

# We are IntechOpen, the world's leading publisher of Open Access books Built by scientists, for scientists

6,300

Open access books available

171,000

International authors and editors

190M

Downloads

Our authors are among the

154

Countries delivered to

TOP 1%

most cited scientists

12.2%

Contributors from top 500 universities



WEB OF SCIENCE™

Selection of our books indexed in the Book Citation Index  
in Web of Science™ Core Collection (BKCI)

Interested in publishing with us?  
Contact [book.department@intechopen.com](mailto:book.department@intechopen.com)

Numbers displayed above are based on latest data collected.  
For more information visit [www.intechopen.com](http://www.intechopen.com)



---

# Combined Transmission Electron Microscopy – *In situ* Observation of the Formation Process and Measurement of Physical Properties for Single Atomic-Sized Metallic Wires

---

Hideki Masuda

Additional information is available at the end of the chapter

<http://dx.doi.org/10.5772/62288>

---

## Abstract

This chapter introduces the research of *in situ* high-resolution transmission electron microscope (HRTEM) methods combined with the functions of atomic force microscope and scanning tunneling microscope. Using this method, we demonstrate fabrication, dynamic observation on an atomistic scale, and mechanical and electrical measurements of nanometer-sized contact simultaneously. We evaluate the silver atomic-sized wire (ASW) which appeared at the final stage of the rupture process of the silver nano-contact.

**Keywords:** Silver, atomic-sized wires, atomic force microscopy, high-resolution transmission electron microscopy

---

## 1. Introduction

Currently, miniaturization of electronics is underway. Now device development is heading toward atomistic and molecular scales [1]. Devices included in these circuits are nanometer-sized contacts (NCs), atomic-sized wires (ASWs), single molecular junctions (SMJs), etc. (Figure 1) [2]. SMJ is a system of single molecule sandwiched by a pair of nanometer-sized metallic electrodes. SMJs enable single electronic operation, high-density integration, and electric power saving [3-7]. To engineer SMJs, we need to reveal that the structure of device configuration includes interfaces between molecules and electrodes and mechanical and electrical properties. Metallic NCs and ASWs are fundamental materials that have the potential for device applications as well as being the key factors required for the application of SMJs [8].

---

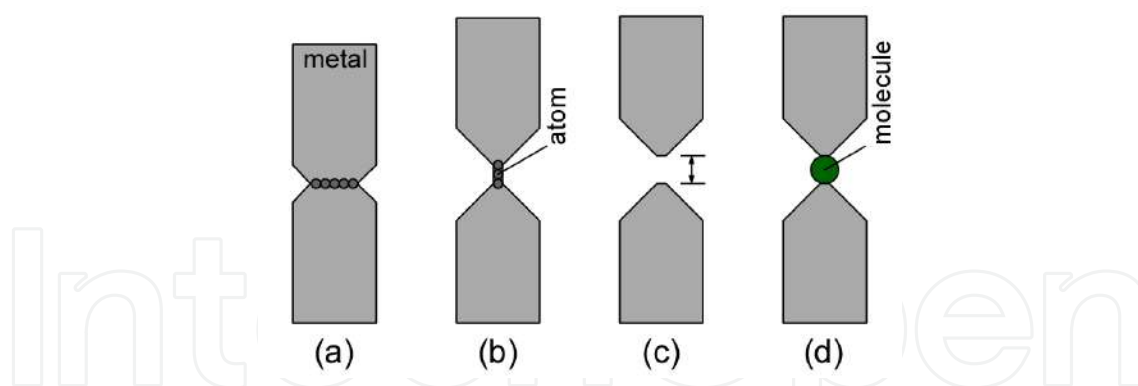


**Figure 1.** Schematics of atomistic-scale devices. (a) NC; (b) ASW; (c) nano-gap structure; and (d) SMJ.

Actually, to observe the formation and deformation of NCs, two *in situ* high-resolution transmission electron microscope (HRTEM) methods were developed; one is the electron beam double holes drilling method. An electron beam drills two holes on a material film with a focused beam. The bridge that was formed between the holes is gradually deformed using a defocused electron beam [9]. The other method is the tip-sample contact method [10], and this fabricates and deforms NCs using a piezo-driven tip. Kizuka and Tanaka observed Zn NCs using this method in HRTEM in 1994 [11]. In 1998, Kizuka et al. directly observed the slip deformation process of Au NCs (Figure 2) [12]. This is the first report that showed atomistic-level observation of a slip deformation process in crystals. After that, Ohnishi et al. fabricated Au NCs and observed the deformation process from a 5-atom width to an 1-atom width in 1998 [13].

In 2001, Kizuka et al. observed the deformation process of Au NCs with atomistic resolution using HRTEM based on the *in situ* method combined with atomic force microscope (AFM) and scanning tunneling microscope (STM) [10]. They measured stress and strain quantitatively and started material mechanics research of metallic NCs. Using this method, the mechanical properties of Cu [14], Ir [15], Pd [16], and Pt [17] NCs were researched.

Further, as Kizuka et al. improved the *in situ* HRTEM method [18]; they were able to observe the structural dynamics of ASWs formation during the tensile deformation process and research electrical and mechanical properties. Using this method, it was revealed that there was a corresponding relationship between structural dynamics and physical properties [19]. Until that point in time they had been researched individually. They observed Au ASW at the final stage of the tensile deformation process of Au NCs. The observed Au ASW is up to 10 atoms in length with an average interatomic distance of 0.27 nm (Figure 3). In the tensile deformation process of ASWs, since tensile stress is concentrated on the contact region, interatomic distances of Au ASWs become longer, up to 0.30 nm. At the same time, conductance of Au ASWs was measured. Resultant conductance greatly decreases when the number of atoms used to construct the ASWs exceeds 4. Moreover, the force acting on the contact was measured. The tensile strength of this ASW was estimated to be from 8 to 17 GPa. This value is several times larger than that of Au NCs and much larger than bulk Au.

At elastic deformation regions undergoing stress–strain, the Young’s modulus of Au ASWs was estimated to be between 47 and 116 GPa. This value is remarkably comparable with that of a single crystal Au.

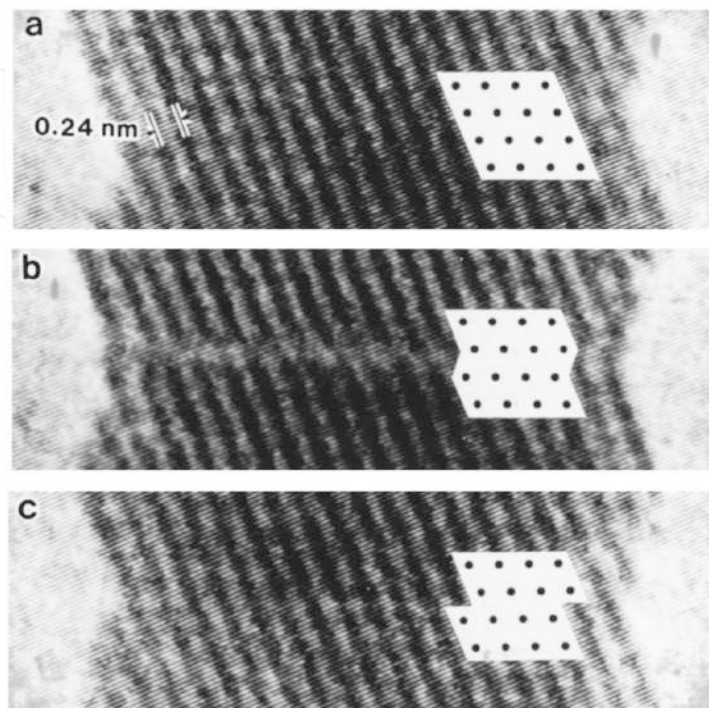


**Figure 2.** Time variation in the elementary steps of slip in the shear deformation of Au NCs [12].

The NCs and ASWs of other materials other than Au have been also observed. Au, Ag [20, 21], Cu [22], Pt [17, 23], Pd [23, 24], Ir [15], and Co [23] ASWs have been observed.

As described above, common problems in research in metallic ASWs and NCs existed, revealing corresponding relationships between structure and electrical properties. As research in ASWs has concentrated on Au, the structural dynamics of ASW formation is uncertain. For some of the metallic ASWs already researched, only the structures that appeared in the tensile deformation process of NCs were observed. Therefore, the stable structure and electrical conductivity of the NCs have not yet been revealed. In order to produce a general rule for the basic phenomenon that appears in metallic NCs and ASWs, it is necessary to examine structural dynamics, electrical conductivity, and mechanical properties, in order to clarify the corresponding relationship between the structure and properties directly. The method is limited to *in situ* HRTEM.

## 2. Combined HRTEM

For the *in situ* tip-sample contact experiment inside the HRTEM, we proposed inserting multiple specimen holders in the specimen chamber. The secondary holder is usually intro-

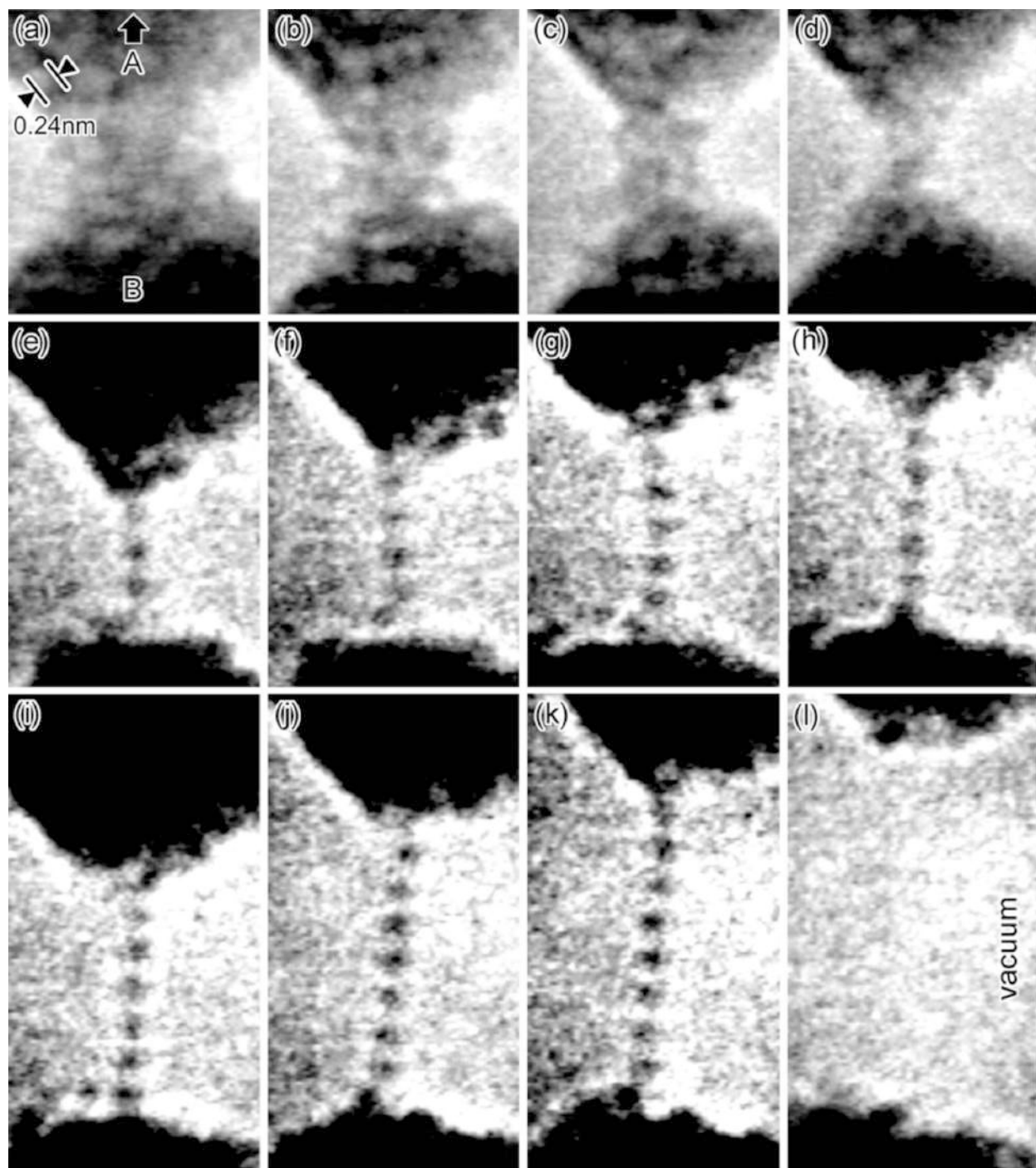


**Figure 3.** Time variation of the Au ASW formation process observed using the *in situ* HRTEM method [19].

duced from the direction perpendicular to the first holder (Figure 4). Since this space is often used for an EDX detector, it is necessary to replace it. In addition, we should consider that this is a space occupying in *z* direction; the relation between the gap distance of pole pieces and the height of sample holders (Figure 5). When you want to do mechanical tests, for example, you would introduce an AFM cantilever. In this configuration, it is rarely applied to a pole piece for high resolution use. This is because the samples must be precisely adjusted to contact

at the standard focal position of the microscope, including the movement range in the *z* direction of the goniometer, which is attached to each holder.

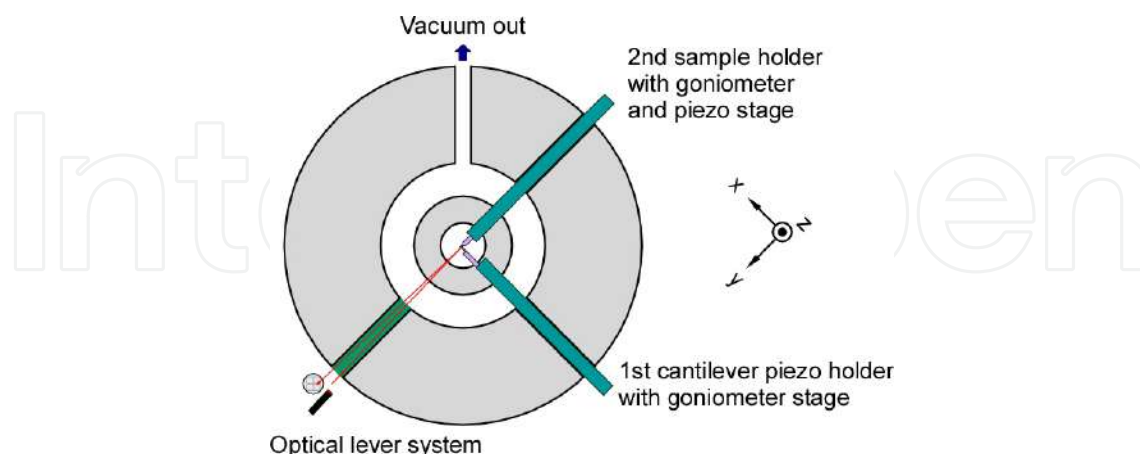


**Figure 4.** Illustration depicting the specimen chamber of the HRTEM combined with atomic force microscope (AFM).

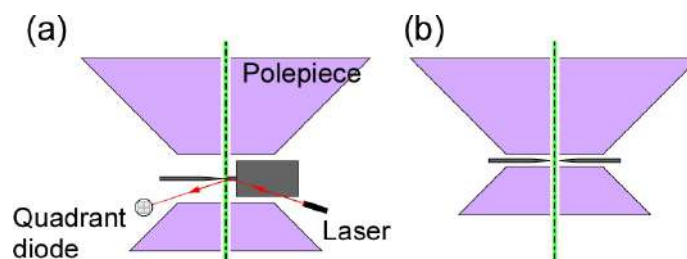


**Figure 5.** Illustrations depicting the configuration of samples and pole pieces for a combined HRTEM.

### 3. Sample preparation

For samples, we use a cut-out metal foil and the metal sputtered tip of the AFM cantilever. In the case of metallic foil, first we cut out the foil with a thickness of below 0.05 mm to a size of 1 mm by 10 mm and sharpen one side of the plate (Figure 6(a)). After that, we polish this side mechanically using emery papers and aluminum or diamond wrapping film. In rare cases, although a burr part of cut is sometimes thin enough for HRTEM observation, the yield is poor and the workability of nano-tip creation processes in a HRTEM is not good because the sample is affected by a stress concentration where there is a sudden change in thickness. This sample is then thinned further by an Ar ion polish of 3–10 kV (Figure 6(b)). It may be that an ionic cleaner is used just before introducing it into a vacuum.

When performing the mechanical tests simultaneously, it is suggested that you use a metallic sputtered Si tip on the cantilever for AFM for one of the samples (Figure 7). For high-resolution (HR) observations, in order to detect the small force needed to deform the fine structure, the

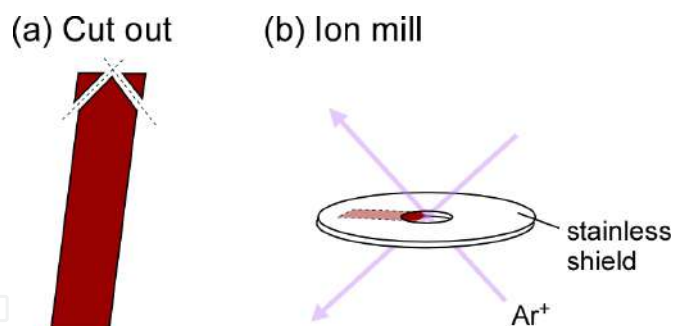


**Figure 6.** Illustrations showing the downsize process of metal foil.

spring constant of the cantilever is required to be small (5 N/m or less is preferred). Metal is sputtered on the cantilever and the tip under a reduced pressure Ar atmosphere. The thickness of metallic film is approximately 20 nm. The requirements in this process are (i) depositing metal atoms on the tip for use in contact with the counter sample and (ii) ensuring the cantilever surface is covered with a uniform continuous metallic film to offer sufficient conductivity. In order to achieve the latter requirement, it would be preferable to sputter in the same way on both sides of cantilever. Moreover, even if the required amount of sputtering is achieved, the spring constant of the cantilever is not changed.

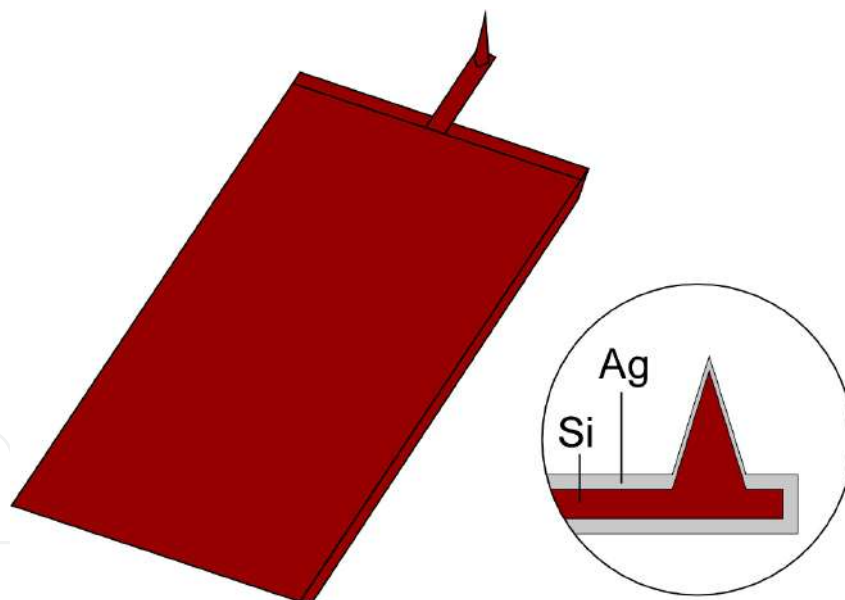


**Figure 7.** Illustration of cantilever preparation for the Ag contact experiment.

Both samples are attached to a specimen holder respectively, then inserted into the HRTEM specimen chambers. Because the sample is exposed to air for several minutes during this preparation process, a natural oxide or sulfide film is deposited on the sample surface. After the first contact with the sample each other, once we should make the contact larger than a width of several tens nanometers. This is because we pull a clean metal part to the surface from inside the samples.

#### 4. Observation of Ag ASWs

Figure 8 shows HR images during the process of miniaturization of Ag NCs. The black areas at the top and bottom of each image are Ag, the center is the NC, and the surrounding area is a vacuum. On all of the NCs, a lattice interval of Ag (0.24 nm) has appeared – as indicated by (111) in the figure. That is, the contact region is a single crystal. Therefore, the direction of incidence of the electron beam is indicated on the figure as [0-11] and the upward direction on image is identified as [100] in the figure. The minimum cross-sectional width of the NC is (a) 4 atoms, (b) 3 atoms, and (c–e) 1 atom. Figure 8(f) shows the contact braking.

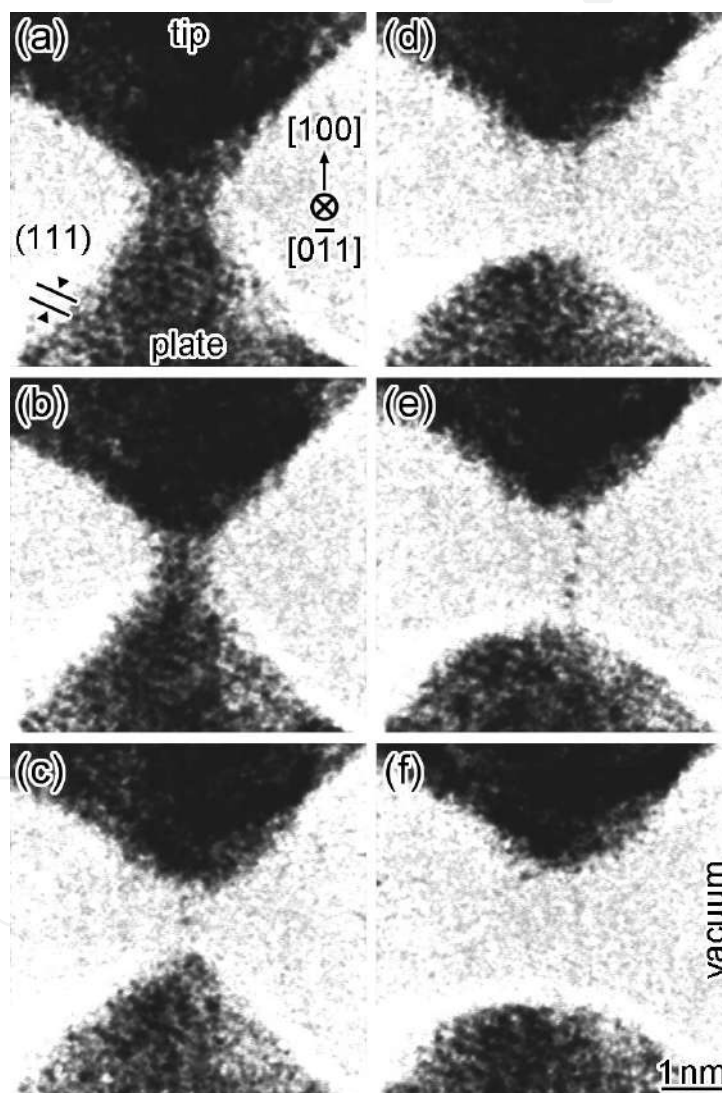


**Figure 8.** Time variation of Ag ASW formation process observed by *in situ* HRTEM.

Figure 9, it shows the calculated image and HR image for the Ag ASW. For the image calculation, we used a model in which both ends of the wire (composed of seven atoms) were connected to two pyramidal Ag crystals (Figure 9(a)). Seven of the Ag ASW atoms were along

the [100] crystal pyramid and arranged at intervals of 0.289 nm, which is the nearest neighboring distance of the bulk Ag. Figure 9(b) is a calculated image for the model. In Figure 9(c), the image intensity along the center line of the atomic wires is shown. The centers of the models of the atoms are displaced from the centers of the black point in computational image by only 0–0.02 nm. Since the experimental spatial resolution of the current HRTEM observation is 0.1 nm, the calculated result agree with the experimentally observed image within that resolution. This correspondence is similar to that of Au atoms in a wire [19]. Figure 9(d) is an enlarged view of the Ag ASW shown in Figure 8(e). Figure 9(c and e) shows the image intensity along the center line of the ASWs. The darkest positions are indicated by the arrows. From the results of the image calculation, the atomic positions of the ASWs can be considered to correspond to the darkest position in the image intensity.

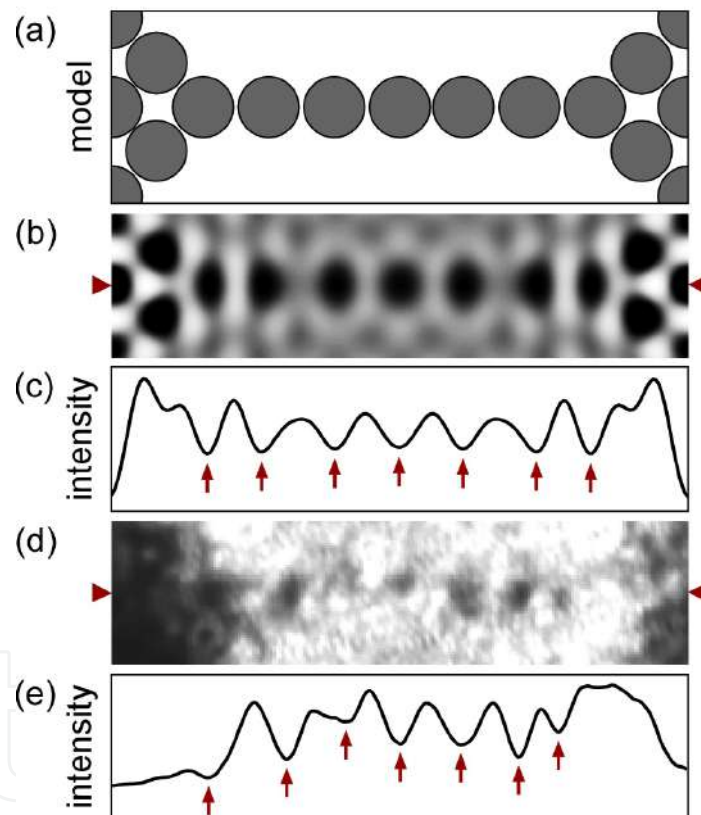


**Figure 9.** HR images of Ag ASWs. (a) Projected model along [110]; (b) calculated image for the structural model of (a); (c) line profile of (b); (d) enlarged experimental image of Figure 8(e); and (e) line profile of (d).

Figure 10 shows the time variation of force and conductance in the Ag ASW formation process shown in Figure 8. Times (a–f) correspond to the times that each image in Figure 8 was observed, respectively. As the NC narrowed, the conductance stepwise reduced (a–b). Similarly, the force acting on the NC also decreased stepwise. Thereafter, when the ASW forms (c–e), both conductance and force were reduced below  $0.1 G_0$  and 0.5 nN.

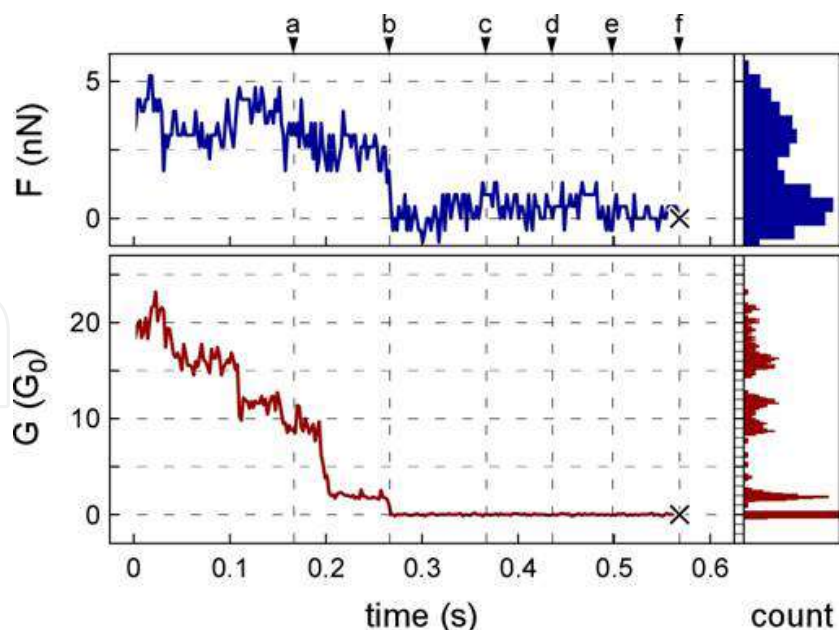


Figure 10. Time variation in the force and conductance measured in the deformation process of Figure 8.

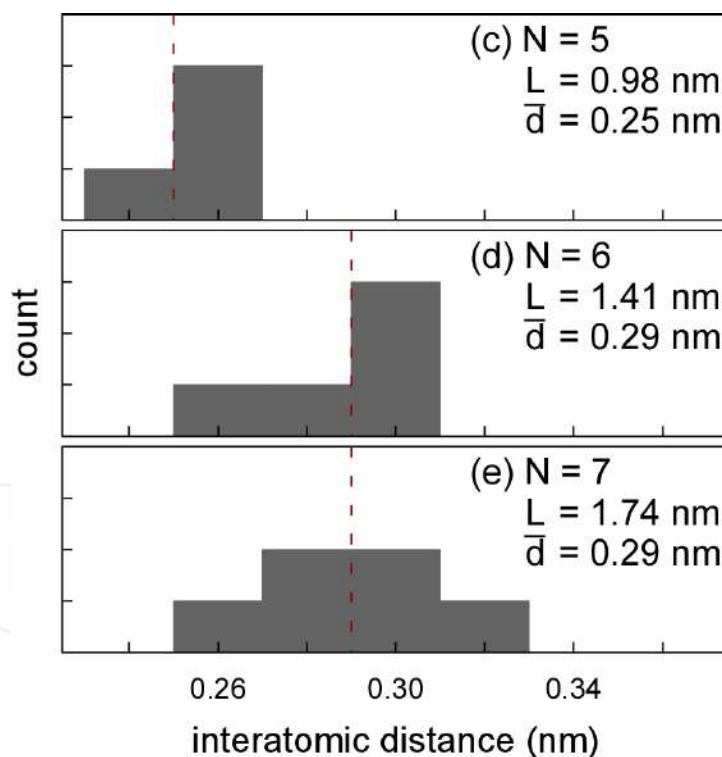
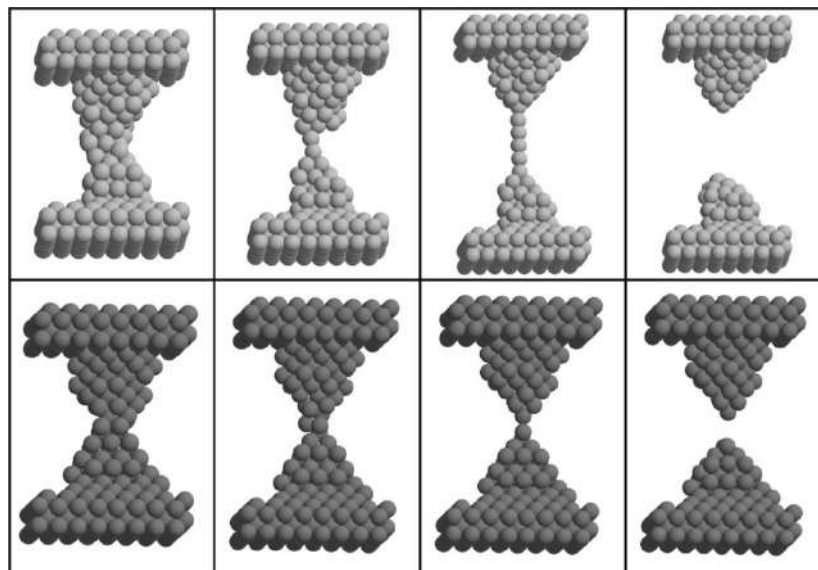


Figure 11. Distribution of interatomic distances in Ag ASWs.

Figure 11 shows the distribution of the interatomic distances between atoms in the wire, observed in Figure 8. When the number of atoms in the ASW was five, the interatomic distance was  $0.25 \pm 0.01$  nm. However, this became  $0.29 \pm 0.05$  nm for an ASW comprised of six or seven atoms. In other words, as the ASW becomes longer, the interatomic distance increases.

ASWs are generally considered to be formed by pulling out atoms one by one from the electrode. Bahn and Jacobsen calculated the process of pulling metal NCs (Figure 12) using the density functional method via molecular dynamics calculations and effective medium approximation [25]. In the state where tip atoms, from two pyramid-shaped electrodes, bond to one another, the single atom located at the minimum cross-section part bonds to not only three or four atoms of the electrode side but also atoms at the opposite electrode simultaneously. They estimated the bonding strength between these atoms, then went on to discuss whether this monatomic junction can draw atoms from the electrode without leading to a fracture. As a result, for Au and Pt, the strength of the binding of atoms in the wire part is energetically three times larger than that in the electrode part; it tends to form ASWs. On the other hand, for Cu, Ag, Ni, and Pd, it is difficult to form ASWs in this way.



**Figure 12.** MD simulation of the tensile deformation process for Au (upper) and Cu (lower) NCs [25].

In the experiment shown in Figure 8, Ag ASWs were formed by tensile deformation of NCs. Since as soon as the NC is miniaturized to one atom width (Figure 8(b)), it forms four or more atomic length wires, the stretching process from a single atom contact could not be observed. In other words, the structural change from the Ag NC to the Ag ASW was faster than the frame rate available using TEM observations ( $\sim 17$  ms). Moreover, we have applied a voltage of 13 mV for the conductance measurement. The withdrawal of atoms from the electrode for atomic wires involved not only tensile force, but also atom transfer by electron wind force. As an example of this effect, when we apply a voltage of 100 mV to the NC, ASW with a length of  $\sim 0.88$  nm formed just before breaking without applying tensile force [8]. Therefore, even for some of the elements for which ASWs were hardly expected to form, there remains the possibility of wire formation due to the atomic diffusion effect.

## 5. Conclusion

In this chapter, we introduced combined microscopy techniques which are based on HRTEM, AFM, and STM. This approach was developed to meet the demand for characterization of nanostructures which needs correspondence between the structure and the physical properties directly. In fact, this research has been promoted with respect to the junction between nano-scales or atomistic scales for a single metal. In the future, this method needs to be combined with chemical reaction engineering for single molecular device fabrication, such as catalysts, corrosion, and storage devices.

## Acknowledgements

This work was partly supported by Grant-in-Aid for JSPS Fellows (10J01479).

## Author details

Hideki Masuda\*

Address all correspondence to: [masuda.hideki@nims.go.jp](mailto:masuda.hideki@nims.go.jp)

National Institute for Materials Science, Tsukuba, Japan

## References

- [1] Cuevas, JC, and Scheer, E, *Molecular Electronics: An Introduction to Theory and Experiment*. World Scientific, Singapore, 2010.
- [2] Joachim, C, Gimzewski, JK, and Aviram, A: Electronics using hybrid-molecular and mono-molecular devices. 2000; 408: 541. *Nature*.
- [3] Di Ventra, M, Pantelides, ST, and Lang, ND: First-principles calculation of transport properties of a molecular device. 2000; 84: 979. *Physical Review Letters*.
- [4] Kubatkin, S *et al.*: Single-electron transistor of a single organic molecule with access to several redox states. 2003; 425: 698. *Nature*.
- [5] Tao, NJ: Electron transport in molecular junctions. 2006; 1: 173. *Nature Nanotechnology*.

- [6] Danilov, A *et al.*: Electronic transport in single molecule junctions: Control of the molecule-electrode coupling through intramolecular tunneling barriers. 2007; 8: 1. Nano Letters.
- [7] Kim, WY, *et al.*: Application of quantum chemistry to nanotechnology: Electron and spin transport in molecular devices. 2009; 38: 2319. Chemical Society Reviews.
- [8] Masuda, H, and Kizuka, T: Distance control of electromigration-induced silver nanogaps. 2014; 14: 2436. Journal of Nanoscience and Nanotechnology.
- [9] Kondo, Y, and Takayanagi, K: Gold nanobridge stabilized by surface structure. 1997; 79: 3455. Physical Review Letters.
- [10] Kizuka, T, *et al.*: Simultaneous observation of millisecond dynamics in atomistic structure, force and conductance on the basis of transmission electron microscopy. 2001; 40: L170. Japanese Journal of Applied Physics.
- [11] Kizuka, T, and Tanaka, N: Dynamic high-resolution electron microscopy of diffusion bonding between zinc oxide nanocrystallites at ambient temperature. 1994; 69: 135. Philosophical Magazine Letters.
- [12] Kizuka, T: Atomistic visualization of deformation in gold. 1998; 57: 11158. Physical Review B.
- [13] Ohnishi, H, Kondo, Y, and Takayanagi, K: Quantized conductance through individual rows of suspended gold atoms. 1998; 395: 780. Nature.
- [14] Fujisawa, S, Kikkawa, T, and Kizuka, T: Direct observation of electromigration and induced stress in Cu nanowire. 2003; 42: L1433. Japanese Journal of Applied Physics.
- [15] Ryu, M, and Kizuka, T: Structure, conductance and strength of iridium wires of single atom width. 2006; 45: 8952. Japanese Journal of Applied Physics.
- [16] Matsuda, T, and Kizuka, T: Structure of nanometer-sized palladium contacts and their mechanical and electrical properties. 2007; 46: 4370. Japanese Journal of Applied Physics.
- [17] Kizuka, T, and Monna, K: Atomic configuration, conductance, and tensile force of platinum wires of single-atom width. 2009; 80: 205406. Physical Review B.
- [18] Kizuka, T, Umehara, S, and Fujisawa, S: Metal-insulator transition in stable one-dimensional arrangements of single gold atoms. 2001; 40: L71. Japanese Journal of Applied Physics.
- [19] Kizuka, T: Atomic configuration and mechanical and electrical properties of stable gold wires of single-atom width. 2008; 77: 155401. Physical Review B.
- [20] Rodrigues, V *et al.*: Quantum conductance in silver nanowires: Correlation between atomic structure and transport properties. 2002; 65: 153402. Physical Review B.

- [21] Lagos, MJ, *et al.*: Observation of the smallest metal nanotube with a square cross-section. 2009; 4: 149. *Nature Nanotechnology*.
- [22] González, JC, *et al.*: Indication of unusual pentagonal structures in atomic-size Cu nanowires. 2004; 93: 126103. *Physical Review Letters*.
- [23] Rodrigues, V, *et al.*: Evidence for spontaneous spin-polarized transport in magnetic nanowires. 2003; 91: 096801. *Physical Review Letters*.
- [24] Matsuda, T, and Kizuka, T: Palladium wires of single atom width as mechanically controlled switching devices. 2006; 45: L1337. *Japanese Journal of Applied Physics*.
- [25] Bahn, SR, and Jacobsen, KW: Chain formation of metal atoms. 2001; 87: 266101. *Physical Review Letters*.

IntechOpen



# We are IntechOpen, the world's leading publisher of Open Access books Built by scientists, for scientists

6,300

Open access books available

171,000

International authors and editors

190M

Downloads

Our authors are among the

154

Countries delivered to

TOP 1%

most cited scientists

12.2%

Contributors from top 500 universities



WEB OF SCIENCE™

Selection of our books indexed in the Book Citation Index  
in Web of Science™ Core Collection (BKCI)

Interested in publishing with us?  
Contact [book.department@intechopen.com](mailto:book.department@intechopen.com)

Numbers displayed above are based on latest data collected.  
For more information visit [www.intechopen.com](http://www.intechopen.com)



---

# Focused Ion Beams (FIB) – Novel Methodologies and Recent Applications for Multidisciplinary Sciences

---

Meltem Sezen

Additional information is available at the end of the chapter

<http://dx.doi.org/10.5772/61634>

---

## Abstract

Considered as the newest field of electron microscopy, focused ion beam (FIB) technologies are used in many fields of science for site-specific analysis, imaging, milling, deposition, micromachining, and manipulation. Dual-beam platforms, combining a high-resolution scanning electron microscope (HR-SEM) and an FIB column, additionally equipped with precursor-based gas injection systems (GIS), micromanipulators, and chemical analysis tools (such as energy-dispersive spectra (EDS) or wavelength-dispersive spectra (WDS)), serve as multifunctional tools for direct lithography in terms of nano-machining and nano-prototyping, while advanced specimen preparation for transmission electron microscopy (TEM) can practically be carried out with ultrahigh precision. Especially, when hard materials and material systems with hard substrates are concerned, FIB is the only technique for site-specific micro- and nanostructuring. Moreover, FIB sectioning and sampling techniques are frequently used for revealing the structural and morphological distribution of material systems with three-dimensional (3D) network at micro-/nanoscale. This book chapter includes many examples on conventional and novel processes of FIB technologies, ranging from analysis of semiconductors to electron tomography-based imaging of hard materials such as nanoporous ceramics and composites. In addition, recent studies concerning the active use of dual-beam platforms are mentioned.

**Keywords:** Focused Ion Beams, Electron Microscopy, Dual-Beam Platforms, Nanostructuring, Nanoanalysis

---

## 1. Introduction

The miniaturization of novel materials, structures, and systems down to the atomic scale has assigned *electron microscopy*, a complementary branch of *nanotechnology*, for multidisciplinary sciences. In particular, transmission electron microscopy (TEM), scanning electron microscopy

---

(SEM), focused ion beams (FIB), and atomic force microscopy (AFM) can be considered as the most comprehensive techniques for advanced and precise analysis on different material species. Among all, *focused ion beam* microscopes are becoming more popular due to their versatility and configurational flexibility, as numerous tasks can practically be carried out with a single tool. Currently, many cutting-edge integrated microscope systems allow for nanosurgery applications inside a pressurized microscope chamber using in situ applications by means of using the capabilities of related tools and attachments that are coupled to related equipment. The best candidate is the dual-beam (also called two-beam or multi-beam) platforms.

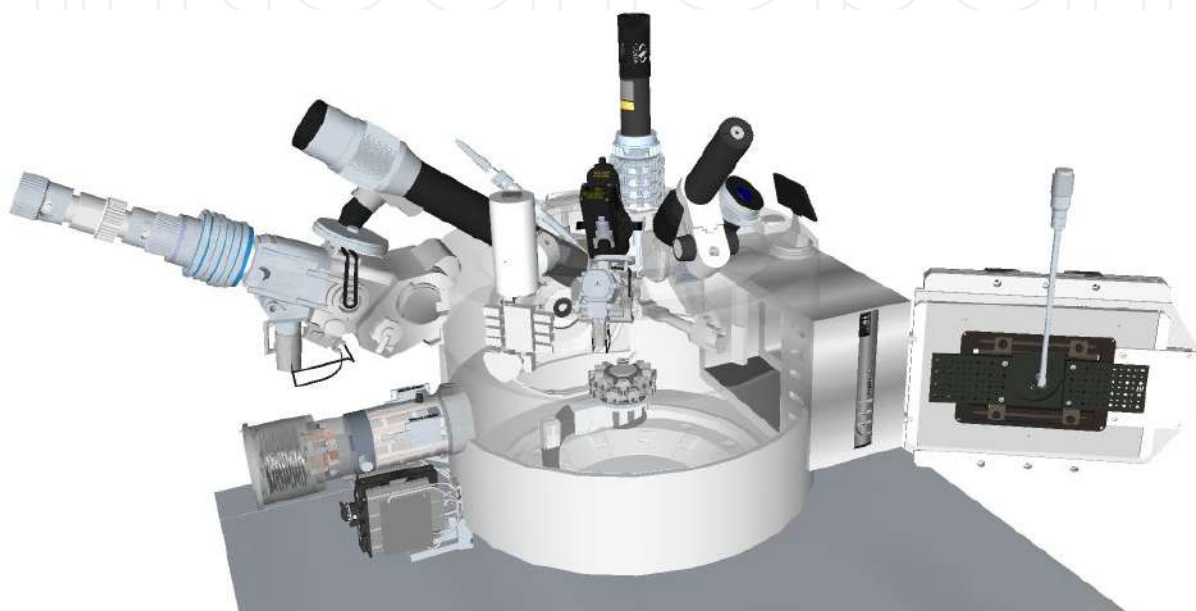


**Figure 1.** Illustration of a dual-beam platform with several attachments

Dual-beam platforms, consisting of an HR-SEM and an FIB column and additionally equipped with gas injection systems (GIS), micromanipulators, and detectors, serve as multifunctional tools for direct lithography in terms of nano-machining and nano-prototyping. A commercial dual-beam platform is shown in Figure 1. In the dual-beam platforms, in addition to imaging and chemical analysis of matter at ultrahigh resolution, many more processes can successfully be carried out from the micro- down to nanoscale, such as fabrication, structuring, deposition, prototyping, machining, 3D sculpturing, and manipulation. Using electron and ion beams in an integrated dual-beam platform, a wide variety of applications can be performed for multidisciplinary fields of nanotechnology: from material sciences and semiconductor technologies to biosciences. Whereas the initial development of focused ion beam (FIB) instruments was driven by their unique capabilities for computer chip repair and circuit modification in semiconductor technology, present FIB applications support a much broader range of scientific and technological disciplines [1,2]. The versatility and multifunctionality of these platforms give users inspiration and *enthusiasm* for developing new methodologies of nanostructuring and nanoanalysis upon the needs and the properties of diverse materials and systems.



**Figure 2.** A commercial FIB/SEM workstation equipped with GIS, micromanipulator, and EDS detector (JEOL JIB 4601F MultiBeam System at Sabanci University Nanotechnology Research and Application Center-SUNUM)

Fundamentally, an FIB column produces and directs a stream of high-energy ionized atoms of a relatively massive element, focusing them onto the sample both for the purpose of etching or milling the surface and as a method of imaging. The ions' greater mass allows them to easily expel surface atoms from their positions and produces secondary electrons (SE) from the surface, allowing the ion beam to image the sample before, during, and after the lithography process. The ion beam has a number of other uses as well, including the deposition of material from a gaseous layer above the sample [3]. Most of the recent commercial FIB systems and dual-beam platforms use gallium ( $\text{Ga}^+$ ) as the ion source. The reason for preferring gallium element as the ion source is explained in the subsequent sections.

Concerning micro- and nano-sectioning processes, rapid FIB slicing techniques are frequently preferred for especially hard materials (e.g., metals, glass, ceramics) or layered structures (e.g., semiconductors) with hard substrates (silicon, glass, ceramics, etc.) because corresponding materials cannot be mechanically sliced by cutting tools. It has been always reported that ion milling is not a proper method for soft materials due to their sensitivity to beam damage and heat-dependent shape distortion. Therefore, for soft materials, ultramicrotomy has so far been accepted as the most convenient preparation technique, which is a mechanical serial sectioning process that uses diamond knives or blades for cutting cross sections from the materials that were embedded in epoxy resin. However, currently, due to the progress in the FIB technologies and due to advanced procedures and novel recipes developed by experienced users, some processes can also be allowed for soft materials as FIB applications still have many advantages over mechanical sectioning methods. Most of the newest procedures include the application

of low voltage, low current, and gentle instrumental parameters, and bringing the microscope chamber to low temperatures and to even cryogenic conditions might also be necessary for specific experimental studies particularly when soft cells and organic materials are to be examined and structured.

FIB is recently considered to be the best technique for site-specific TEM specimen preparation. For an efficient TEM tomography analysis, the specimen has to be precisely structured so that it represents all its properties originally in 3D at the nanometer scale. Such samples can be successfully structured using the capabilities of FIB-SEM systems, e.g., ion milling, micro-/nanostructuring, deposition, manipulation, and polishing. Another application of dual-beam instruments is the 3D FIB tomography, where the material is cross-sectioned by ion milling sequentially, and from each sliced surface, an electron image (e.g., SE) or elemental information by energy-dispersive spectra (EDS) is acquired. Consequently, the collected serial two-dimensional (2D) data can be stacked and reconstructed to form ultimate comprehensive 3D data. Using this procedure, different material systems can be characterized for their morphological and elemental distributions in 3D.

Three-dimensional electron tomography is extensively used for revealing the structural and morphological distribution of material systems with 3D network at micro-/nanoscale. Accordingly, specific sample preparation techniques that keep the original structures to be investigated at the TEM are often required. FIB technologies, which are gaining high impact for their applications on diverse fields of science, provide material-dependent and TEM analysis spectrum-based solutions that are highly rapid, practical, creative, and reliable. The main approach is to overcome the limitations and difficulties (e.g., to be able to acquire only 2D data instead of 3D, projection problem that occurs at TEMs), which can be faced during electron microscopy-based characterization. In order to investigate the structural properties of the related materials in detail, practical, rapid, and reliable electron microscopy techniques and characterization methodologies have to be determined. This is very supportive in the direction of improving the quality of the production and the final product. TEM tomography enables to image the samples for different angles of tilting, which can be performed by 2D tilt series, and consequently, 3D reconstruction and segmentation can be carried out. Eventually, the resolving power of electron tomography (3D atomic resolution achieved) can be accompanied with analytical possibilities such as electron energy loss spectroscopy (EELS) and EDS. For performing TEM tomography work, special FIB samples (e.g., pin-like) that enable tilt series without projection problems are also needed to be prepared by experts.

Nevertheless, *irradiation damage*, caused by the use of beams in the electron microscopes, which leads to undesired physical/chemical material property changes or uncontrollable modification of structures that are being processed, should not be underestimated. Especially, soft matter such as polymers or biological materials is highly susceptible and very much prone to react on electron/ion beam irradiation. The effect is even higher when the ions are used as incident particles, and the end effect might even be the total loss of the material properties. The reason for that is, focused ions (in case of FIB, this is usually  $\text{Ga}^+$ ) are energetic species with a high momentum and relatively low mean path, due to their mass. Therefore, they strongly affect surface composition, leading to extensive chemical modification and sometimes

resulting in graphitization. Nonetheless, it is well possible to turn degradation-dependent physical/chemical changes from negative to positive use when materials are intentionally exposed to beams. Especially, controllable surface modification allows tuning of surface properties in intended directions and thus provides the use of the ultimate materials and their systems toward desired and predefined concepts. Moreover, FIB is capable of performing maskless site-specific structuring, which are considered to be the major advantages of FIB over e-beam lithography. In particular, surface modification processes can be carried out through gas-assisted etching (GAE) in an FIB-SEM dual-beam instrument equipped with gas injections systems (GIS).

In the following sections, fundamentals of dual-beam technologies are revealed and examples of conventional and novel dual-beam applications and processes as well as structuring and modification of structures and surfaces are explained in detail.

## 2. Fundamentals of FIB technologies

### 2.1. Focused ion beams and FIB/SEM platforms

FIB systems are very similar to SEM, while the only difference is the use of an ion beam for scanning the sample surfaces, instead of an electron beam. In the FIB systems, a focused beam of metal ions is generated by a liquid metal ion source (LMIS). The LMIS is able to provide a source of ions of  $\approx 5$  nm in diameter, and a typical LMIS contains a tungsten (W) needle attached to a reservoir that holds the metal source material. There are several metallic elements or alloy sources that can be used in LMIS [4]. Among all, gallium ( $\text{Ga}^+$ ) is commonly preferred in commercial FIB instruments owing to its advantages that are summarized as follows [2]:

- i. Gallium has low melting point ( $T_m = 29.8$  °C), minimizing reaction or inter-diffusion probabilities between the liquid and the tungsten needle, from where the ions are emitted.
- ii. The low volatility of gallium at the melting point protects the supply of metal, and this yields a long source life.
- iii. The low surface free energy leads to viscous behavior of the liquid on the substrate.
- iv. The low vapor pressure allows gallium to be used in its pure form rather than in the form of an alloy source. This yields a long lifetime of the source as the liquid will not evaporate.
- v. Gallium has excellent mechanical, electrical, and vacuum properties.
- vi. Gallium's emission characteristics provide high angular intensity with a small energy spread.

Once the  $\text{Ga}^+$  ions are extracted from the LMIS, they are accelerated down to the ion column up to 30 keV and subsequently focused onto the sample using electrostatic lenses. The ion column typically has two lenses, a *condenser lens* and an *objective lens*. The condenser lens is the

probe-forming lens and the objective lens is used to focus the beam of ions at the sample surface. Beam currents from a few picoamperes up to 60 nA can be obtained.

An optimum ion probe can be achieved by adjusting apertures, tuning all lenses, and doing final settings of the beam, such as stigmator and focus corrections. Cylindrical octopole lenses placed in an FIB system have multiple uses, which include beam deflection, alignment, and stigmation correction [2]. It should be reminded that, in both SEM and TEM systems, *magnetic lenses* are used for focusing the beam. Because ions are massive and they travel at much lower velocities, their *Lorentz force* is lower and magnetic lenses are less effective on ions than they would be on electrons at the same accelerating voltages. As a result, FIB columns are equipped with electrostatic lenses rather than magnetic lenses.

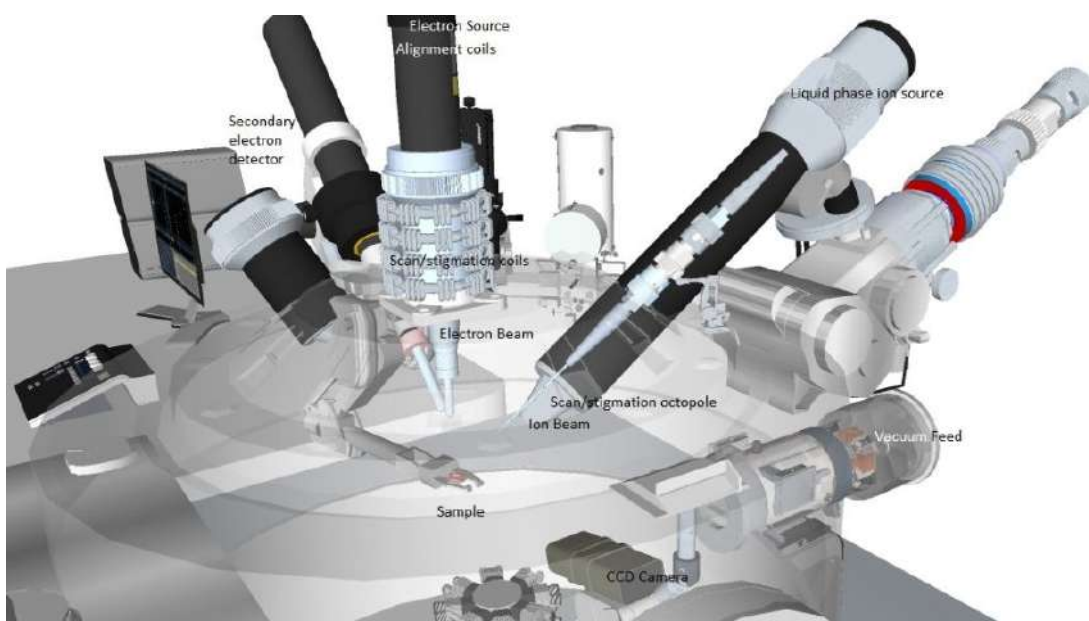


**Figure 3.** Construction of a dual-beam chamber

Commercial dual-beam platforms incorporate both a FIB column and a SEM column in a single system. This combination is especially useful for sample preparation of cross-sections using the electron beam to view this cross-sectional face as the ion beam mills normal to the sample surface. This monitoring allows the milling to be stopped precisely when the task is completed. The typical dual-beam column configuration is a vertical electron column with a tilted ion column. In dual-beam platforms, the tilt angle of the FIB column can vary from manufacturer to the model, but usually it is between 52° and 55° tilt to the vertical.

Both SEM and FIB can be used to acquire high-resolution images by collecting the secondary electrons (SE) that are emitted from the interactions between the beam and the surface atoms, although backscattered electrons (BSE) and/or secondary ions (SI) can contribute to form images. For secondary electron detection, Everhart–Thornley electron multiplier detector is the most common design used recently [3]. The main difference between scanning and/or transmission electron microscopy and focused ion beams is the use of ions as the beam that is

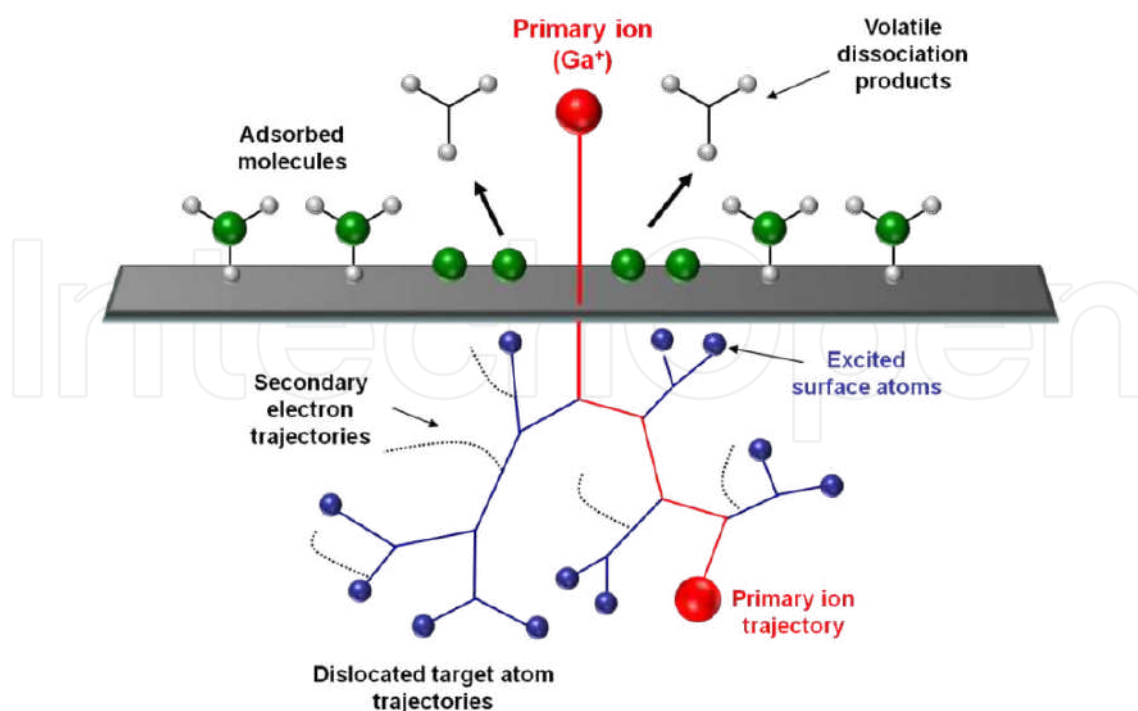


**Figure 4.** The interactions of primary ions generating secondary electrons and the collision cascade. The non-sputtered target atoms remain as excited surface atoms contributing to the molecule dissociation (modified from [5])

also responsible for many interactions occurring at the sample surface. Because ions are much larger in size than electrons, they are not able to penetrate within specimens' individual atoms, and outer shell interaction results in atomic ionization and breaking of chemical bonds of the target material. Secondary electrons are formed and alterations in the chemical stability are generated by this means. The interactions of primary ions and the target surface are responsible for the generation of secondary electrons, while the non-sputtered target atoms remain as excited surface atoms and contribute to dissociation of molecules [5].

## 2.2. Beam–specimen interactions

Dual-beam platforms allow the use of electron and ion beams for several applications through particle–sample interactions and/or reactions. As already very well known by electron microscope users, electrons may adversely affect organic or inorganic samples when they are placed in an electron microscope (e.g., SEM or TEM) for different purposes and may cause temporary or permanent changes within the specimen. The main effects might be in the form of electrostatic charging, ionization damage (radiolysis), displacement damage, sputtering heating, and hydrocarbon contamination. Typically, the amount of radiation damage is proportional to the electron dose, and the extent of damage depends on the amount of energy deposited in the specimen [6].

When ions are accelerated from a source and hit on the specimen surface in an ion column, they enter the target material as they might interact with specimen in various ways within a penetration volume. This interaction, depending on the ion energy, can be in the form of

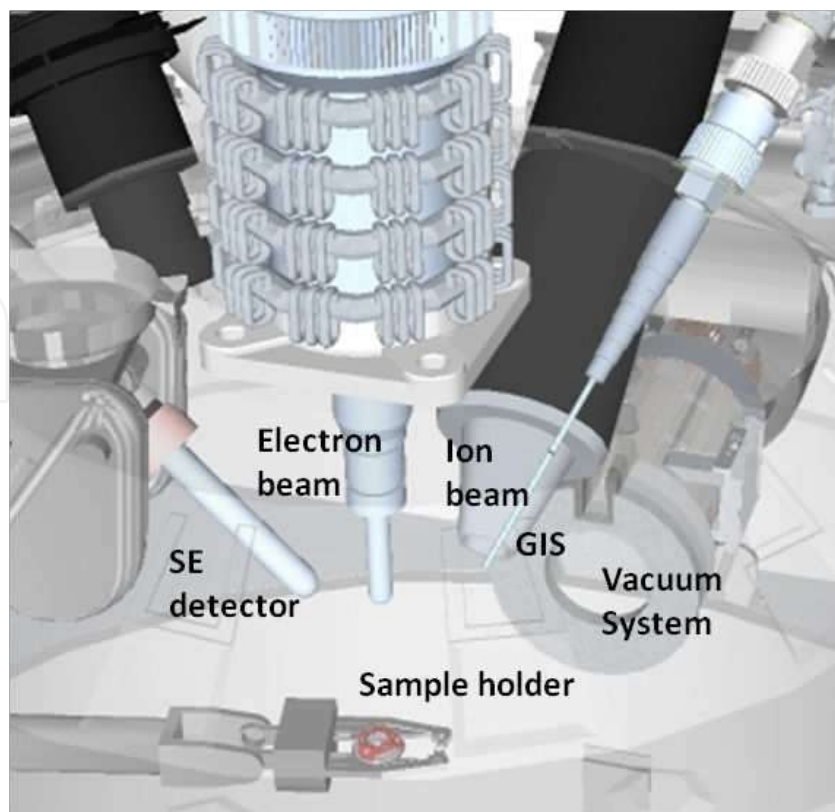


**Figure 5.** Illustration of the specimen chamber of a dual-beam platform

sputtering, amorphization, swelling, deposition, redeposition, implantation, backscattering, or nuclear reaction. However, many of the interactions are not completely separable and occur simultaneously, and it is often not very well understood which mechanism is dominating in the degradation process of specimens being irradiated by ions. Radiation damage not only leads to morphological changes but also alters intrinsic physical properties (crystallinity, elasticity, conductivity, electrostatic charge), as well as chemical characteristics (hydrophilicity, surface composition) of the surface.

The most dominating mechanisms for ion irradiation are discussed below:

- i. **Sputtering:** Sputtering is actually the same as ion milling process and is the major mechanism for material removal. Usually, sputtering range increases with increased ion energies, while heavier ion sources or lower surface binding energies of target materials can contribute to higher sputtering regimes.

A software package called SRIM (Stopping and Range of Ions in Matter)/TRIM (TRansport of Ions in Matter) has been widely used for predicting the range of sputtering for many different ions at a wide energy range. SRIM/TRIM uses a Monte Carlo treatment of ion–atom collisions to calculate the stopping range of ions into the matter. SRIM/TRIM calculations agree very well with the experimental data for the cases considered, and the sputter yield is dependent not only on the material but also on many processing parameters, including the ion energy, angle of incidence, and scanning procedures.

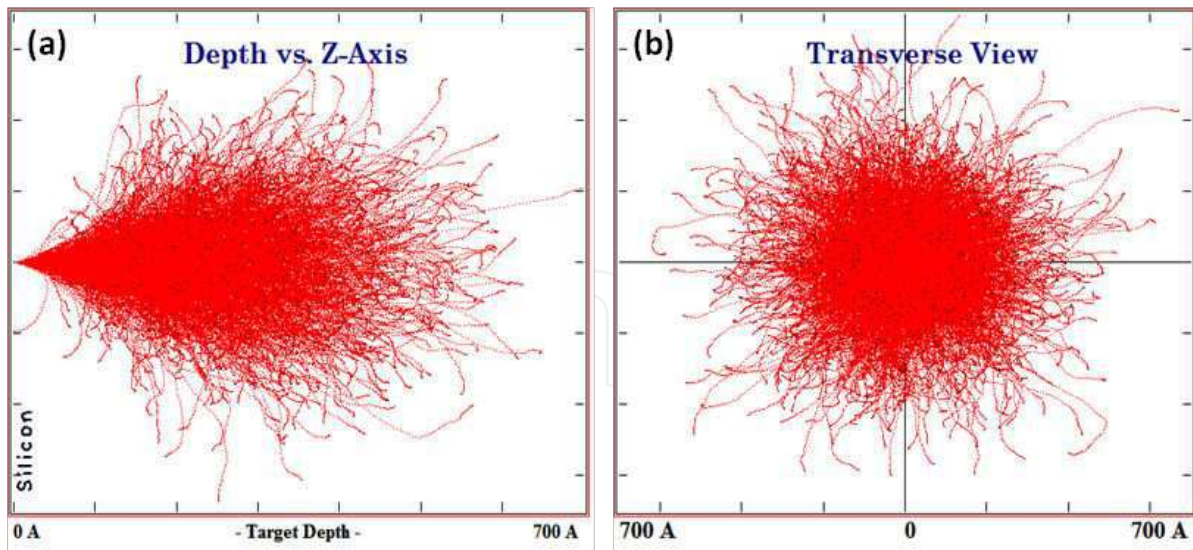


**Figure 6.** TRIM calculations for gallium penetration on silicon (for 30 keV ion energy, 0° angle and 5000 ions): (a) through z-axis, (b) transverse projection

- ii. **Gallium Implantation:** Sputtering mechanism may cause gallium ions to be implanted and mixed into the specimen. This might be responsible for the alteration of the specimen's local composition within the interaction volume. Gallium implantation may lead to structural changes, as well as alteration in, e.g., thermal, electrical, optical, and mechanical properties.
- iii. **Redeposition:** Sputtered particles leaving material's surface in gas phase are very prone to condense back into the solid phase upon collision with solid surfaces, as they are not thermodynamically in equilibrium. As a result, a portion of ejected atoms tend to stick back into the sputtered surfaces and redeposit. Redeposition can be minimized via using low ion doses (e.g., currents), deposition of protective layers using low ion energies, and optimizing ion milling geometries.
- iv. **Amorphization:** Amorphization of the materials that are processed with focused ions may occur in the bombarded area of a crystalline substrate and may induce the substrate to swell. This mechanism can be attributed to sufficient atom displacement within the collision cascade, resulting in the loss of crystalline orientation. Amorphization is usually faced during TEM specimen preparation and might be a serious problem for the crystalline structures to be investigated in TEM. Hence, the use of low ion energies during the polishing step of the preparation process can drastically help in minimizing amorphization effects.
- v. **Swelling:** Swelling of the target material due to ion bombardment during FIB processing is dependent on two major mechanisms: amorphization and ion implantation. Swelling is mostly attributed to material amorphization, while ion implantation does not seem to remarkably contribute to volume expansion. Distortion of the crystalline orientation to amorphous structures leads to volumetric alterations and

hence swelling of the material. Also implanting of gallium ions into the target material is found to be another reason for swelling mechanism during FIB processing.

## 2.3. Basic applications of FIB

### 2.3.1. Ion milling

Ion milling, as the fundamental application of FIB systems, is a continuous sputtering process that occurs during ion beam exposure on the sample. Milling is actually an atomic collision process that ends up in the removal of the material from the ion-sample interaction volume, mainly depending on the beam current and voltage used in the process. Ion milling can be used to create both simple structures, such as lines, rectangles, or circles in the material, and complex patterns, bitmaps, and streamline files. In addition, specific singular or serial patterns can be created by internal patterning engines or external lithography software and can be easily imported to FIB user interfaces.

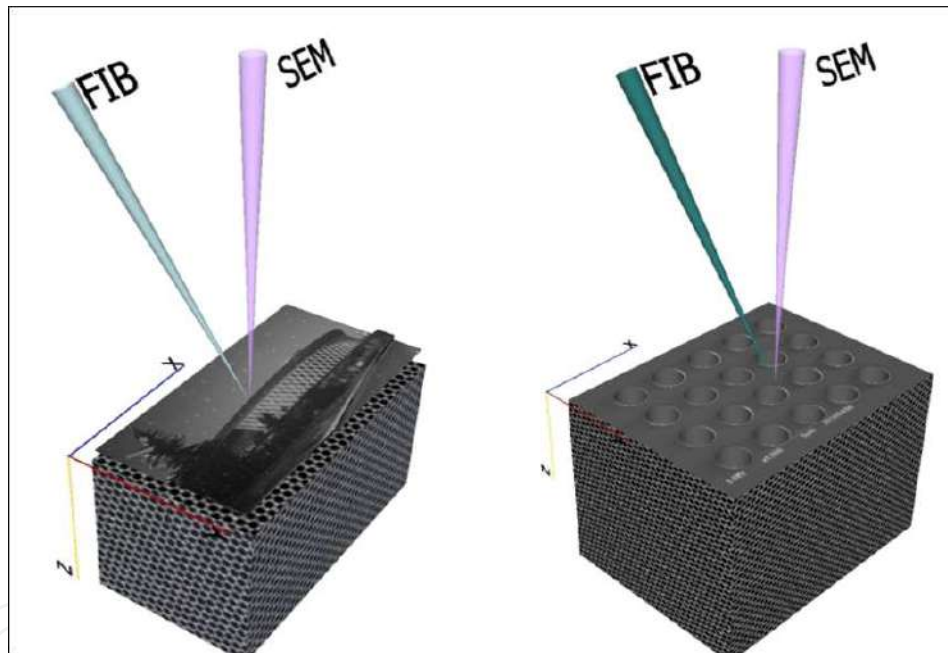


**Figure 7.** Representation of ion milling: maskless lithography and nanostructuring

Milling allows for creating cross sections or developing structures with desired geometries to control not only the lateral position but also local depth. Ion milling can also be described as a “direct writing technique” via etching the material surfaces with the exposure of ion beams. This process is similar to lithography; however, the advantage here is that it does not require the use of masks. Local assisting gases exposed by gas injection systems (GIS) that are integrated into dual-beam platforms can help in enhancing the removal of atoms from the material surfaces. Local gas delivery systems can change the oxidation state of released particles and speed up the milling process, while exposure of gases into the region of interest may also reduce the local redeposition of atoms released from the surface.  $\text{XeF}_2$  and  $\text{I}_2$  are the

most common gases that are used in FIB to enhance ion milling processes, and their supply is usually dependent on the manufacturer.

### 2.3.2. Deposition

Deposition is the second most powerful feature of FIB technologies, as the ion or electron beams can be used in a deposition system, allowing the addition of material instead of removing the material. Deposit materials are often supplied by an internal gas delivery system that locally exposes a chemical compound close to the surface impact point via gas injection systems (GIS) that can be incorporated into dual-beam platforms. The chemical gas compound is usually in the precursor form and consists of organometallic molecules. When this compound is exposed to the region of interest, beams decompose the molecules locally and deposit almost-pure material onto the surface. In other words, gas compound is exposed onto the target specimen and adsorbed on its surface, and this is followed by bombardment of focused beams on the adsorbed molecules within predefined patterns. Finally, as a result of complex beam-induced reactions, gas molecules dissociate into deposits and volatile fragments, while dissociated molecules are adsorbed and deposited into desired structures. This procedure is demonstrated in a scheme in Figure 8.

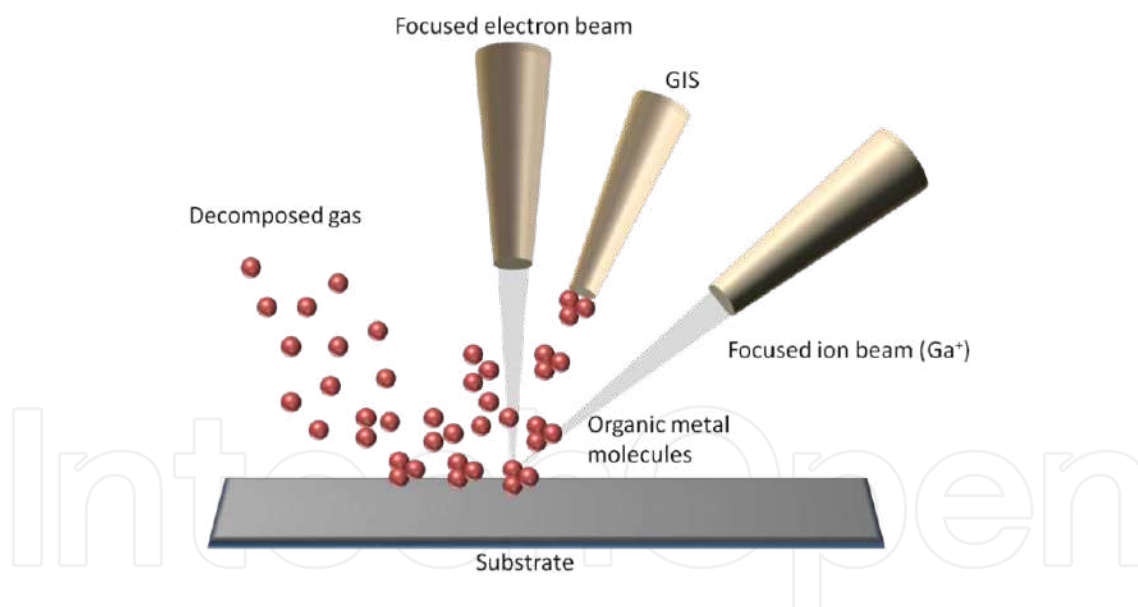


**Figure 8.** Illustration of deposition process in dual-beam instruments via electron beam-induced deposition (EBID) and ion beam-assisted deposition (IBAD)

Usually the decomposition of the precursor molecules is not hundred percent, and therefore some additional matrix molecules (e.g., organic residues) are also deposited together with the diverted material. For this reason, the purity of the deposits is lower when compared to other deposition techniques such as chemical vapor deposition (CVD) or physical vapor deposition (PVD). The materials used for beam-induced deposition in the dual-beam platforms are determined by their different gas chemistries, and several precursor gases are commercially

available for the deposition of Pt, W, SiO<sub>2</sub>, and C provided by different manufacturers and suppliers. There has been already a COST Action (CM 1301 – CELINA) ongoing that aims to develop novel gas chemistries for beam-induced deposition techniques and to perform applications for multidisciplinary sciences using deposition capabilities of precursor materials.

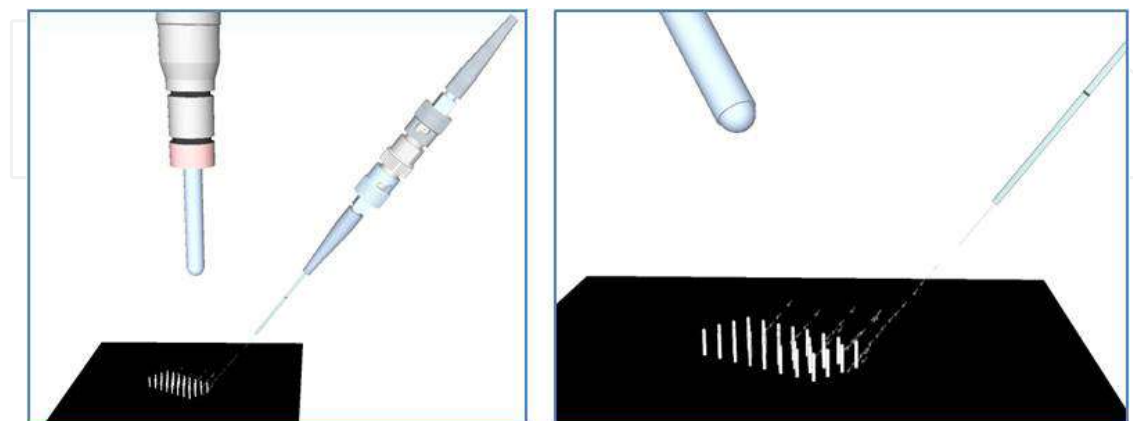


**Figure 9.** Illustration of gas-assisted deposition process

### 3. FIB-based conventional and novel processes

#### 3.1. TEM specimen preparation

One of the most important applications of dual-beam instruments is preparing samples for transmission electron microscopy, as an important capability owing to controlled ion milling abilities is the production of ultrathin and uniform lamellae that are electron-transparent and hence can serve as TEM samples. Advantages of using an FIB for TEM specimen preparation are listed below:

- TEM lamellae can be prepared site-specifically with a spatial accuracy as fine as  $\approx 30$  nm from any region of interest.
- When compared to other techniques (microtomy, low-energy ion milling, dimpling, etc.), the duration for site-specific and ultrathin specimens' preparation process is considerably short, varying from less than 1 hour for noncomplex structures to 4–5 hours for challenging specimens.
- FIB allows for the preparation of TEM samples from both hard and soft materials, regardless of how brittle, ductile, or mechanically sensitive the material is. Even FIB serves for the TEM investigation of samples of life sciences studies when proper conditions of dual-beam systems are maintained (e.g., using cooling stage and cryo-conditions; low ion energy and ion current options), and the experience of the FIB user is sufficient.
- It is possible to develop new methodologies and specific geometries according to the nature and properties of the materials from which TEM specimens are to be prepared. The main

approach in special TEM sample designs is to overcome the limitations and difficulties which can be faced during TEM investigations.

The most common route for TEM specimen preparation is the “in situ lift-out technique,” for which the dual-beam instrument has to be equipped with a micromanipulator unit for allowing the transfer of the lamella to the TEM grid, when both are placed in the microscope chamber at the same time. In this procedure, initially a metal protection layer is coated on the region of interest via beam-induced deposition and two opposing trenches are milled away, leaving behind a 1–2- $\mu\text{m}$ -thin section on the block sample. This section can be named as “pre-lamella.” The next step involves cutting the bottom part and the side trenches away, until the section is held by the bulk sample from its shoulders. Then, this pre-lamella can be welded to the micromanipulator using ion beam-assisted platinum deposition (IBAD) by simultaneously cutting away the shoulders, and can be lifted out from the sample, transferred, and welded to a TEM grid. Afterwards, final thinning and polishing down to a thickness of  $< 100$  nm is achieved using low incident angles and low ion currents. Finally, the sample is ready for TEM analysis. This type of TEM specimen preparation method is demonstrated in Figure 10, giving an example of preparing a cross-sectional lamella from an organic thin film transistor.

In addition to in situ lift-out route, there are many more procedures in the literature that have been developed for more than a decade. Specimen preparation by FIB is often preferred for hard materials (e.g., metals, glass, ceramics) or layered structures (e.g., semiconductors) with hard substrates (silicon, glass, ceramics, etc.) since ion milling is not a proper method for soft materials due to their sensitivity to beam damage and heat-dependent shape distortion. For soft materials, ultramicrotomy is considered to be the most convenient preparation technique, which is a mechanical sectioning process using a diamond knife. As far as TEM investigations for organic and inorganic electronics are concerned, dual-beam instruments are effective for preparation of cross-sections from multilayer integrated devices with hard substrates as the active layer is often very thin (in nanometers) and sandwiched between supporting materials. However, it should be reminded that, for all conditions ion milling and deposition parameters have to be optimized in order to avoid potential ion irradiation damage. Hence, special care should be taken during the entire FIB-based TEM specimen preparation process for minimizing the radiation effects triggered by damage mechanisms mentioned in the previous section (2.2), such as amorphization, gallium implantation, and swelling.

Moreover, when three-dimensional investigations of materials are of interest, TEM tomography-based analysis can be performed. For this type of characterization, the specimen has to be precisely structured so that it has to be representing all its properties of the original material in 3D at the nanometer scale. Such samples can be successfully structured using the capabilities of dual-beam systems, as the details of the corresponding technique are given in the following parts of this section.

### 3.2. Serial slicing and imaging

Dual-beam platforms provide the use of electron and ion beams simultaneously, which opens a way to perform cross sectioning by means of sequential ion milling and monitoring and/or

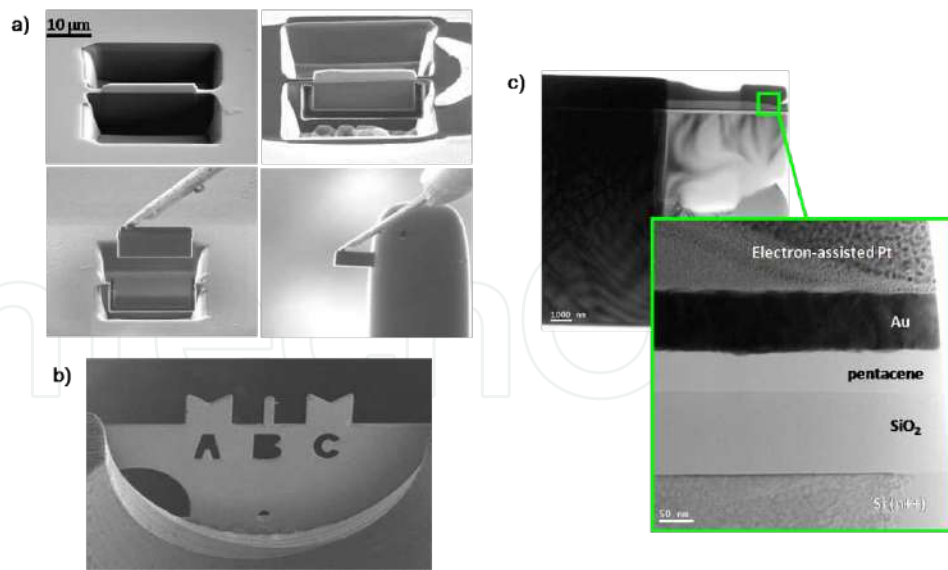


**Figure 10.** TEM specimen preparation of an organic thin film transistor (O-TFT) structure using a dual-beam tool: (a) coarse milling, lift-out, and mounting steps, (b) lamella on a TEM semi-grid, (c) thinned and polished cross-sections investigated by TEM in bright field (BF) mode (images taken at Felmi-Zfe, TU Graz, Austria)

acquiring images of the corresponding cross section of the specimen at the same time using the electron beam. There are mainly two different ways to collect a stack of SEM images of sectioned surfaces: static mode and dynamic mode. In dynamic image acquisition mode, SEM images are acquired in real time during the FIB milling process. In static image acquisition mode, after each slicing, the process is either paused or stopped and therefore slow-scan high-resolution SEM images are acquired.

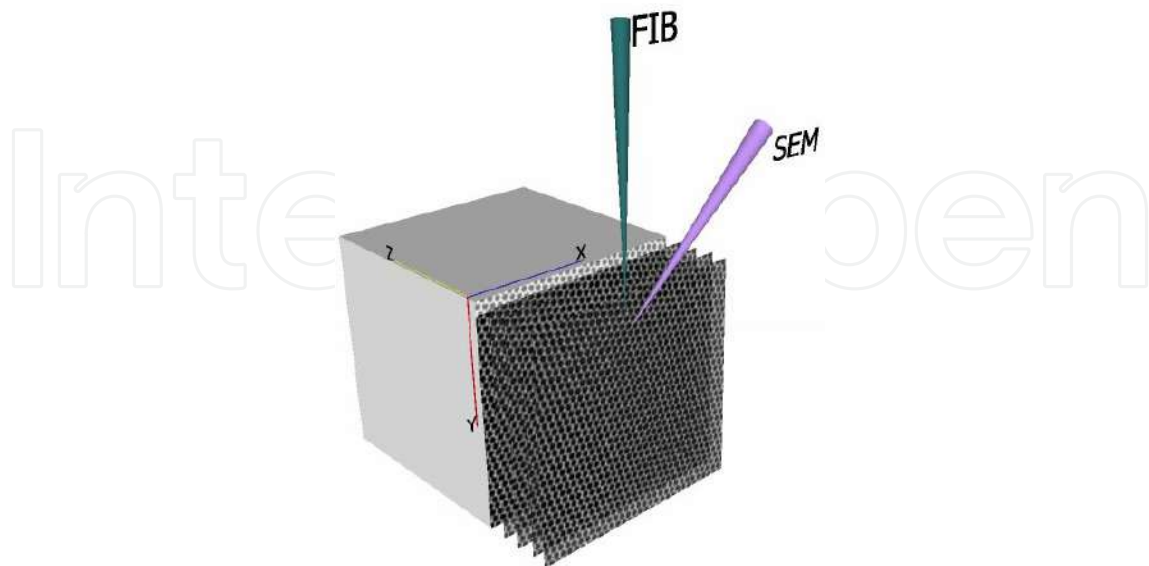


**Figure 11.** Illustration of serial slicing and imaging application of dual-beam platforms. Ion beam is used for creating cross sections, while electron beam allows for monitoring and imaging of the sliced regions.

In particular, the application of this process is very useful for failure analysis of semiconductor devices because it is much faster than TEM specimen preparation. Also rapid monitoring of inner structures of several materials and gaining information of the features down to a few nanometers possible with serial slicing and imaging techniques.

### 3.3. 3D microstructural characterization and FIB tomography

Dual-beam platform also enables three-dimensional information methodologies, especially for quantitative characterization of materials, while the measurement of a number of important geometric properties that cannot be obtained using a 2D analysis can be performed using FIB tomography methods. These are, for instance, the number of features per unit volume, feature connectivity, real feature shapes and sizes, and spatial distribution information.

One step further of serial slicing and imaging application is the 3D FIB tomography, which is based on the principle that continuous 2D data are collected from the surface of the bulk material by serial-sectioning and are stacked together to form reconstructed data, giving information in 3D. By the removal of each section, SE images, BSE images, EBSD maps, and/or EDS data can be acquired from the specimen surface, collected for 3D reconstruction and processed for 3D material characterization. Consequently, dual-beam microscopes are capable of high-fidelity characterization of the morphology, crystallography, and chemistry of micron- and submicron-sized features in 3D. The FIB slicing and HR-SEM imaging-based reconstruction showing the distribution of dentinal tubules in human tooth is shown in Figure 12.

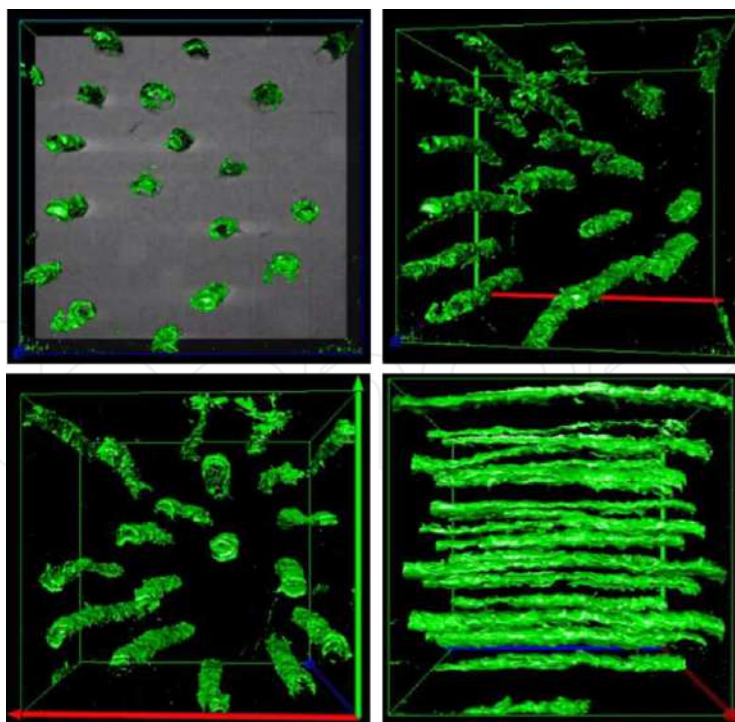


**Figure 12.** The 3D reconstruction of dentin showing the tubule distribution: red arrow corresponds to  $x$ -axis, while blue arrow represents the  $y$ -axis and green arrow the  $z$ -axis. For the reconstruction, Stack N-Viz software was used (reprinted by permission from [7])

### 3.4. Micro-/nano-fabrication, micro-/nano-modification, and other applications

In addition to applications mentioned above, structuring capabilities of dual-beam platforms in small scales fall into two major categories: one is *fabrication* and *machining*, while the other is *rapid prototyping* or *modification* abilities of structures and devices using both ion and electron beam-based processing. For the former, FIB is used for preparing structures that are difficult to form using conventional processes due to material or geometry constraints. The latter, when FIB is utilized, processes can be carried out in more practical and less time-consuming steps than conventional routes. Within user-defined patterns, it is possible to mill away lines down to 10 nm in width, and deposit materials as small as 30 nm by the breakdown of organometallic precursors. The finest ion beam spot size is approximately 5–10 nm, enabling small features to be patterned, while the shape of an FIB cut is dependent on many factors, such as its geometry, milled depth, ion beam profile, and the redeposition of sputtered material.

As already mentioned, FIB provides a very convenient technique for material removal using gallium ions. The advantage of the instrument is that the structure that is to be milled can be predefined as patterns and the process can be performed in an automated way. Milling patterns may be defined in different forms such as scripts, stream files, or image files. However, as already given in the previous section concerning platinum deposition, the quality and the efficiency of the ion milling process are dependent on the instrumental and process parameters, and those have to be optimized for the achievement of the desired structures.

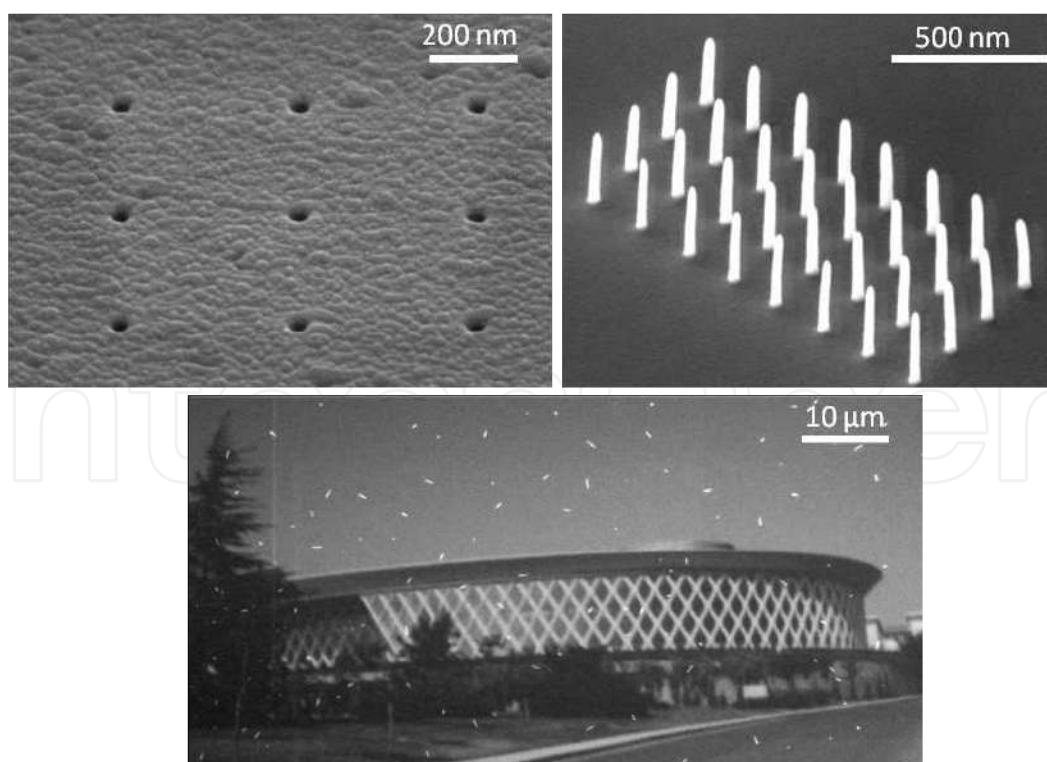


**Figure 13.** Nanostructuring, nano-fabrication and maskless ion lithography examples performed by dual-beam instruments

Recently, FIB technologies are becoming more popular for machining miniaturized samples to investigate the influence of sample dimensions on mechanical properties, in terms of determining size-dependent effects, particularly in metals, alloys, and ceramic composites. Sometimes dual-beam platforms enable not only the fabrication of the test structures but also the application of in situ examination in micro-/nano-size when they are coupled to proper mechanical test stages and nano-indentation devices. The most popular mechanical behavior tests that are recently in application and development include tensile strength and yield strength measurements, giving out the data for deformation in the form of stress–strain curves. The acquired data are very important to get compared to the data in macroscale, for the evaluation of size-dependent effects. Also in situ hardness tests can be performed on the coatings that include applications on several material systems used for multidisciplinary sciences and many fields of industry.

### **3.5. Special sample designs for TEM tomography**

Electron tomography applications are recently becoming more popular for imaging of three-dimensional material systems such as alloys, composites, or samples having spatial features, such as porous network or multicomponents. Especially, in order to reveal the geometric and elemental distribution of material systems that are based on nanostructures, electron tomography applications are being widely used. For this reason, specific sample preparation techniques that keep the original structures of the sections to be investigated at the TEM are often required. Dual-beam technologies provide material-dependent and TEM analysis spectrum-based solutions that are highly rapid, practical, creative, and reliable.

The main approach for novel specimen designs is to overcome the limitations and difficulties (e.g., to be able to acquire only 2D data instead of 3D, projection problem that occurs at TEMs, etc.) that can be faced during electron microscopy-based characterization. In order to investigate the structural properties of these materials in detail, unique electron microscopy techniques and characterization methodologies have to be developed according to the needs and what is expected to be analyzed.

When TEM tomography investigation of a sample is coupled to its FIB slicing and imaging and FIB tomography work, while TEM will be able to provide 3D information at the nanometer scale and below, via FIB tomography sectioning, the information in the scale ranging from micrometers to tens of nanometers will be collected from the identical sample and the data can be comparatively and complementarily evaluated.

One of the solutions for the problems faced during TEM tilt series in tomography applications is the preparation of samples with special geometries that do not cause any projection, thickness variation, and shadowing problems during tilting. This might be a problem for lamellar samples; however, pin-like TEM structures are proper for tilting without any projection or shadowing, as well as this type of sample can represent the three-dimensional nature for the nanocomposite systems or porous materials. Especially, nanoparticles can be kicked out of the matrix during final thinning of ultrathin lamellae and the pores in nano-size can be enlarged with respect to ion bombardment via FIB processing in thin samples. Hence, pin-like structures are found to be more stable both physically and chemically when compared

to lamellar samples. An example for pin-like sample preparation of human dentin using dual-beam instruments is given in Figure 14.

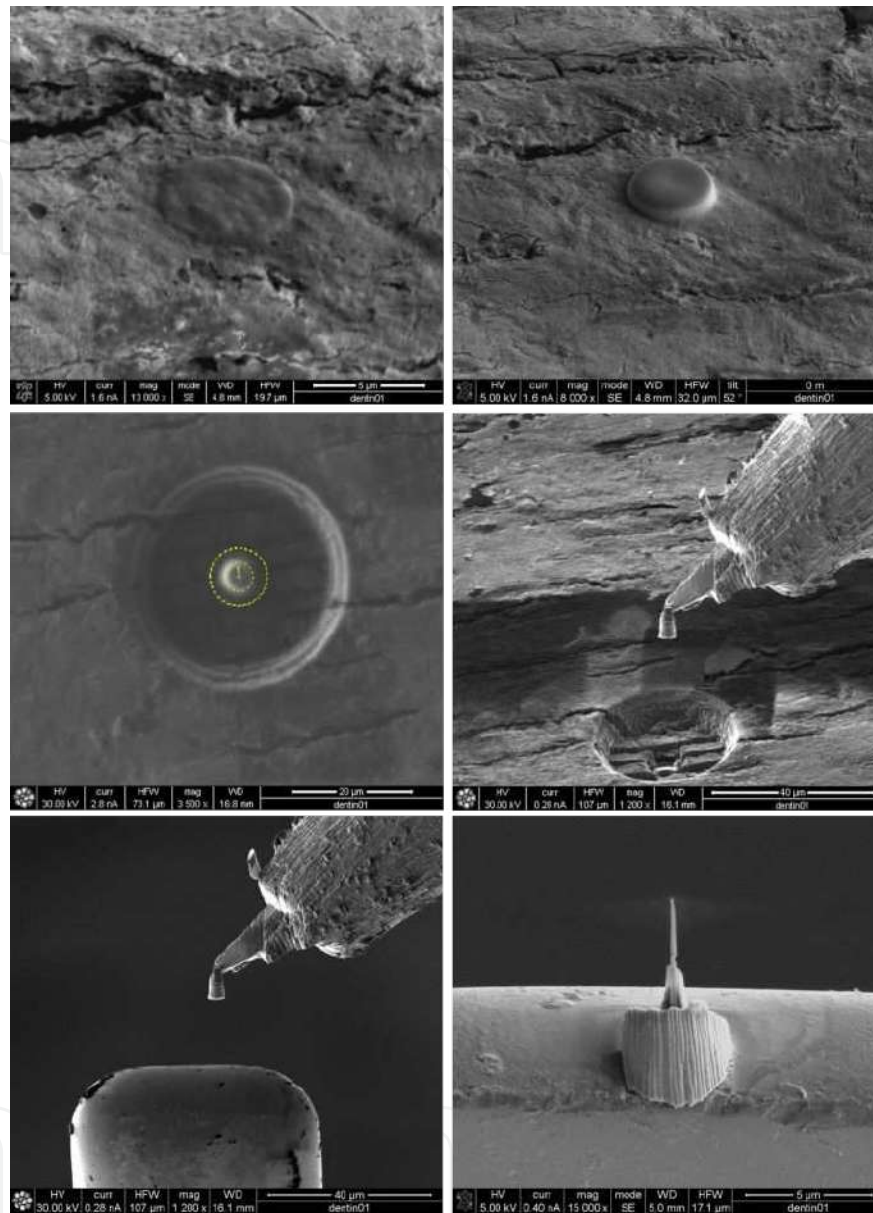


**Figure 14.** The steps for preparation of pin-like TEM sample using the dual-beam instruments: (a) deposition of electron beam-assisted Pt layer, (b) deposition of ion beam-assisted Pt layer, (c) ion beam milling via annular patterns, (d) lift-out of the pre-section, (e) mounting of the pre-section onto the grid; (f) final thinning and polishing (reprinted from [7] by permission)

Pin-like structures investigated by TEM allow for revealing structures in 3D at the nanoscale and below, and when combined to FIB tomography data, the overall results help in observing materials' features at different scales. An example again on human dentin is given in Figure 15 for tracking micro-sized dentinal tubules, and nano-sized collagen fibrils are investigated using FIB slicing/SEM imaging and TEM bright field imaging, respectively.

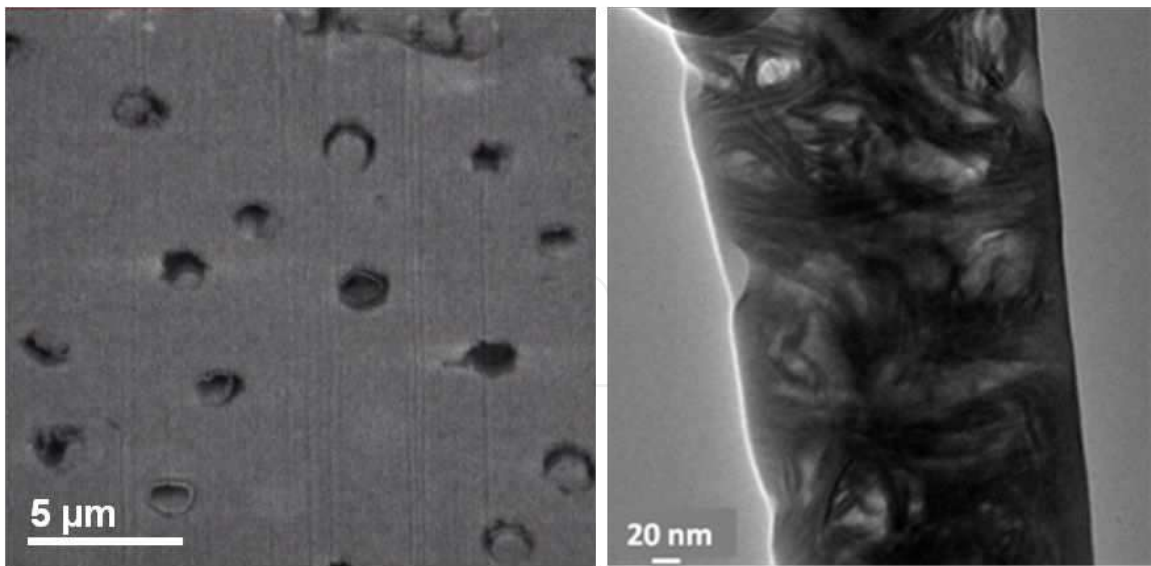


**Figure 15.** FIB slice showing the cross sections of tubules elongated in  $y$ -axis in human dentin and the TEM bright field images showing the 3D distribution of collagen fibrils within the human dentin. The micrographs show the nanostructures within the dentin structure [7].

## Acknowledgements

I would like to cordially thank Dr. Feray Bakan, Sina Sadighikia, and Ertuğrul Bülbül for their valuable help with this book chapter. Also support by Dr. Volkan Özgüz at Sabanci University and my former colleagues at Felmi-Zfe, TU Graz, is gratefully acknowledged. In addition, I owe many thanks to the national TUBITAK projects 112M195 and 114M040, as well as COST Actions MP1103 and CM1301 (CELINA) for providing financial support and collaboration opportunities.

## Author details

Meltem Sezen\*

Sabanci University Nanotechnology Research and Application Center (SUNUM), Orhanlı-Tuzla, Istanbul, Turkey

## References

- [1] Mayer J, Giannuzzi L.A, Kamino T, Michael J. TEM sample preparation and FIB-induced damage. *MRS Bulletin*. 2007; 32: 400–407. DOI: 10.1557/mrs2007.63

- [2] Giannuzzi L.A, Stevie F.A. Introduction to Focused Ion Beams: Instrumentation, Theory, Techniques, and Practice. New York: Springer; 2005. 357 p. DOI: 10.1007/b101190
- [3] Yao N, editor. Focused Ion Beam Systems: Basics and Applications. Cambridge University Press; 2011. 395 p. DOI: 10.1017/CBO9780511600302
- [4] Orloff J, Utlaut M, Swanson L. High Resolution Focused Ion Beams. New York: Kluwer Academic/Plenum Publishers, Springer US; 2002. 303 p. DOI: 10.1007/978-1-4615-0765-9
- [5] Utke I, Hoffmann P, Melngailis J. Gas-assisted focused electron beam and ion beam processing. Journal of Vacuum Science and Technology. B. 2008; 26, 4: 1197–1276. DOI: 10.1116/1.2955728
- [6] Egerton R.F, Li P, Malac M. Radiation damage in the TEM and SEM. Micron. 2004; 35, 6: 399–409. DOI: 10.1016/j.micron.2004.02.003
- [7] Sezen M, Sadighikia S. 3D electron microscopy investigations of human dentin at the micro/nanoscale using focused ion beams based nanostructuring. RSC Advances. 2015; 5: 7196–7199. DOI: 10.1039/C4RA14364G

IntechOpen

# We are IntechOpen, the world's leading publisher of Open Access books Built by scientists, for scientists

6,300

Open access books available

171,000

International authors and editors

190M

Downloads

Our authors are among the

154

Countries delivered to

TOP 1%

most cited scientists

12.2%

Contributors from top 500 universities



WEB OF SCIENCE™

Selection of our books indexed in the Book Citation Index  
in Web of Science™ Core Collection (BKCI)

Interested in publishing with us?  
Contact [book.department@intechopen.com](mailto:book.department@intechopen.com)

Numbers displayed above are based on latest data collected.  
For more information visit [www.intechopen.com](http://www.intechopen.com)



---

## Immunogold Techniques in Electron Microscopy

---

Mogana Das Murtey

Advanced Medical and Dental Institute (AMDI), Universiti Sains Malaysia, Bertam Kepala Batas,  
Penang, Malaysia

---

**Retraction to: Das Murtey M. Immunogold Techniques in Electron Microscopy. In: Janecek M, Kral R, editors. Modern Electron Microscopy in Physical and Life Sciences. Rijeka: IntechOpen; 2016. DOI: 10.5772/61719.**

The publisher is retracting and removing [1] following an authors' request.

The publisher and the authors regret any inconvenience this might have caused to the readership.

### References

[1] Das Murtey M. Immunogold Techniques in Electron Microscopy. In: Janecek M, Kral R, editors. Modern Electron Microscopy in Physical and Life Sciences. Rijeka: IntechOpen; 2016. DOI: 10.5772/61719.

IntechOpen

# We are IntechOpen, the world's leading publisher of Open Access books Built by scientists, for scientists

6,300

Open access books available

171,000

International authors and editors

190M

Downloads

Our authors are among the

154

Countries delivered to

TOP 1%

most cited scientists

12.2%

Contributors from top 500 universities



WEB OF SCIENCE™

Selection of our books indexed in the Book Citation Index  
in Web of Science™ Core Collection (BKCI)

Interested in publishing with us?  
Contact [book.department@intechopen.com](mailto:book.department@intechopen.com)

Numbers displayed above are based on latest data collected.  
For more information visit [www.intechopen.com](http://www.intechopen.com)



---

## Sample Preparations for Scanning Electron Microscopy – Life Sciences

---

Mogana Das Murtey<sup>1</sup>, Patchamuthu Ramasamy<sup>2</sup>

<sup>1</sup>Advanced Medical and Dental Institute (AMDI), Universiti Sains Malaysia, Bertam Kepala Batas, Penang, Malaysia

<sup>2</sup>Quest International University Perak (QIUP), Ipoh, Perak Darul Ridzuan, Malaysia

---

**Retraction to: Das Murtey M, Ramasamy P. ISample Preparations for Scanning Electron Microscopy – Life Sciences. In: Janecek M, Kral R, editors. Modern Electron Microscopy in Physical and Life Sciences. Rijeka: IntechOpen; 2016. DOI: 10.5772/61720.**

The publisher is retracting and removing [1] following an authors' request.

The publisher and the authors regret any inconvenience this might have caused to the readership.

### References

[1] Das Murtey M, Ramasamy P. ISample Preparations for Scanning Electron Microscopy – Life Sciences. In: Janecek M, Kral R, editors. Modern Electron Microscopy in Physical and Life Sciences. Rijeka: IntechOpen; 2016. DOI: 10.5772/61720.

# We are IntechOpen, the world's leading publisher of Open Access books Built by scientists, for scientists

6,300

Open access books available

171,000

International authors and editors

190M

Downloads

Our authors are among the

154

Countries delivered to

TOP 1%

most cited scientists

12.2%

Contributors from top 500 universities



WEB OF SCIENCE™

Selection of our books indexed in the Book Citation Index  
in Web of Science™ Core Collection (BKCI)

Interested in publishing with us?  
Contact [book.department@intechopen.com](mailto:book.department@intechopen.com)

Numbers displayed above are based on latest data collected.  
For more information visit [www.intechopen.com](http://www.intechopen.com)



---

# Evaluation of the Glomerular Filtration Barrier by Electron Microscopy

---

Diogo Benchimol de Souza, Bianca Martins Gregório,  
Marlene Benchimol and Fernanda Amorim de Moraes Nascimento

Additional information is available at the end of the chapter

<http://dx.doi.org/10.5772/61811>

---

## Abstract

The plasma filtration and formation of the urine is a very complex process necessary for the elimination of metabolites, toxins, and excessive water and electrolytes from the body. The initial process of urine formations is done by the glomerular filtration barrier inside the glomeruli. This specialized barrier consists of three layers, fenestrated endothelium, basement membrane, and podocytes, which ensure that water and small molecules pass through while cells and large molecules are retained. The glomerular filtration barrier is found with abnormal morphology in several diseases and is associated with renal malfunction; thus, it is interesting to study these structures in different experimental and clinical conditions. The normal glomerular barrier and its alterations in some conditions (hypertension, diabetes, and fetal programming) are discussed in this chapter. Furthermore, some methods for studying the glomerular filtration barrier by electron microscopy, both by qualitative and quantitative methods, are present.

**Keywords:** Electron microscopy, glomerulus, filtration barrier, morphometry

---

## 1. Introduction

The human kidney is responsible for many functions, such as filtration of the plasma, blood pressure control, and hormonal production among others. Kidneys are bean-shaped organs located in the retroperitoneal space, irrigated by the renal artery, and covered by its fibrous capsule. Renal parenchyma can be distinguished into cortex and medullar regions, with different anatomic–histological characteristics. Inside a human kidney, there are about one million nephrons, which are composed of tubules and renal corpuscles. The corpuscles contain several tortuous arterioles covered by podocytes. The set of the endothelial layer of these

arterioles, its basement membrane, and the podocytes correspond to the glomerular filtration barrier [1, 2].

The ultrafiltration of the plasma by this barrier and formation of the primary urine requires normal glomerular morphology. It is well documented that the podocytes are important to guarantee the selectivity during the filtration process, preventing macromolecules that pass through the slit diaphragm formed between its foot processes. Many studies suggest that alterations on these cells or on the vessels, as those during hypertension, diabetes, or lupus, can reduce the oxygen flux, leading to hypoxia stage, being responsible for podocyte alteration and death [3, 4].

The glomerular filtration barrier morphology has been extensively studied in several experimental and clinical conditions. For this purpose, electron microscopy (both transmission and scanning) suits perfectly for observing the fine structure of this barrier, indicating with accuracy morphological alterations when present [5, 6].

Thus, in this chapter, we aimed (a) to describe the elements of the glomerular filtration barrier, (b) to present scientific examples of how the glomerular filtration barrier elements are related to different clinical and experimental conditions, and (c) to show how the elements of the glomerular filtration barrier can be analyzed by scanning and transmission electron microscopy with qualitative and quantitative methods.

## **2. Main body**

### **2.1. The normal glomerular filtration barrier**

The glomerulus is a highly irrigated structure that performs selective filtration of the plasma. Inside the Bowman's capsule, several tortuous arterioles receive the blood and filtrate it forming the primary urine, which then passes to the proximal tubule. The glomerular capillaries are lined by a fenestrated endothelium, covered externally by specialized cells, called podocytes. Between the cell layers, there is a basement membrane, which also has an important filtering function. Together, the endothelial cells, the basement membrane, and the podocytes form the glomerular filtration barrier [1, 3].

The glomerular filtration barrier is highly permeable to water and small molecules. Moreover, it is slightly permeable to macromolecules and acts as a physical and electrical barrier for the filtration process. These characteristics are dependent of the cellular structures, and its function is influenced by factors such as molecular weight and electric charge [2]. Moreover, changes in the cell junctions of the glomerular barrier prejudice the glomerular function [7].

Internally, the glomerular filtration barrier is constituted by the glomerular fenestrated endothelium. These endothelial cells have a glycocalyx over its luminal surface, which form a highly negatively charged coating [2]. Thus, glycocalyx covers the endothelium and promotes a first selection of molecules passing through the barrier by electric charge. The endothelium coating the glomerular capillaries is very thin and has several fenestrae with 70–90 nm of diameter. These pores can filtrate only large molecules and blood cells [1].

The endothelial cells are supported by a basement membrane (about 100–150 nm), which is the only continuous layer of the glomerular filtration barrier. As this membrane is thought to be the fusion of the endothelial and epithelial basement membranes, two laminae lucida (interna and externa) and, between them, a lamina densa are found [1]. The basement membrane is composed of a complex network of glycosaminoglycans and fibrous proteins (laminin and collagen type IV), which are continuously produced and deposited by podocytes and mesangial cells [8]. These proteins adhere to the cell membranes by surface receptors and form the glomerular filtration barrier [5].

Podocytes are specialized epithelial cells found in the external layer of the glomerular filtration barrier and exhibit several long cellular processes, which bears various secondary processes, named as foot processes. The foot processes involve capillaries by interdigitations, and small gaps are left in between. These small gaps measure about 20–30 nm and is named as slit diaphragm being responsible for passage of small molecules, whereas larger ones are retained [6]. Further, the slit diaphragm is filled with nephrin and podocin, the transmembrane proteins that are also important for the correct function of glomerular filtration barrier. Experimental studies have shown that mutations in expression of these proteins can alter the filtration barrier and probably is the cause of nephrotic syndrome [9].

In addition to adhesion receptors from integrin family, there are also proteoglycan transmembrane receptors such as those of syndecan family. Also, the junction of podocytes membrane is seen by electron microscopy, showing zipper-like structure where binding proteins form cell junctions and small pores, as previously mentioned on filtration slit [6]. Thus, it is important to consider all glomerular ultrastructure in the filtration process and renal function. Some diseases provoke changes in glomerular ultrastructure, which promote irregular filtration rates, proteinuria, and even kidney failure, further discussed here. Electron microscopy and correlate techniques allow better to understand these pathological changes and become an effective and important method in the study of renal function.

## 2.2. The altered glomerular filtration barrier

Literature describes well several diseases that affect the glomerular filtration barrier. Some conditions such as diabetes mellitus, hypertension, and maternal nutritional changes during critical periods of development, known as fetal programming, are well recognized as important risk factors for developing chronic kidney disease.

Diabetes mellitus is one of the most chronic diseases emerging on twenty-first century, in which hyperglycemia is a major indicator, generating microvascular damage such as retinopathy, neuropathy, and kidney disease [4]. Diabetic nephropathy is a chronic progressive disease that affects 20–40% of patients with diabetes mellitus [10]. Histopathologically, this disease in humans courses with the thickening of glomerular and tubular glomerular basement membrane, podocytopenia, mesangial expansion, glomerular, and arteriolar hyalinosis. The earliest clinical manifestation of diabetic nephropathy is microalbuminuria, a strong predictor of renal and cardiovascular disease in patients with type 1 and type 2 diabetes mellitus [11, 12]. These modifications contribute to the abnormal stimulation of resident kidney cells, which increases the production of TGF- $\beta$ 1 and causes collagen (types I, IV, V, and VI), fibronectin,

and laminin depositions in the extracellular matrix of the glomerulus. Thus, this structural disorganization of the glomerular slit diaphragm enhances renal damage and chronic kidney disease progression [13, 14].

Likewise, hypertension is directly related to renal failure [15]. Hypertensive nephropathy, a consequence of chronic increase of blood pressure, is secondary to diabetic nephropathy in terms of diagnosis and is considered the last stage of renal disease. Some complications are associated with hypertensive nephropathy such as glomerular damage resulting in impaired renal function [16]. Hypertension causes an increase of numerous local factors, such as angiotensin II, which may contribute to the development of renal fibrosis. It is reported that angiotensin II stimulates the gene expression of TGF- $\beta$ 1 and the release of this protein. The presence of TGF- $\beta$ 1 activates the conversion of fibroblasts into myofibroblasts, producing large amounts of extracellular matrix components, and induces renal fibrosis [17].

Moreover, angiotensin II regulates the number and integrity of podocyte. In high quantities, it promotes the disintegration and breakup of these highly specialized cells and causes glomerular endothelial cells hypertrophy since it raises intraglomerular pressure, preferably affecting the afferent glomerular arterioles [18]. The increase of blood volume is also capable to reduce the levels of podocin (abundant protein in the podocyte body) and nephrin (a structural component of the slit diaphragm) in the glomerulus, which enhances the glomerular podocyte injury and albuminuria [19].

Recently, experimental and epidemiological studies report that several metabolic disorders manifested in adulthood have their roots dating embryonic periods [20, 21]. Protein or energy restriction during pregnancy induces low birth weight and, consequently, the injury of nephrogenesis, increasing the incidence of chronic kidney disease in adulthood [22]. As previously mentioned, the glomerulus (the most important filtering apparatus in the body) is a highly specialized structure formed by four types of cells: mesangial, endothelial, visceral (podocytes), and parietal epithelial cells. Accordingly, the intrauterine growth restriction induced by maternal protein restriction may cause morphological and functional changes in the glomerulus, thereby decreasing the filtration barrier efficiency with consequent glomerulosclerosis [23].

Just as occurs in diabetic nephropathy, low birth weight promotes glomerulosclerosis [24], expansion of mesangial matrix, hyalinosis, and podocytopenia, which compromises glomerular filtration and facilitates progressive kidney dysfunction [25]. The loss of podocytes may represent the starting point for an irreversible glomerular injury, characterized by proteinuria and glomerular scarring. Transmission electron microscopy analysis revealed that the offspring from maternal low protein diets at 26 weeks of age and at 16 weeks old and presents the effacement of pedicels, the absence of the slit diaphragm, and an increase of glomerular basement membrane thickness, denoting a reduced of barrier efficiency filtration [24, 26].

Another metabolic programming model related to the occurrence of chronic kidney disease in adult life is maternal vitamin D restriction. This vitamin is essential for the development of the nervous system, immune function, skeletal formation, and fetal kidney [27, 28]. Studies in rats showed that vitamin D restriction during critical periods of development has increased the

number of glomerulus, reduced the size of renal corpuscles, and delayed glomerular maturation, further lower expression of WT1 and podocin in adult offspring [28, 29]. These structural and functional adaptations in the glomerulus may progress to chronic kidney disease

### 2.3. Glomerular filtration barrier evaluation

#### 2.3.1. Sample preparation

A very good sample preparation for EM must follow careful cares because small mistakes will be big ones when analyzed by EM. Thus, we can use either old or new approaches when we intend to study not only the glomerulus but also any biological sample.

However, the glomerulus is particularly difficult due to different osmolarities found in each segment of the nephron. Cryofixation, in general, needs much smaller samples sizes than conventional chemical fixation. A freeze-depth of about 10–15  $\mu\text{m}$  is achieved; one exception is high-pressure freezing (HPF). Nowadays, there are new techniques and good, although expensive, equipments commercially available such as high-pressure freezing (HPF), slam freezing, cryoultramicrotomy, freeze-fracture, freeze-etching, and so on. New scanning electron microscopies with high resolution and extreme high resolution that appeared recently provided beautiful and illustrative aspects of all different cell types. Concerning transmission EM, new methodologies allow 3-D reconstruction such as tomography of thick or semithick sections, serial sections, or high-voltage TEMs. In addition, spectacular images were recently obtained with new Helium ion (proton) microscopes.

When sample preparation for the evaluation of the glomerular filtration barrier by electron microscopy follows the standards of routine biological sample preparations, the person should manipulate the tissue with the animal alive, under anesthesia, for obtaining a small fragment with a size of 0.5 mm or even less and immediately immerse it in the fixative. Alternatively, perfusion gives very good results.

When studying biopsy samples of human kidney or whenever the perfusion is not possible or recommendable, fixation by immersion is an adequate option. For this, a small fragment of the renal cortex is collected, washed in buffered solution, and immediately immersed in the fixation solution [30]. This fragment should be collected from the outer part of the renal cortex, avoiding juxtamedullary region where glomeruli are sparser [1]. As routine preparation, fixation of the kidney is done with glutaraldehyde alone or in combination with freshly prepared formaldehyde from paraformaldehyde powder in warm water. The formaldehyde molecule is a very small aldehyde and has the advantage to penetrate rapidly into tissue, although it is not a strong linker for proteins. Thus, a good procedure is its combination with glutaraldehyde since it penetrates more slowly than formaldehyde and provokes cross-links with proteins. However, glutaraldehyde is a slow fixative, and it takes some seconds or even some minutes to cause death to cells and tissues. The small fragments are fixed in 2.5% glutaraldehyde or 4% PF with 2.5% glutaraldehyde, diluted in 0.1 M cacodylate buffer, pH 7.2, overnight at room temperature. Most important, buffered solutions should be used for better preservation of the cellular aspects of the glomerular filtration barrier [30, 31]. In the next day, samples are post-fixed in 0.1 M cacodylate buffer containing 1%  $\text{OsO}_4$  and 0.8% potassium

ferricyanide for 1 h. It is important to point out that potassium ferricyanide is an important approach to better visualize the trilaminar structure of cell membranes. Then samples are dehydrated in graded series of acetone or alcohol. Ultrathin sections obtained after epoxy resin embedding are stained with uranyl acetate and lead citrate and observed in transmission electron microscope.

When studying samples collected from large animal models (i.e., pig, sheep, dog, etc.), the whole kidney can be adequately fixed by perfusion through the renal artery. When studying small species of animals (i.e., rats, mouse, etc.), the whole animal can be perfused through the left ventricle or aorta. In both cases, the researcher may take into account that some fixatives could hamper some other analysis, as for example, perfusing the kidney with glutaraldehyde may prejudice immune-labeling analysis, unless used in very low concentrations such as 0.5% glutaraldehyde or less [31]. We recommend fixation by perfusion in a mixture of glutaraldehyde and freshly prepared formaldehyde because the latter is a fast fixative allowing not only good preservation but also a quick cell death. Whenever using perfusion fixation, the osmolarity of the fixative solution should be taken into account. Preferentially, the osmolarity of the solution for kidney perfusion fixation should be of 420 mOs [32]. After organ perfusion, a small fragment of the renal cortex should be collected and immersed in the fixative solution for postfixation and dehydration as describe by immersion above. It is important to remember removing the renal capsule whenever it is present, allowing the fixative penetrate into the tissue of interest. Also, cryofixation can be an option for sample fixation for glomerular filtration barrier evaluation. One advantage of high-pressure freezing technique is that larger fragments with edges as large as 1 mm can be used, being a good choice as a cryofixation method [31].

As the object of interest is present in the glomerulus, we may take into account that our samples should have at least one glomerulus for examination. The glomerulus of rats has an average area (in its maximum cross section) of  $0.02 \text{ mm}^2$  and occupies around 7.5% of the surface area on renal cortex [33]. Thus, for improving the chance of having a glomerulus on our sample, the examined surface area of the sample should be of at least  $0.5 \text{ mm}^2$  ( $0.02 \times 200 / 7.5$ ). Based on this, the cortical fragment collected for glomerular filtration barrier analysis with electron microscopy should be about  $1 \times 0.5 \times 0.5 \text{ mm}$  in size. Furthermore, as there is no guaranty of having glomeruli in the sample, several fragments must be collected, processed, stored, or fixed.

It is important to point out one step that should not be overtaken: obtaining and observation of semithin sections before the ultrathin sections. Semithin sections are important because it is necessary (a) to confirm that there is a glomerulus in the cutting surface of the sample, (b) to determine whether the pyramid in the block face is correct in size and shape or should centered over a glomerulus, and (c) to observe the hole cutting surface under low magnification and obtain a copy in light microscopy that will be useful for searching glomeruli when this sample is observed with electron microscopy. It is very often that when the semithin sections are observed, the block is taken away as no glomerulus was found on its surface. This reinforces the importance of collecting several fragments of each animal/patient for electron microscopy analysis. Alternatively, electron tomography can be used. For this, thick sections ( $>200 \mu\text{m}$ ) and

intermediate (200–300 kV) or high-voltage (750–1000 kV) EM equipped with a eucentric tilting stage are used. Colloidal gold particles (10 nm) are deposited on surface of the grids, to be used as fiducial markers for alignment of the tilted views. Single-axis tilt series from  $-60^\circ$  to  $60^\circ$  images are collected in  $1^\circ$  increments using TEM coupled to a  $4k \times 4k$  CCD camera. About 400 images are obtained and three dimension reconstruction and data analyses are performed using proper software package as recommended by the EM company.

Sample preparation for SEM requires the same care as for TEM. Aldehyde fixation is adequate, but in order to improve lipid stability, contrast, and electron beam scanning, osmium tetroxide is also used. Sample is dehydrated with the same agents for TEM; however, we prefer to use alcohol starting from 7.5% to three times in 100% to avoid problems of drying artifacts. Next, tissue will critical point dried and coated with a very thin layer of gold or other conductive metal, producing beautiful images but without high resolution.

### 2.3.2. Helium ion microscopy

Recently, the group of Rice et al. [34] used helium ion microscopy (HIM) to analyze the rodent glomeruli and obtained wonderful images of uncoated samples by SEM. The authors used transcatheter perfusion with aldehyde fixatives, vibratome sectioning, gradual dehydration in methanol series, and a very careful critical point drying. There is no need to apply conductive coatings to the samples prior to imaging, and thus sample surface information is preserved. Even at low magnification, the high quality and depth of field of HIM images is impressive. The images obtained with HIM are important and beautiful. The authors depicted some nanoprojections of the foot processes membrane (Figure 1). Also, podocytes and endothelial fenestrae within the filtration slit diaphragm were observed with much more detail (Figure 2). Nanoprotrusions originating from the processes are clearly seen projecting into urinary space. The future will provide much more resolution for biological samples.

### 2.3.3. Qualitative analysis of the elements of the glomerular filtration barrier

The glomerular filtration barrier can be easily evaluated by simple observation with electron microscopy. One aspect commonly evaluated is the loss of characteristic fenestration of the endothelial layer, which has been reported in some medical conditions previously described. By transmission electron microscopy, the endothelial cells are seen lying over the basement membrane and gaps of this layer, which correspond to fenestrae are fewer when compared to normal conditions [1].

The glomerular basement membrane is another part of the barrier easily evaluated with transmission electron microscopy. By routine examination, the membrane thickness can be qualitatively assessed. As the thickness of the membrane is of great importance for proper functioning of the filtration barrier, this is of interest in many studies. In addition, alterations found in basement membrane are highly associated with several diseases, as previously mentioned, reinforcing the importance of study this structure.

Finally, the podocytes, the third layer of the glomerular filtration barrier, are probably the most studied structure of this barrier. One important aspect of these cells is the interlacement formed

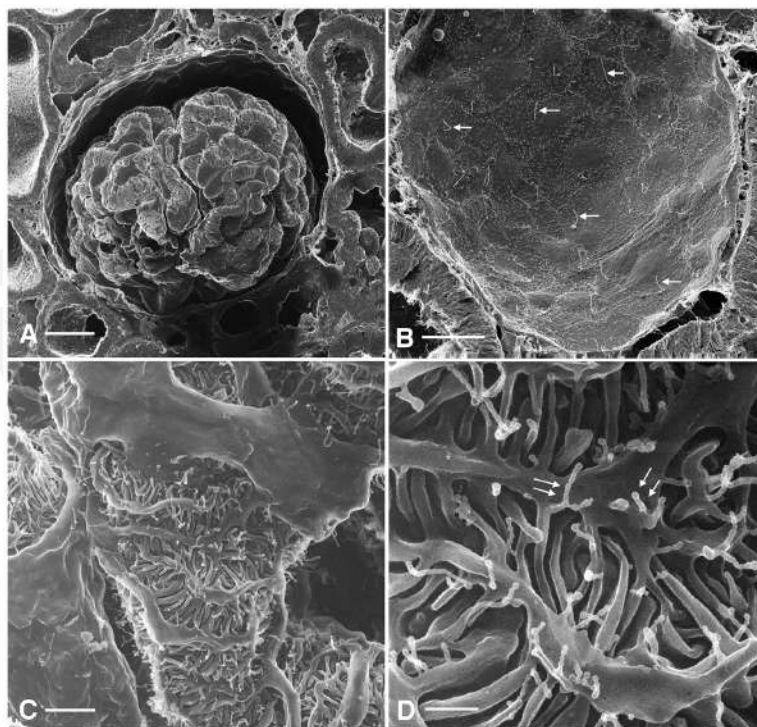


**Figure 1.** Microscopic images of glomerulus of rats as seen by scanning helium ion microscopy. In image A, we see the glomerulus in low magnification and several cut open tubules surrounding the glomerulus. Bar = 20 mm. In image B, the interior of a Bowman's capsule from which the glomerular tuft was removed is observed. Each parietal cell displays a single, long central cilium (arrows) that is very well preserved and visualized without heavy metal coating commonly used in scanning electron microscopy but unnecessary for ion microscopy. Bar = 10 mm. In image C, with intermediate magnification of the surface of a glomerular tuft, it is showed the complex interdigitations of podocytes and their foot processes. Bar = 2 mm. Finally, under higher magnification, it is possible to observe in image D that the podocyte processes are decorated by fine, thread-like protrusions (arrows). Bar = 0.5 mm. Image courtesy of Prof. Dennis Brown [34], available at doi:10.1371/journal.pone.0057051.g001.

by its foot processes, with a small slit diaphragm in between [35]. The alteration of the normal morphology of podocytes and foot processes is named effacement, which has been demonstrated in several conditions [36]. Podocyte effacement is characterized by loss of the normal interdigitations pattern of foot processes, leaving a thinner cell covering a large area outside the basement membrane. As consequence, morphological modifications as fewer and wider foot processes of podocytes are found and can be observed either with transmission or scanning electron microscopy. Among the advantages of observation with scanning electron microscopy are the following: (a) deep field, (b) possibility of analysis of larger areas, allowing the visualization of several podocytes and foot processes in the same sample, and (c) beautiful images of the glomeruli within Bowman's capsule, which are easy to understand and interpret, as shown in figures 3 and 4.

Qualitative differences found in glomerular filtration barrier from individuals submitted to any experimental or clinical condition are only possible when comparison is done with health organisms. However, only qualitative studies do not allow a deeper analysis and statistics and thus lacks scientific excellence. In addition, qualitative observation leads to problems of the

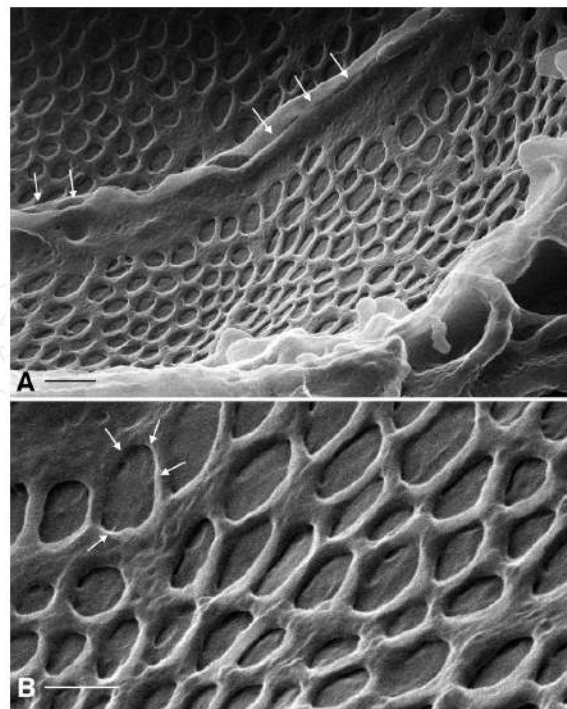


**Figure 2.** Images of glomerular endothelial cells as seen from the capillary luminal side using scanning helium ion microscopy. In image A, note the numerous, round fenestrations present over the entire cell surface. The raised ridges (arrows) represent the location of the tight junction between the two cells. Bar = 175 nm. In image B, under higher magnification, it is possible to observe the details of the fenestrations. In some of them, a substructure consisting of faint spokes like a bicycle wheel can be seen (arrows). Bar = 80 nm. Image courtesy of Prof. Dennis Brown [34], available at [doi:10.1371/journal.pone.0057051.g004](https://doi.org/10.1371/journal.pone.0057051.g004).

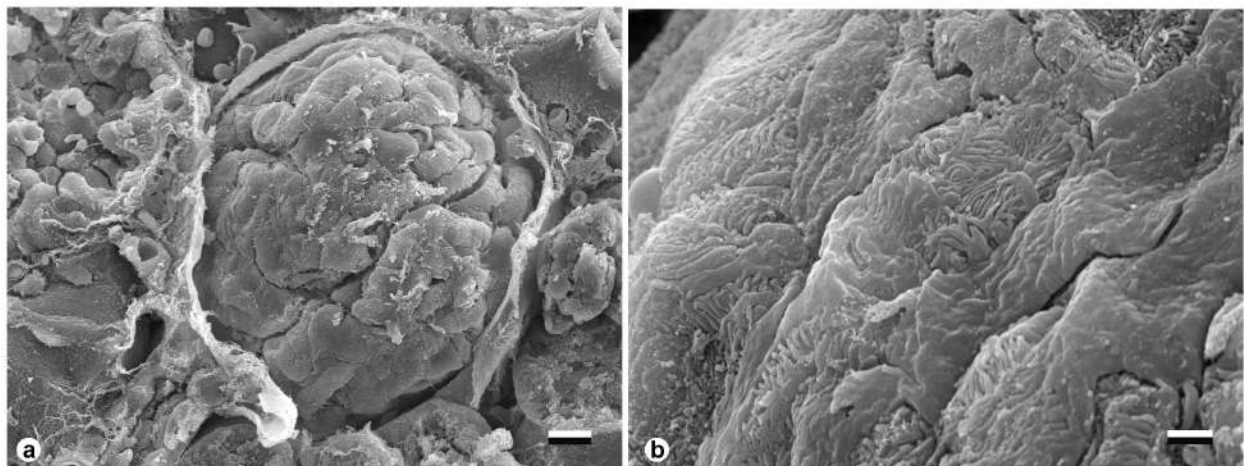


**Figure 3.** Scanning electron microscopic images of glomerulus of rats, showing the podocytes and its foot processes. In image A, under low magnification, we can observe the entire glomeruli with its Bowman's capsule ( $\times 950$ ; 15 kV, scale bar represent 10  $\mu\text{m}$ ). In image B, we can observe several podocytes and foot processes ( $\times 6500$ ; 15 kV, scale bar represent 1.5  $\mu\text{m}$ ).

interpretation due observer expertise [37]. Thus, it is clear that quantitative methods have advantages over those qualitative ones.

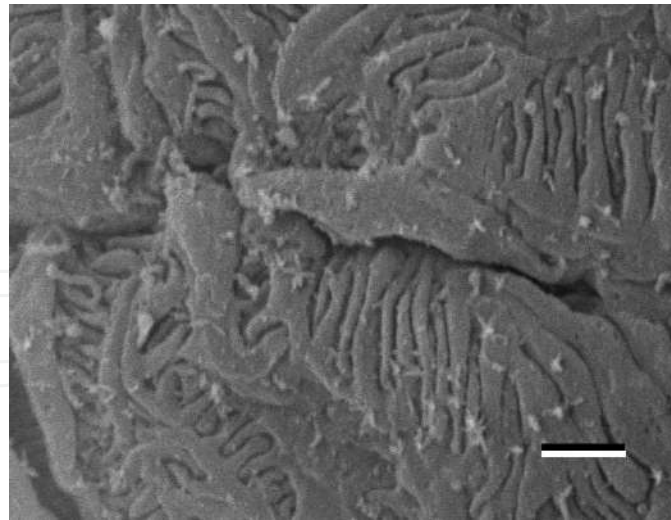


**Figure 4.** Scanning electron microscopic images showing the fine detail of the interdigitating pattern of the foot processes of podocytes at high magnification ( $\times 10,000$ ; 15 kV, scale bar represent 1  $\mu\text{m}$ ).

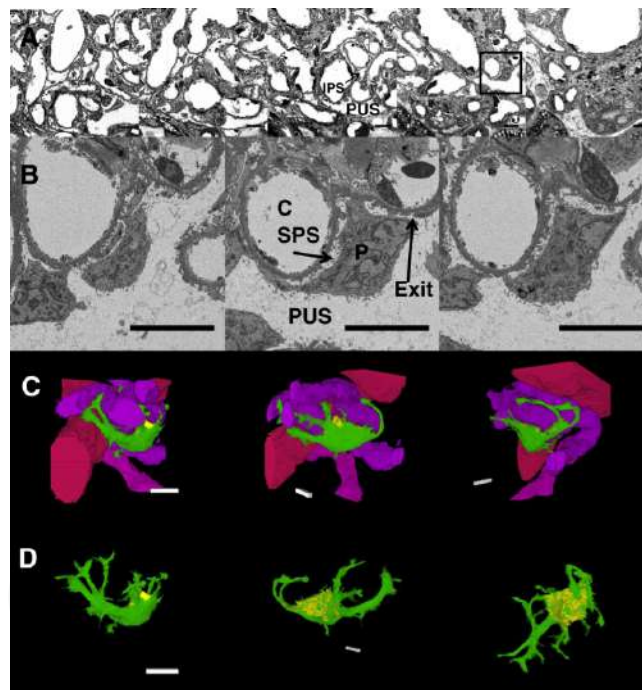


**Figure 5.** Scanning electron microscopy of a human glomerulus after serial block face slicing. In image A, we observe figures that resemble transmission electron micrographs by inverting the signal intensity of the backscattered electron. We see micrographs of complete field of view, with slices 15  $\mu\text{m}$  apart one from another (z). In image B, we observe micrographs of a podocyte of a higher magnification of image A, illustrating the subpodocyte space. In image C, we observe the same podocyte as in image B and adjacent capillaries after highlighting and 3D reconstructing. Finally, in image D, the same podocytes of image C is separated from capillaries after 3D reconstruction, showing the subpodocyte space. P = podocytes, SPS = subpodocyte space, C = capillary lumen, PUS = periphery urinary space, IPS = interpodocyte space, and Exit is an exit region for an SPS. Purple/pink = capillaries, green = podocyte cell body, and yellow = SPS (under the main cell body). Scale bar is 10  $\mu\text{m}$  in all cases. Image courtesy of Prof. Kenton Arkill [38], available at doi:10.1186/1471-2369-15-24.

The glomerular basement membrane was recently observed in three dimensions by different methodologies [38]. In their paper, the authors compared the images and the 3D reconstruction of the glomerular filtration barrier as performed using serial block face scanning electron microscopy, focused ion beam milling scanning electron microscopy, and transmission electron tomography. They reported that the transmission electron tomography technique had the advantage of a higher resolution, with the disadvantages of limited field of view and anisotropic shrinkage. Focused ion beam and serial block face with scanning electron microscopy had greater field of view with lower resolution. The most interesting aspect of these techniques is the reconstruction and digital dissection of cells as demonstrated in Figure 5.

#### *2.3.4. Quantitative analysis of the elements of the glomerular filtration barrier*

The quantification of morphological structures is highly recommended for studying biological alterations in several tissues and different situations. The quantification of morphological aspects of the glomerular filtration barrier is possible and desirable. Translating the morphological aspects of tissues in numbers is very useful from a scientific point of view. It improves the understanding of the modifications of the barrier provoked by different conditions and allows statistical comparisons with other specimens, subjected to different conditions or at different stages of the disease [37]. Based on these premises, methods have been used for different purposes in the study of the glomerular filtration barrier morphology, and important scientific knowledge has been generated from these analyses.

Most quantitative analyses use digital microscopic images that can be digitally acquired or scanned from conventional images. For absolute values (linear measures, for example), it is very important that a scale is maintained on the image. Most electron microscopes automatically print a scale bar on each image, and this is very suitable for morphometric purposes [30].

Several software are eligible for morphometric analyses. In this chapter, we present the steps used in ImageJ 1.37v software. ImageJ is an open source, free software produced and distributed by the National Institutes of Health and can be downloaded at <http://imagej.nih.gov/ij/index.html>.

The different elements of endothelial layer of the glomerular filtration barrier can be objectively evaluated, and the possible loss of fenestrations can be easily assessed by linear measurements in transmission electron microscopy images. For this, we should first calibrate the software for the correct magnification. The straight-line tool should measure the scale bar of the image, and then we should use the option “analyze—set scale.” In the box opened, the distance in pixels should represent the size of the line over the scale bar, and one should insert the real size of the bar at “known distance” space. The “unit of length” space should be fulfilled with the unit of the scale bar ( $\mu\text{m}$  or  $\text{nm}$ ). When one intend to measure several images, all of them should be acquired under the same conditions (magnification, resolution, size, etc.), and the option “global” can be marked. By this, the same configuration may be used for all following micrographs. Figure 6 shows the above-mentioned steps.

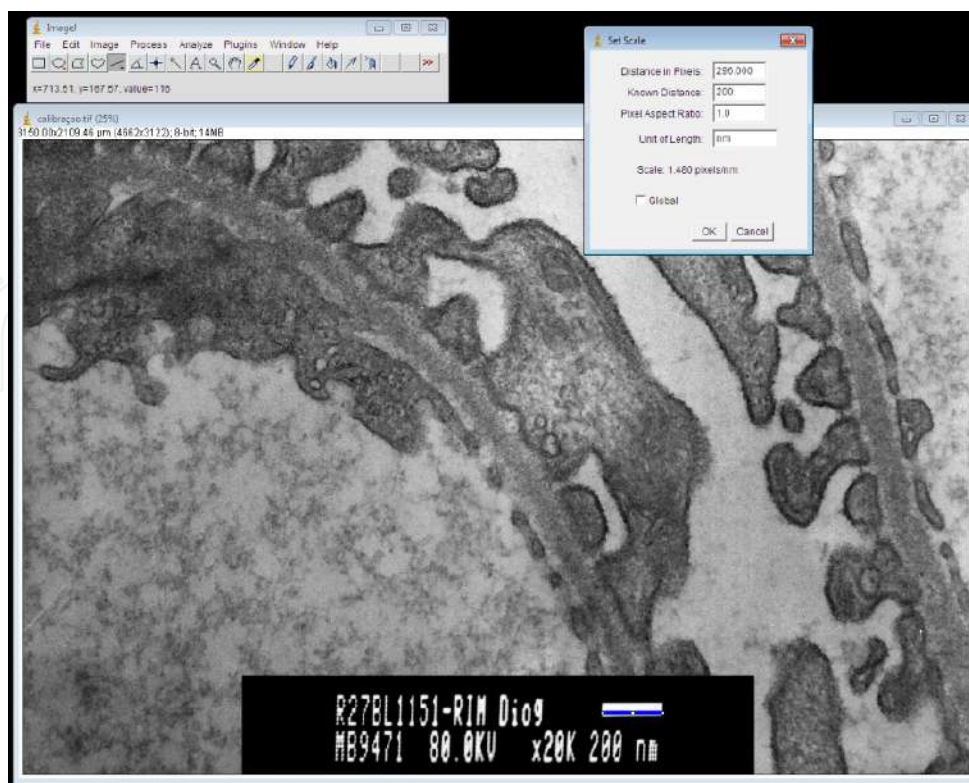


**Figure 6.** Transmission electron microscopy used to demonstrate how to calibrate the software for correct magnification of the micrograph with ImageJ software. The straight-line tool (in blue) is used to measure the scale bar, which here is 200 nm. Next, in the “set scale” box, one can see the distance in pixels of the blue line, and the space of “known distance” is fulfilled with 200 whereas “unit of length” with nm. After clicking “OK,” any measurement in this image will be at nanometers calibrated for the real size.

After the software calibration for the magnification, the straight-line tool is used to measure (“Analyze—measure”) the linear distance of endothelial cells and their fenestrations. The results, expressed in the unit of the scale bar, appear sequentially in the “results” window, and can be easily copied to spreadsheet or statistic software, as seen in Figure 7. One can further compare (a) the size of fenestrations, (b) the endothelial layer, and (c) their proportion (size of fenestrations/size of the endothelial layer). It is also possible to count the number of fenestrations observed on each image and divide by the linear size of the entire filtration barrier present on the image and thus obtain the number of fenestrations per distance. In addition, the thickness of endothelial cells can be measured by applying the straight-line perpendicular to basement membrane, in some randomly chosen points. One should consider that several measurements should be performed to obtain the whole thickness of endothelial layer, as it can greatly vary in the same glomerulus [39].

Furthermore, the glycocalyx that covers the endothelial cells can be studied with some special techniques. Because conventional methods do not stain the glycocalyx since it is mainly composed of proteoglycans, glycosaminoglycan, and hyaluronan, some techniques were developed for its identification. Perfusion with negatively charged lipid particles allows observation of these intralipids inside the capillary lumen. The measurement of linear distance from these intralipids to the endothelial inner membrane reflects glycocalyx thickness. When

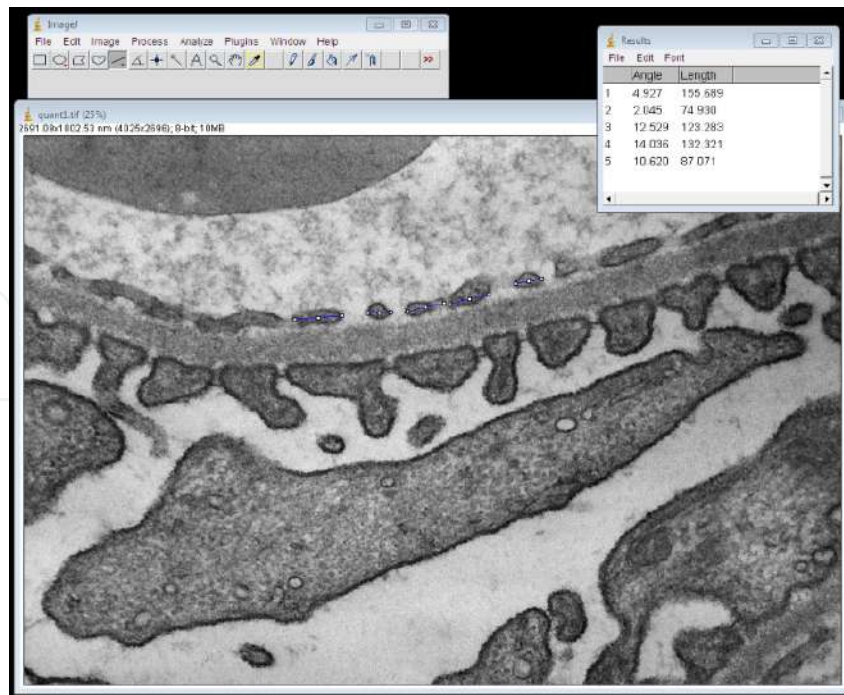


**Figure 7.** The linear distance of the endothelial cells can be measured with the straight-line tool of ImageJ software. In this electron micrograph, blue lines measure some endothelium segments, and the result is seen in the upper right corner. In the results box, the length of each measurement is expressed in nanometers because the image was previously calibrated for the real size.

reduction of glycocalyx thickness occurs, as measured by this method, correlation with proteinuria is thought, as this structure is one of the responsible for the filtration of plasma proteins [40,41].

Furthermore, the number of the endothelial cells per glomerulus can be measured using stereological methods. This needs determination of the glomerular volume (by the Cavalieri principle, disector technique, or volume-weighted methods), the cellular density of glomerulus (counting cell nuclei by the Weibel and Gomez point-counting method), and the proportion of cell types of the glomerulus (also by the point-counting method) [40,41]. These measurements can be assessed with light microscopy with the benefits of a faster and cheaper method, or by electron microscopy with the advantage of being a more accurate method.

Regarding the basement membrane, despite its importance for the plasma filtration, the most commonly measurement performed is membrane width. This directly reflects the membrane thickness that occurs in several diseases and is easily and accurately assessed with transmission electron microscopy images. For this, after calibration for the magnification, the straight-line tool of ImageJ should be used perpendicularly to the membrane, as seen in Figure 8.

The effacement of the podocytes, which is commonly qualitatively assessed, can be objectively assessed by two methods [33]. In transmission electron microscopy images, the linear size of the foot processes touching and parallel to the basement membrane can be measured by the straight-line tool, as shown in Figure 9a. As the podocyte effacement is characterized by the loss of the normal interdigitating pattern, with fewer and larger foot processes, in this

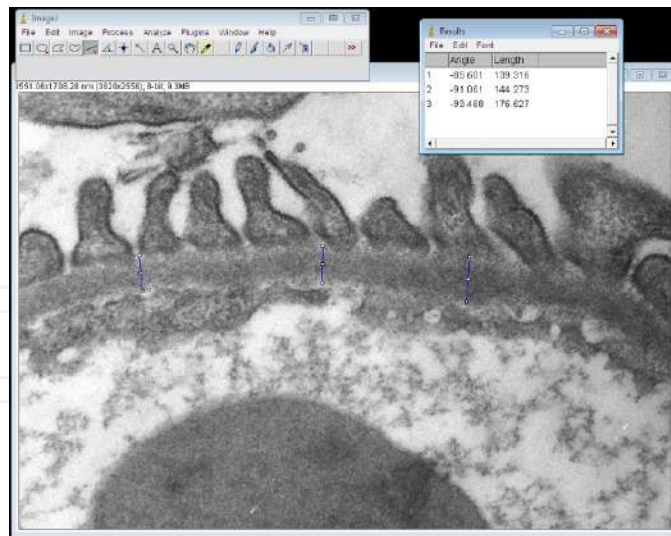


**Figure 8.** The basement membrane width easily measured in transmission electron micrographs using the “straight line” tool of the ImageJ software. In this image, blue lines measure the basement membrane width, and the result is seen in upper right corner of the image. After calibration of the software, each basement membrane measurement is expressed in nanometers in the results box.

condition, these processes present a higher area touching the basement membrane. Thus, the increased linear size measured by this method numerically represents the podocyte effacement. In addition, one can determine the number of slit diaphragm divided by the linear size of the entire filtration barrier present on the image, and the number of slit diaphragm per distance is obtained (Figure 9b), which is also reduced in podocyte effacement. Also, the number of foot processes per distance can be measured by the same method, as used by Jonsson et al. [42], who quantitatively demonstrated the podocytes effacement, as observed in Figure 10. The size of slit diaphragm can be also easily measured using the straight-line tool applied parallel to the basement membrane, after software calibration.

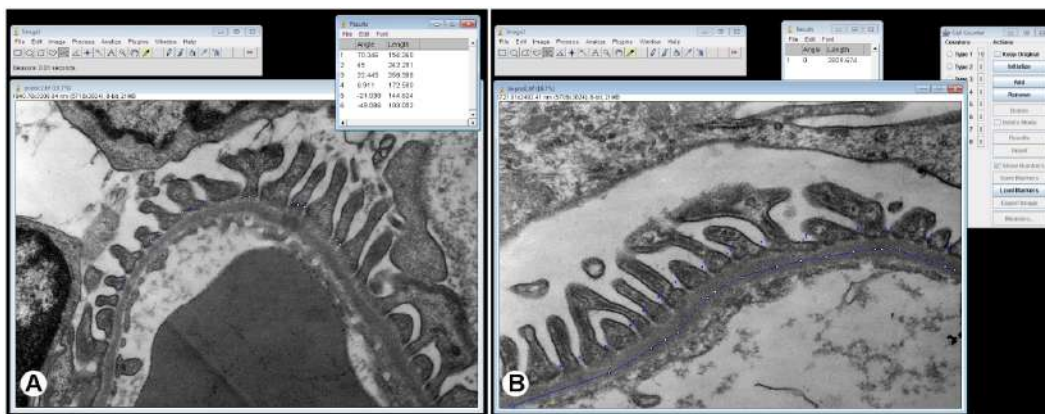


**Figure 9.** Measurement of foot process parameters that relate with podocyte effacement using transmission electron micrographs. In image A, the linear size of the foot processes that touch the basement membrane is measured by the straight-line tool. Several foot processes can be measured for this parameter. In image B, slit diaphragms can be counted using the “cell counter” tool of ImageJ and the linear size of basement membrane, measured with the “Segmented line selections” tool.

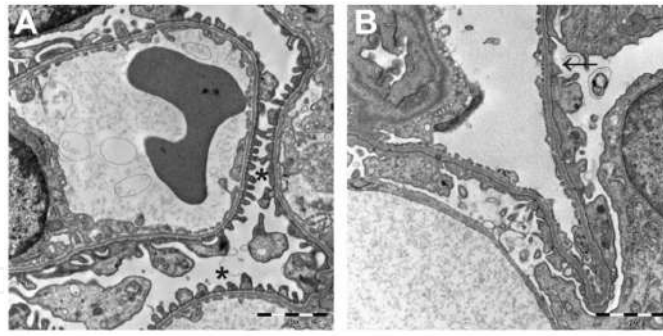


**Figure 10.** Transmission electron microscopic images of control mice and animals with passive Heymann nephritis. In image A, we see the normal glomerular filtration barrier (\*) in control animals. In image B, from mice that received an injection of Anti-Fx1A IgG antibody to induce passive Heymann nephritis, it is possible to observe a high degree of foot process effacement (arrow). Scale bar = 2  $\mu$ m. Image courtesy of Prof. Annika Lindskog Jonsson [42], available at doi:10.1371/journal.pone.0087816.g004.

In scanning electron microscopy images, the number of foot processes per podocyte can also be measured. This parameter only could be determined in podocytes that can be entirely visualized in the scanning image, and special attention should be taken for not count the foot process of the adjacent cell. This makes this method time consuming but can be an option when only scanning electron microscopy is available. In addition, the size of the foot process can be measured in these images, however, with fewer accuracy than when measured in transmission electron microscopy images (Figure 11). Finally, the number of podocytes per glomerulus can be determined using the same method described for determination of endothelial cells per glomerulus.

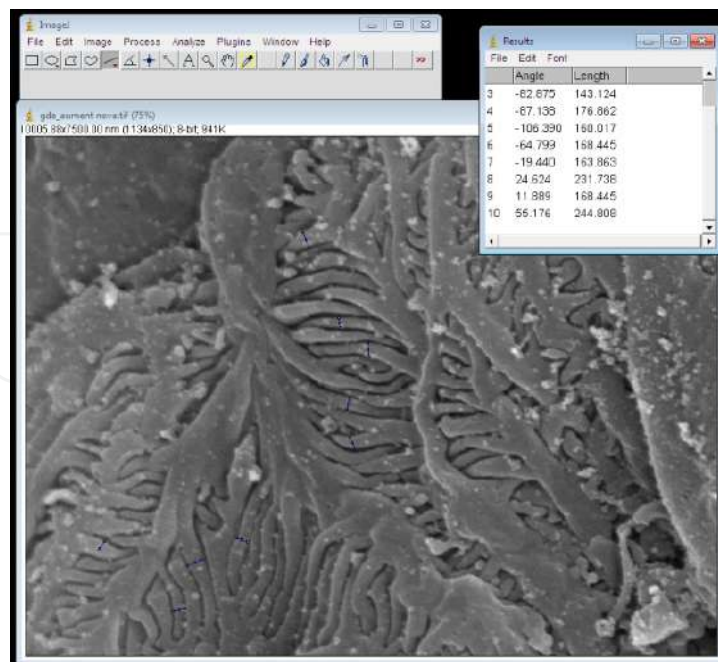


**Figure 11.** The foot processes can also be measured in scanning electron micrographs with the straight-line tool of ImageJ software after calibration for the correct magnification.

### 3. Conclusions

The glomerular filtration barrier is a main component for the filtration of the plasma and formation of primary urine. It is composed of specialized cells and noncellular structures that, together, can avoid the loss of important plasma components but permit the passage of water and undesirable molecules. For this functionality, this barrier has a specific morphology with a fenestrated endothelium covered with glycocalyx, a basement membrane, and a set of slit diaphragms formed by the foot processes of podocytes.

The glomerular filtration barrier morphology has been studied in several diseases and is directly associated with kidney malfunction. Furthermore, it is very important to study this barrier under different clinical and experimental situations. Morphological alterations of components explain some physiopathological findings in clinical setting and correlate with kidney function. For this, scanning and transmission electron microscopy suits perfectly for obtaining high-quality images of this barrier.

Several studies qualitatively described the alterations of glomerular filtration membrane. This gives valuable information, especially when reporting clinical cases or individual lesions that could not be compared. However, when the purpose of the study is to compare the results of a group of individuals with another, quantitative analysis is more appropriate. In this chapter, we presented some objective methods for easy evaluation glomerular filtration membrane. Results obtained with these methods generate numerical data that can be statistically compared with other groups, in different phases of the disease, after some treatment, etc. Thus, whenever possible, quantitative analysis of the glomerular filtration barrier should be favored.

### Author details

Diogo Benchimol de Souza<sup>1\*</sup>, Bianca Martins Gregório<sup>1</sup>, Marlene Benchimol<sup>2</sup> and Fernanda Amorim de Moraes Nascimento<sup>1,3</sup>

\*Address all correspondence to: diogobenchimol@gmail.com

1 Urogenital Research Unit, Department of Anatomy, State University of Rio de Janeiro, Rio de Janeiro, Brazil

2 Unigranrio University, Rio de Janeiro, Brazil

3 Basic Nutrition and Dietetics Nucleus, Federal University of Rio de Janeiro, Macaé, Brazil

### References

- [1] Bloom W, Fawcett DW. A Textbook of Histology. 10th ed. Philadelphia: Saunders; 1975.

- [2] Jarad G, Miner JH. Update on the glomerular filtration barrier. *Curr Opin Nephrol Hypertens*. 2009;18:226–232. DOI: 10.1097/MNH.0b013e3283296044
- [3] Mundel P, Kriz W. Structure and function of podocytes: an update. *Anat Embryol (Berl)*. 1995;192:385–397. DOI: 10.1007/BF00240371
- [4] Wild S, Roglic G, Green A, Sicree R, King H. Global prevalence of diabetes: estimates for the year 2000 and projections for 2030. *Diabetes Care*. 2004;27:1047–1053. DOI: 10.2337/diacare.27.5.1047
- [5] Mould AP, Craig SE, Byron SK, Humphries MJ, Jowitt TA. Disruption of integrin-fibronectin complexes by allosteric but not ligand-mimetic inhibitors. *Biochem J*. 2014;464:301–313. DOI: 10.1042/BJ20141047
- [6] Relle M, Cash H, Brochhausen C, Strand D, Menke J, Galle PR, et al. New perspectives on the renal slit diaphragm protein podocin. *Mod Pathol*. 2011;24:1101–1110. DOI: 10.1038/modpathol.2011.58
- [7] Inoue K, Ishibe S. Podocyte endocytosis in the regulation of the glomerular filtration barrier. *Am J Physiol Renal Physiol*. 2015;309:F398-F405. DOI: 10.1152/ajprenal.00136.2015
- [8] Lennon R, Randles MJ, Humphries MJ. The importance of podocyte adhesion for a healthy glomerulus. *Front Endocrinol (Lausanne)*. 2014;5:160. DOI: 10.3389/fendo.2014.00160
- [9] Craici IM, Wagner SJ, Weissgerber TL, Grande JP, Garovic VD. Advances in the pathophysiology of pre-eclampsia and related podocyte injury. *Kidney Int*. 2014;86:275–285. DOI: 10.1038/ki.2014.17
- [10] Gaede P, Lund-Andersen H, Parving HH, Pedersen O. Effect of a multifactorial intervention on mortality in type 2 diabetes. *N Engl J Med*. 2008;358:580–591. DOI: 10.1056/NEJMoa0706245
- [11] Kannel WB, Stampfer MJ, Castelli WP, Verter J. The prognostic significance of proteinuria: the Framingham study. *Am Heart J*. 1984;108:1347–1352. DOI: 10.1016/0002-8703(84)90763-4
- [12] Yuyun MF, Dinneen SF, Edwards OM, Wood E, Wareham NJ. Absolute level and rate of change of albuminuria over 1 year independently predict mortality and cardiovascular events in patients with diabetic nephropathy. *Diabet Med*. 2003;20:277–282. DOI: 10.1046/j.1464-5491.2003.00940.x
- [13] Schena FP, Gesualdo L. Pathogenetic mechanisms of diabetic nephropathy. *J Am Soc Nephrol*. 2005;16 Suppl 1:S30–33. DOI: 10.1681/ASN.2004110970
- [14] Tryggvason K, Patrakka J, Wartiovaara J. Hereditary proteinuria syndromes and mechanisms of proteinuria. *N Engl J Med*. 2006;354:1387–1401. DOI: 10.1056/NEJM-ra052131

- [15] Pistoia F, Sacco S, Degan D, Tiseo C, Ornello R, Carolei A. Hypertension and stroke: epidemiological aspects and clinical evaluation. *High Blood Press Cardiovasc Prev*. DOI: 10.1007/s40292-015-0115-2
- [16] Bidani AK, Griffin KA. Long-term renal consequences of hypertension for normal and diseased kidneys. *Curr Opin Nephrol Hypertens*. 2002;11:73–80. DOI: 10.1097/00041552-200201000-00011
- [17] Lan HY. Diverse roles of TGF-beta/Smads in renal fibrosis and inflammation. *Int J Biol Sci*. 2011;7:1056–1067. DOI: 10.7150/ijbs.7.1056
- [18] Kato T, Mizuguchi N, Ito A. Blood pressure, renal biochemical parameters and histopathology in an original rat model of essential hypertension (SHRSP/Kpo strain). *Biomed Res*. 2015;36:169–177. DOI: 10.2220/biomedres.36.169
- [19] Le Jemtel TH, Rajapreyar I, Selby MG, Payne B, Barnidge DR, Milic N, et al. Direct evidence of podocyte damage in cardiorenal syndrome type 2: preliminary evidence. *Cardiorenal Med*. 2015;5:125–134. DOI: 10.1159/000375130
- [20] Barker DJ, Forsen T, Uutela A, Osmond C, Eriksson JG. Size at birth and resilience to effects of poor living conditions in adult life: longitudinal study. *BMJ*. 2001;323:1273–1276. DOI: 10.1136/bmj.323.7324.1273
- [21] Gregorio BM, Souza-Mello V, Carvalho JJ, Mandarim-de-Lacerda CA, Aguila MB. Maternal high-fat intake predisposes nonalcoholic fatty liver disease in C57BL/6 offspring. *Am J Obstet Gynecol*. 2010;203:495 e1–8. DOI: 10.1016/j.ajog.2010.06.042
- [22] Hoy WE, Douglas-Denton RN, Hughson MD, Cass A, Johnson K, Bertram JF. A stereological study of glomerular number and volume: preliminary findings in a multi-racial study of kidneys at autopsy. *Kidney Int Suppl*. 2003;63:S31-S37. DOI: 10.1046/j.1523-1755.63.s83.8.x
- [23] Ikezumi Y, Suzuki T, Karasawa T, Yamada T, Hasegawa H, Nishimura H, et al. Low birthweight and premature birth are risk factors for podocytopenia and focal segmental glomerulosclerosis. *Am J Nephrol*. 2013;38:149–157. DOI: 10.1159/000353898
- [24] Sene Lde B, Mesquita FF, de Moraes LN, Santos DC, Carvalho R, Gontijo JA, et al. Involvement of renal corpuscle microRNA expression on epithelial-to-mesenchymal transition in maternal low protein diet in adult programmed rats. *PLoS One*. 2013;8:e71310. DOI: 10.1371/journal.pone.0071310
- [25] Hodgins JB, Rasoulpour M, Markowitz GS, D'Agati VD. Very low birth weight is a risk factor for secondary focal segmental glomerulosclerosis. *Clin J Am Soc Nephrol*. 2009;4:71–76. DOI: 10.2215/CJN.01700408
- [26] Villar-Martini VC, Carvalho JJ, Neves MF, Aguila MB, Mandarim-de-Lacerda CA. Hypertension and kidney alterations in rat offspring from low protein pregnancies. *J Hypertens Suppl*. 2009;27:S47-S51. DOI: 10.1097/01.hjh.0000358838.71675.5e

- [27] Lapillonne A. Vitamin D deficiency during pregnancy may impair maternal and fetal outcomes. *Med Hypotheses*. 2010;74:71–75. DOI: 10.1016/j.mehy.2009.07.054
- [28] Nascimento FA, Ceciliano TC, Aguila MB, Mandarim-de-Lacerda CA. Maternal vitamin D deficiency delays glomerular maturity in F1 and F2 offspring. *PLoS One*. 2012;7:e41740. DOI: 10.1371/journal.pone.0041740
- [29] Maka N, Makrakis J, Parkington HC, Tare M, Morley R, Black MJ. Vitamin D deficiency during pregnancy and lactation stimulates nephrogenesis in rat offspring. *Pediatr Nephrol*. 2008;23:55–61. DOI: 10.1007/s00467-007-0641-9.
- [30] Maunsbach AB, Afzelius BA. *Biomedical Electron Microscopy. Illustrated Method and Interpretations*. London: Academic Press; 1999.
- [31] Souza W. *Técnicas de microscopia eletrônica aplicadas às ciências biológicas*. 3rd ed. Rio de Janeiro: Soc. Bras. Microsc; 2007.
- [32] Bone Q, Denton EJ. The osmotic effects of electron microscope fixatives. *J Cell Biol*. 1971;49:571–581. DOI: 10.1083/jcb.49.3.571
- [33] Souza DB, Costa WS, Cardoso LE, Benchimol M, Pereira-Sampaio MA, Sampaio FJ. Does prolonged pneumoperitoneum affect the kidney? Oxidative stress, stereological and electron microscopy study in a rat model. *Int Braz J Urol*. 2013;39:30–36. DOI: 10.1083/jcb.49.3.571
- [34] 34. Rice WL, Van Hoek AN, Paunescu TG, Huynh C, Goetze B, Singh B, et al. High resolution helium ion scanning microscopy of the rat kidney. *PLoS One*. 2013;8:e57051. DOI:10.1371/journal.pone.0057051
- [35] Shirato I. Podocyte process effacement in vivo. *Microsc Res Tech*. 2002;57:241–246. DOI: 10.1002/jemt.10082
- [36] Wagner MC, Rhodes G, Wang E, Pruthi V, Arif E, Saleem MA, et al. Ischemic injury to kidney induces glomerular podocyte effacement and dissociation of slit diaphragm proteins Neph1 and ZO-1. *J Biol Chem*. 2008;283:35579–35589. DOI: 10.1074/jbc.M805507200
- [37] Felix-Patricio B, De Souza DB, Gregório BM, Costa WS, Sampaio FJ. How to quantify penile corpus cavernosum structures with histomorphometry: comparison of two methods. *Biomed Res Int*. DOI: 10.1155/2015/832156
- [38] Arkill KP, Qvortrup K, Starborg T, Mantell JM, Knupp C, Michel CC, et al. Resolution of the three dimensional structure of components of the glomerular filtration barrier. *BMC Nephrol*. 2014;15:24. DOI: 10.1186/1471-2369-15-24
- [39] Hjalmarsson C, Johansson BR, Haraldsson B. Electron microscopic evaluation of the endothelial surface layer of glomerular capillaries. *Microvasc Res*. 2004;67:9–17. DOI: 10.1016/j.mvr.2003.10.001

- [40] Andersson M, Nilsson U, Hjalmarsson C, Haraldsson B, Nystrom JS. Mild renal ischemia-reperfusion reduces charge and size selectivity of the glomerular barrier. *Am J Physiol Renal Physiol.* 2007;292:F1802-F1809. DOI: 10.1152/ajprenal.00152.2006
- [41] Steffes MW, Schmidt D, McCrery R, Basgen JM. Glomerular cell number in normal subjects and in type 1 diabetic patients. *Kidney Int.* 2001;59:2104–2113. DOI: 10.1046/j.1523-1755.2001.00725.x
- [42] Jonsson AL, Granqvist A, Elvin J, Johansson ME, Haraldsson B, Nystrom J. Effects of melanocortin 1 receptor agonists in experimental nephropathies. *PLoS One.* 2014;9:e87816. DOI: 10.1371/journal.pone.0087816

IntechOpen

# We are IntechOpen, the world's leading publisher of Open Access books Built by scientists, for scientists

6,300

Open access books available

171,000

International authors and editors

190M

Downloads

Our authors are among the

154

Countries delivered to

TOP 1%

most cited scientists

12.2%

Contributors from top 500 universities



WEB OF SCIENCE™

Selection of our books indexed in the Book Citation Index  
in Web of Science™ Core Collection (BKCI)

Interested in publishing with us?  
Contact [book.department@intechopen.com](mailto:book.department@intechopen.com)

Numbers displayed above are based on latest data collected.  
For more information visit [www.intechopen.com](http://www.intechopen.com)



---

# Observation of Fungi, Bacteria, and Parasites in Clinical Skin Samples Using Scanning Electron Microscopy

---

Ran Yuping, Zhuang Kaiwen, Hu Wenyong, Huang Jinghong, Feng Xiaowei, Chen Shuang, Tang Jiaoqing, Xu Xiaoxi, Kang Daoxian, Lu Yao, Zhang Ruifeng, Ran Xin, Wan Huiying, Lama Jebina, Dai Yalin and Zhang Chaoliang

Additional information is available at the end of the chapter

<http://dx.doi.org/10.5772/61850>

---

## Abstract

This chapter highlights the description of the clinical manifestation and its pathogen and the host tissue damage observed under the Scanning Electron Microscope, which helps the clinician to understand the pathogen's superstructure, the change of host subcell structure, and the laboratory workers to understand the clinical characteristics of pathogen-induced human skin lesions, to establish a two-way learning exchange database with vivid images

**Keywords:** Fungi, Bacteria, Parasite, Clinical Skin Samples, SEM

---

## 1. Introduction

In dermatovereology department, skin infections by fungi, bacteria, and, parasites are very common in routine clinical practice. Differentiation and identification of these pathogens are a huge challenge and very important for the patient's diseases diagnosis and treatment. Scanning electron microscope (SEM) is a very strong tool for detection and observation of pathogens from the clinical samples that helps us obtain a direct proof of the pathogen on the surface of the skin samples of the lesion. Based on the detailed morphologic image, we can recognize the ultrastructural of the pathogen and understand the pathogenesis of the skin-infected diseases. During recent years, we collected a lot of pathogenic microorganisms' photographs taken by SEM. These pathogens include fungi (*Trichophyton violaceum*, *Microsporum canis*, *Mucor irregularis*, *Lichtheimia (Absidia) corymbifera*, *Alternaria arboresce*, *Fon-*

---

*secaea pedrosoi*, *Aspergillus fumigatus* and *Malassezia*), bacteria (*Propionibacterium acnes*), and parasites (*Pediculosis pubis* and *Demodicid mites*) *in vivo* or *in vitro*. The diagnosis and clinical manifestation, the kinds of sample and the image of the pathogens are summarized in the Table 1.

Diagnosis	Clinical manifestation	Sample	Image of pathogen by SEM
Tinea capitis	Erythema, scales on the scalp; hair broken and hair loss	Infected hair	Fungus ( <i>Trichophyton violaceum</i> )
Tinea capitis	Excessive scales and hair loss on the scalp	Infected hair	Fungus ( <i>Microsporum canis</i> )
<i>Malassezia</i> folliculitis	Slightly pruritic, monomorphic follicular papules and pustules	Keratotic plug of pustule of hair follicle	Fungus ( <i>Malassezia</i> )
Pityriasis versicolor	Erythema and scaly, hyperpigmentation or hypopigmentation of skin	Scales	Fungus ( <i>Malassezia</i> )
Mucormycosis	Progressive red plaque around the inner canthus	Cultured colony	Fungus ( <i>Mucor irregularis</i> )
Mucormycosis	Purulent granuloma of left forearm	Cultured colony	Fungus ( <i>Lichtheimia corymbifera</i> )
Cutaneous alternariosis	An ulcer covered with crust on left anterior tibia	Cultured colony	Fungus ( <i>Alternaria arboresce</i> )
Chromoblastomycosis	Red plaque in the left knee	Cultured colony	Fungus ( <i>Fonsecaea pedrosoi</i> )
Primary laryngeal aspergillosis	Hoarseness, severe paroxysmal coughing and tachypnea	Biopsy tissue	Fungus ( <i>Aspergillus fumigatus</i> )
Acne	Recurrent papule and pustule acne	Pustule	Bacteria ( <i>Propionibacterium acnes</i> )
Pediculosis pubis	Intense itching of the scalp	Parasite	Parasite ( <i>Pubic lice</i> )
Demodicid mites	Itching, multiple erythema, papules, pustules	Hair follicle plug	Parasite ( <i>Demodex folliculorum</i> )

**Table 1.** Summary of diagnosis and clinical manifestation, kinds of sample, and the image of the pathogens observed by SEM

## 2. Methods

All samples for SEM were taken from clinical patients. These samples included infected hair, scales, colony of culture, and tissue of skin biopsy. The samples for SEM were fixed in 2% glutar-aldehyde for 4 h at 4 °C, dehydrated through four gradations of alcohol solutions (50%, 70%, 95%, 100%, progressively) for 15 min each, then soaked in isoamyl acetate for 30 min. The specimens were prepared after critical-point drying method, under which condi-

tion they were gilded in a vacuum chamber and observed under the SEM, FEI Inspect F50, equipped with an FEG gun operated at 30 kV at high vacuum.

### 3. Results

#### 3.1. Tinea capitis

Tinea capitis is a common superficial fungal infection of scalp hair follicles and surrounding skin. It often affects children rather than adults. Its pathogens are dermatophytes, usually species in the genera *Microsporum* and *Trichophyton*, such as *Microsporum canis*, *Trichophyton tonsurans*, and *Trichophyton violaceum* [1]. The clinical manifestation of tinea capitis is highly variable, depending on the causative organism, type of hair invasion and degree of host inflammatory response. Common features are patchy hair loss with varying degrees of scaling and erythema. However, the clinical signs may be subtle and diagnosis can be challenging. A number of clinical patterns exist [2]. The accurate diagnosis of tinea capitis usually depends on the laboratory investigation, mainly including direct microscopy with 10%–30% potassium hydroxide and fungal culture. It can confirm the diagnosis by detecting or isolating the causal organism by either of these two methods. Tinea capitis always requires systemic antifungal treatment. Topical treatment is only used as adjuvant therapy to systemic antifungals as topical antifungal agents do not penetrate the hair follicle. Recommended drug in systemic treatment include itraconazole, terbinafine, or griseofulvin.



**Figure 1.** a. A 9-year-old boy, weighing 25kg, presented to our clinic with slightly itching, multiple patchy areas of gray scaling lesions on the scalp and obvious hair loss.

We describe two cases of tinea capitis due to *T. violaceum* [3] and *M. canis* [4]. The first patient is a 9-year-old boy, weighing 25 kg, presented to our clinic because of multiple, slightly itching and patchy areas of gray scales on the scalp associated with hair loss (Fig. 1). The diagnosis of tinea capitis caused by *T. violaceum* was established by direct microscopic examination, culture, and slide-culture. The scanning electron microscope revealed that the infected hairs were destroyed by abundant fungus (Fig. 2). The boy was cured after receiving 4 weeks of systemic treatment with itraconazole 125 mg per day and topical treatment with 1% naftifine–0.25% ketaconazole cream, after wash with 2% ketaconazole shampoo once a day.

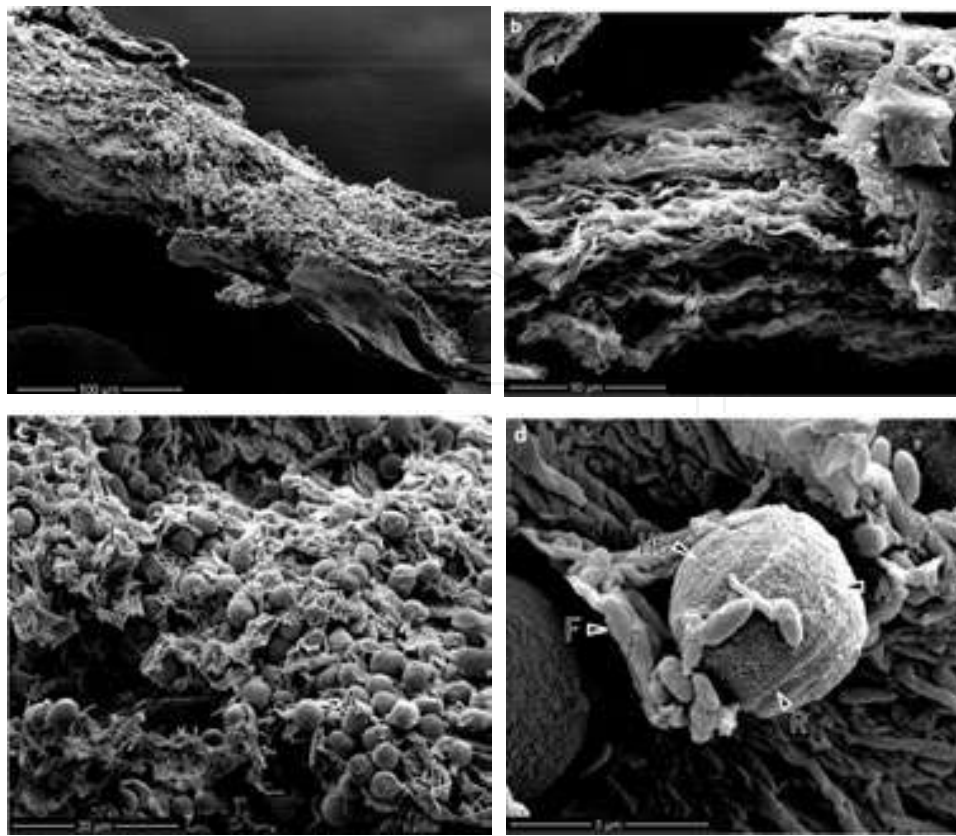


**Figure 2.** a-b. Cuticle layers of hair shaft were seriously destroyed and a large part had been lost, exposing the fibril cortex inside which many arthrospores were noted. c. High magnification of "a" showing the cuticle layers completely destroyed with the residual cortex fully filled with arthroconidia (A) and distorted fibril bundles (F). d. An arthrospore (A) at high magnification showing irregular convex granules on the chitinous surfaces and the poles bordered by a protruding ring structure (R), bulged by a hemispherical convex (HC). Numerous residual fibril fragments (F) noted around the spore.

The second patient is a 5-year-old boy in good health, weighing 19 kg and presented at our clinic with a 1-month history of excessive scales and hair loss on the scalp (Fig. 3a). He had been previously diagnosed with tinea capitis in a local hospital and received oral itraconazole 100 mg per day for 14 days administered with water. However, the area of hair loss enlarged slightly. Additionally, he had a history of direct contact with a pet dog. Direct microscopic examination (with 10% KOH) of broken hair strands showed numerous spores inside as well as outside of the hair strand. Simultaneously, strands were observed under SEM, and there were many round spores in and around the hair strand (Fig. 4a, b). Fungal culture revealed yellow filamentous colonies, which were identified as *Microsporum canis* with ITS1/4-PCR, sequence-based molecular validation (Accession Number: KJ1003284). A diagnosis of tinea capitis caused by *Microsporum canis* was confirmed. According to his weight, the boy was treated with itraconazole using the same dose as before, but in this course each dose was administered with whole milk instead with water before. After the 14-day course, clinic assessments showed the hair loss area was smaller and without scales (Fig. 3b). With the same examinations as before, only a few spores were detectable by direct microscopic examination. The number of spores was markedly reduced in hair strands, and

spores inside as well as outside of the hair strand. Simultaneously, strands were observed under SEM, and

there were many round spores in and around the hair strand (Fig. 4a, b). Fungal culture revealed yellow

round spores were now very irregular under SEM (Fig. 4c, d). The boy continued therapy for a total of 40 days. Clinical assessment of the treatment showed that there was no apparent hair loss and all of the same examinations now appeared to be normal (Fig. 3c). Upon clinical examination during the follow-up after 3 months, there was no recurrence following the end of the treatment [4].



**Figure 3.** a. A 5-year-old boy presented with 1-month history of scalp scales and hair loss, who had received oral itraconazole 100 mg per day with water for 14 days; b. The patch with hair loss was smaller and without scale after oral itraconazole 100 mg per day with whole milk for 14 days; c. There was no apparent hair loss on scale after 40 days at end of treatment.

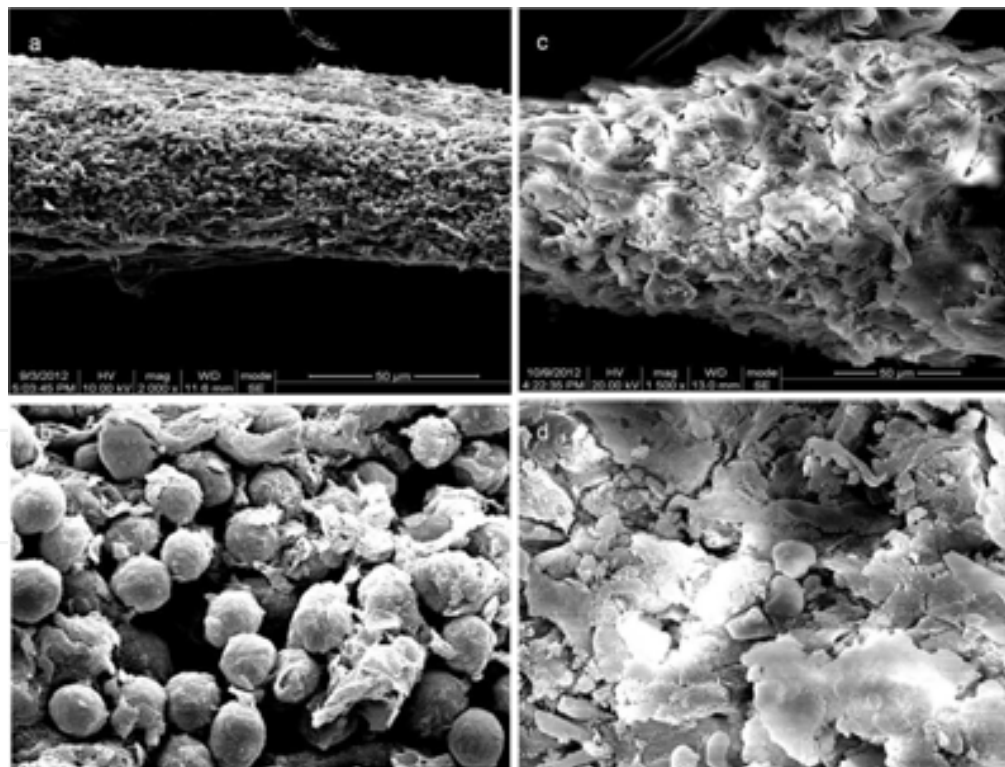


**Figure 4.** a-b. After oral itraconazole 100 mg per day with water for 2 weeks, broken hair strands with many round spores in and around the hair strands were evident under scanning electron microscopy (SEM); c-d. Oral itraconazole 100 mg per day with whole milk for 14 days, the number of spores were markedly reduced in broken hair strands, and spores appeared very irregular under SEM.

### 3.2. *Malassezia* folliculitis (*Pityrosporum* folliculitis)

*Malassezia* folliculitis is most commonly seen in teenagers and adults, which is characterized by pruritic, monomorphic follicular papules and pustules on the upper trunk, arms, neck and occasionally on the face. It is due to excessive growth of *Malassezia* spp. within the hair follicle, with resulting inflammation (from yeast products and free fatty acids produced by fungal lipase). Only yeast forms are observed, no hyphal forms as in pityriasis versicolor [5]. Diagnostic studies include microscopic evaluation of the presence of yeast, cultures, and biopsies. Additionally, Woods lamp can be used to illuminate the lesions, which portray a yellow-green fluorescence. Both topical and oral antifungal agents are effective agents in the treatment of *Malassezia* folliculitis and are commonly combined to hasten resolution and maintain clearance. Topical regimens include daily wash with ketoconazole shampoo 2%, then 1% naftifine-0.25% ketaconazole cream. For severe cases, it needs systemic administration of antifungal agents. Commonly used regimens include oral fluconazole 150 mg weekly for 2–4 weeks, and itraconazole 200 mg daily for 2–4 weeks [6].

The following is a case of *Malassezia* folliculitis due to *Malassezia* spp. The patient is a 25-year-old man, who was presented to our clinic because of slightly pruritic, monomorphic follicular papules and pustules on the upper trunk and neck (Fig. 5a). The diagnosis of *Malassezia* folliculitis was established by direct microscopic examination, culture, and scanning electron microscopy. The scanning electron microscope of the hair follicle from the upper trunk revealed a large number of yeast of two kinds, orbicular-ovate and globular (Fig. 5 b-c). The man was cured after receiving 4 weeks of systemic treatment with itraconazole 200 mg per day and topical treatment with 1% naftifine–0.25% ketaconazole cream after wash with 2% ketaconazole shampoo once a day.

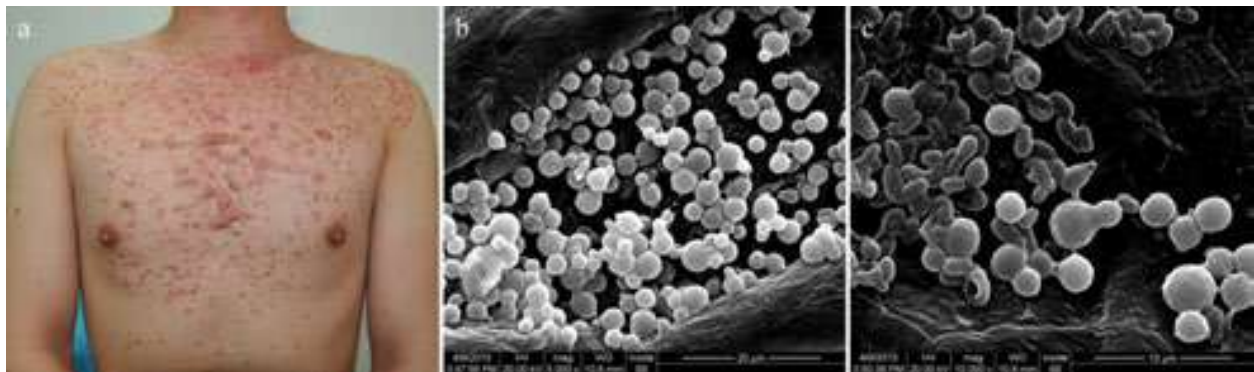


**Figure 5.** a. A 25-year-old man with complains of slightly pruritic, monomorphic follicular papules, pustules, and secondary keloid on the upper trunk and neck. b-c. SEM of the hair follicle from the upper trunk. These demonstrated a large number of globular or orbicular-ovate yeasts of budding daughter cell, with collar structure around the budding. b. Globular yeast. c. Orbicular-ovate and globular yeast in the same sample.

### 3.3. Pityriasis versicolor

Pityriasis versicolor is a superficial fungal infection of the skin and caused by *Malassezia*, a lipophilic yeast, which is part of the normal skin flora. Certain environmental, genetic, and

are also susceptible populations [9]. Immunological factors can lead to the development of disease [7]. The prevalence is as high as 50% in tropical areas [8]. Prevalence increases significantly in childhood and adolescence, probably because of increased sebum production, which allows for a more lipid-rich environment for *Malassezia* to grow. Adolescents and young adults who are physically active are also susceptible populations [9]. This is a case of pityriasis versicolor due to *Malassezia* spp. A 27-year-old man was presented to our clinic with extensive erythema and scaly for 6 months (Fig. 6a). The scaly was scraped and observed through SEM. Under SEM, numerous hyphae and spores that resemble “banana-like grapes” (Fig. 6b). The scaly was treated with oral itraconazole 200 mg (Fig. 6c) and topical use of 1% naftifine–0.25% ketoconazole cream after wash with 1% naftifine–0.25% ketoconazole cream after wash with ketoconazole shampoo was effective.

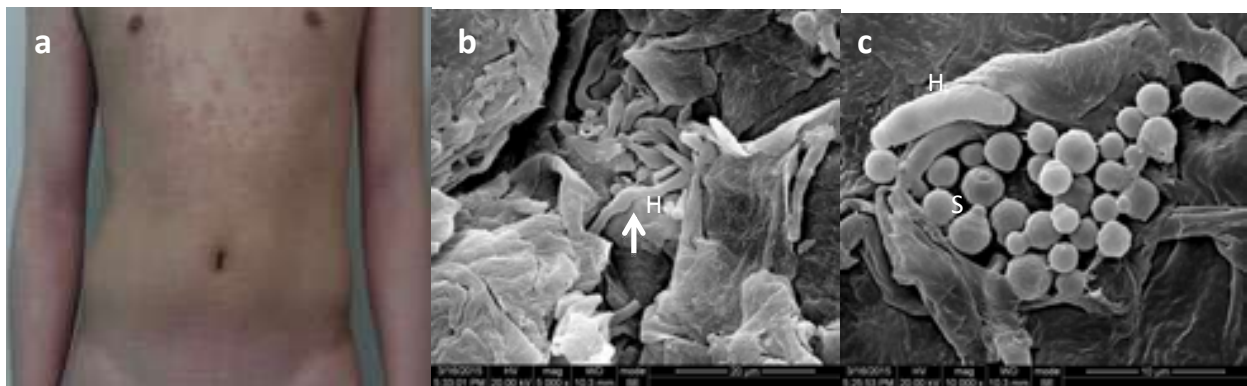


Figure 6. a. A 27-year-old man presented in our clinic with extensive erythema and scaly for 6 months. b. Under SEM, numerous hyphae (H) went through the scaly, length of which is about 10–20 μm. c. Under SEM, abundant of 3–5 μm in diameter grapes-like spherical *Malassezia* spores (S) with budding daughter cell, with collar structure around the budding, and banana-like haphae (H).

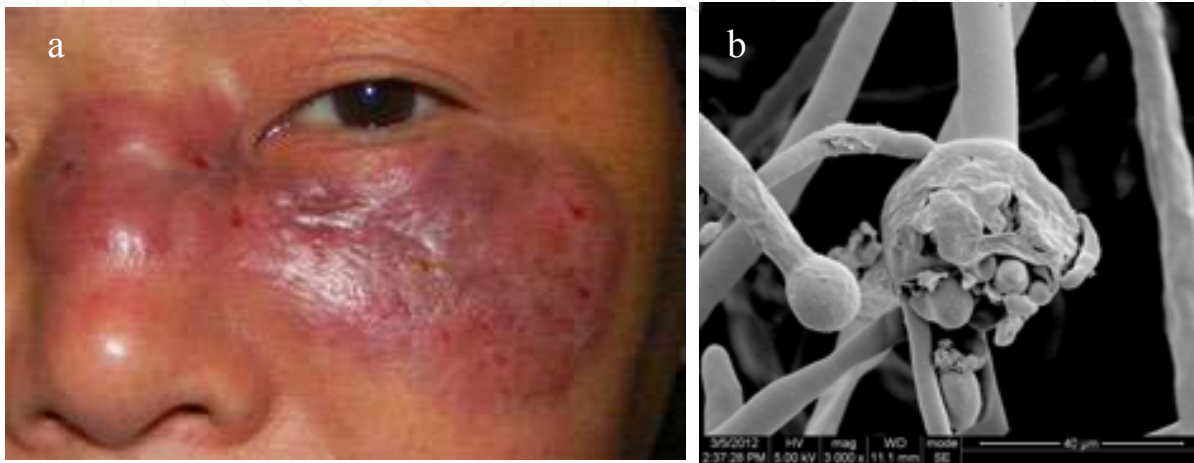
abundant of 3–5 μm in diameter grapes-like spherical *Malassezia* spores (S) with budding daughter cell, with

### 3.4. Mucormycosis

collar structure around the budding, and banana-like haphae (H). Mucormycosis is a clinically rare and fatal opportunistic fungal infection, which invades nasal, brain, lung, gastrointestinal tract, skin, and other parts with acute, subacute, or chronic process. The routes of invasion contain respiratory tract, digestive tract, skin, and neonatal umbilical region [10]. Its pathogens are fungi in the order *Mucorales*, usually species in the genera *Mucor*, *Rhizopus*, and *Lichtheimia (Absidia)*, such as *Mucor irregularis*, *Rhizopus stolonifer*, *Mucor and Lichtheimia corymbifera*. A fatal opportunistic mycotic infection, which invades nasal, brain, lung, described in China [10]. Amphotericin B and its lipid derivatives are considered as the effective drugs to treat mucormycosis.

The following is a description of two cases of primary cutaneous mucormycosis caused by contain respiratory tract, digestive tract, skin, and neonatal umbilical region [10]. Its pathogens are fungi in the *Mucor irregularis* [10] and *Lichtheimia corymbifera* [11], respectively. One of the cases is of a 47-year-old farmer, who presented to our clinic with a history of progressive red plaque around the inner canthus (Fig. 7a), following dacryocystectomy about a year earlier. Linear, aseptate hyphae were seen by direct KOH examination and in biopsy. Fungal culture re-*irregularis*, *Rhizopus stolonifer*, and *Lichtheimia corymbifera*. *M. irregularis* is a newly recognized fungal

presented to our clinic with a history of progressive red plaque around the inner canthus (Fig. 7a), following vealed light-yellow filamentous colonies that were identified as *Mucor irregularis* by nucleotide sequencing of rRNA gene. SEM observations revealed non-apophysate sporangia with pronounced columellae and conspicuous collarette at the base of the columella following biopsy. Fungal culture revealed white filamentous colonies that were identified as *Mucor irregularis* by nucleotide sequencing of rRNA gene. SEM observations revealed non-apophysate sporangia with pronounced columellae and conspicuous collarette at the base of the columella following sporangiospore dispersal (Fig.



7b). Amphotericin B and dexamethasone were used in the treatment. The patient was discharged after 2 months of treatment. The plaque became smooth, and there was no recurrence for half a year through telephone follow-up. The other case is of a 69-year-old female farmer, who presented to our clinic with the history of a progressive purulent granuloma of her left forearm (Fig. 8a) following a fracture of left forearm about 11 months earlier. Broad, nonseparate hyphae were seen in pathologic study with methenamine silver stain (Fig. 8b). Fungal culture revealed white filamentous colonies that were identified as *Lichtheimia corymbifera* by nucleotide sequencing of rRNA gene. The scanning electron microscope showed that the sporangia are slightly pear-shaped instead of spherical. The sporangiophores of *Lichtheimia corymbifera* formed a conical apophysis and a collarette at the base of the columella following sporangiospore dispersal (Fig. 8c).

The patient was discharged after 2 months of treatment. The plaque became smooth, and there was no recurrence for half a year through telephone follow-up.

The other case is of a 69-year-old female farmer, who presented to our clinic with the history of a progressive purulent granuloma of her left forearm (Fig. 8a) following a fracture of left forearm about 11 months earlier. Broad, nonseparate hyphae were seen in pathologic study with methenamine silver stain (Fig. 8b). Fungal culture revealed white filamentous colonies that were identified as *Lichtheimia corymbifera* by nucleotide sequencing of rRNA gene. The scanning electron microscope showed that the sporangia are slightly pear-shaped instead of spherical. The sporangiophores of *Lichtheimia corymbifera* formed a conical apophysis and a collarette at the base of the columella following sporangiospore dispersal (Fig. 8c).

Antimicrobial susceptibility test indicated that *Lichtheimia corymbifera* is most sensitive to terbinafine and voriconazole. The patient was cured after the deletion of the center of plaque. Some scales were also observed on the plaque.

### 3.5. Cutaneous alternariosis

*Alternaria*, an opportunistic fungus, is pigmented (also known as dematiaceous or phaeoid) filamentous fungi, which are well-known soil saprophytes and plant pathogens that infrequently cause infection in humans. Although *Alternaria* usually infects immunocompromised patients [12], in rare cases it infects healthy or immunocompetent individuals as well.

The other case is of a 69-year-old female farmer, who presented to our clinic with the history of a progressive purulent granuloma of her left forearm (Fig. 8a) following a fracture of left forearm about 11 months earlier.

patient was cured after 6 weeks of therapeutic alliance of oral itraconazole with surgery [11].

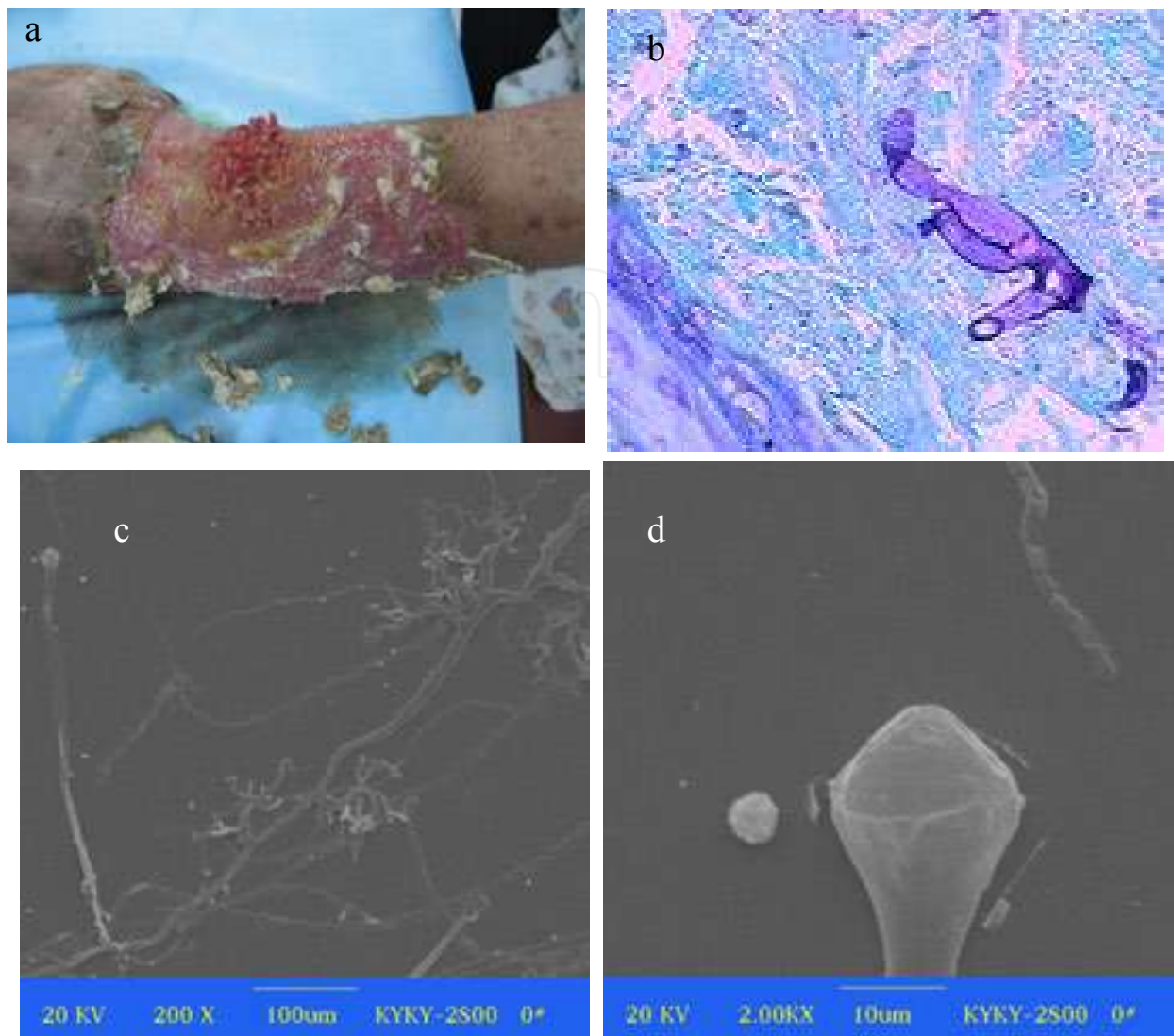


Figure 8. a. A 69-year-old female was presented to our clinic with a progressive purulent granuloma of her left forearm. b. Broad nonseparate hyphae were seen in pathologic study (methenamine silver stain,  $\times 200$ ). c-d. The sporangio-phores of *Lichtheimia corymbifera* were seen in pathologic study (methenamine silver stain,  $\times 200$ ) and SEM. The sporangio-phores of *Lichtheimia corymbifera* forming a conical apophysis and arising at points on the stolon that was between the rhizoid and not opposite them. SEM showed the sporangia were slightly pear-shaped instead of spherical (20kv,  $\times 2000$ ).

The sporangio-phores of *Lichtheimia corymbifera* forming a conical apophysis and arising at points on the

There is no standard therapy for cutaneous alternariosis and the patients are usually treated with surgical resection and/or antifungal therapy.

was described in a healthy individual with cutaneous alternariosis due to infection with *Alternaria arborescens* [13]. A 28-year-old man presented at our clinical with a one-month history of ulcers covered with crust on his left anterior tibial (Fig. 9a).

Fungal culture of the tissue revealed dark grey-white colonies with a dark-brown underside (Fig. 9b) and the SEM observation of the slide culture revealed beaked conidia (Fig. 9c).

### 3.5. Cutaneous alternariosis

Based on the morphological features and molecular identification, the patient was diagnosed as cutaneous alternariosis. He was successfully treated with oral itraconazole and topical wet dressing of amphotericin B.

*Alternaria*, an opportunistic fungus, is pigmented (also known as dematiaceous or phaeoid) filamentous fungi, which are well-known soil saprophytes and plant pathogens that infrequently cause infection in humans.

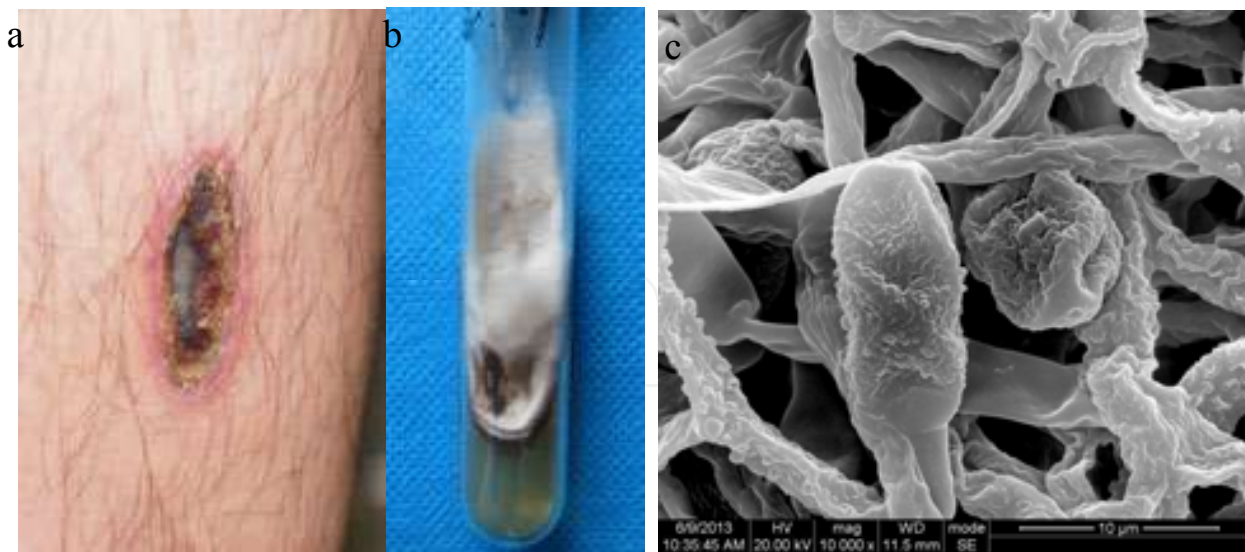


**Figure 9.** a. Ulcer with an overlying crust on the patient's skin of left anterior tibia. b. Fungal culture of the tissue revealed dark grey-white colonies with a dark-brown underside. c. SEM observation of slide culture revealed beaked conidia.

tissue revealed dark grey-white colonies with a dark-brown underside. c. SEM observation of slide culture

### 3.6. Chromoblastomycosis

revealed beaked conidia.

Chromoblastomycosis is a chronic fungal infection of the skin and subcutaneous tissue caused by dematiaceous fungi. Common pathogenic fungi are *Fonsecaea pedrosoi*, *Phialophora verrucosa*, *Cladophialophora carrionii*, among others. These fungi exist in the natural environment in soil, water, vegetation, or wood splinters, and usually are inoculated in the skin tissue of human body by a traumatic injury. A higher incidence is reported in tropical and subtropical countries. Cutaneous lesions can be nodules, papules, and/or ulcerations and mostly affect the lower limbs. The diagnosis of chromoblastomycosis is based on direct examination, culture, and histopathology. On treatment, long courses of antifungal agents such as itraconazole, terbinafine can be used alone or in combination with surgical excision, and physical treatments (cryotherapy or, mostly, thermotherapy). However, long duration of treatment is needed and cure rate of the disease is low [14].

In this part we describe a case of chromoblastomycosis due to *Fonsecaea pedrosoi*. A 34-year-old male presented at our clinic with a 12-year history of red plaque in the left knee (Fig. 10a). The patient's left knee was punctured by a fragment of a brick 12 years ago. The pathogenic fungus was isolated and identified as *Fonsecaea pedrosoi*. SEM observation: dematiaceous hyphae with many well-defined septa, conidiophores and oval brown spores arranged in a clump could be seen. The surfaces of conidiogenous cells were smooth. Oval spores were arranged around conidiophores (Fig. 10b). The patient was diagnosed as chromoblastomycosis and was treated with oral terbinafine 250 mg twice a day and thermotherapy with a small electronic heating pad (42°C, more than one hour per day) after applying topical cream containing 1% naftifine hydrochloride and 0.25% ketoconazole. The total course was 61 weeks. The crust and pruritus had disappeared and the erythema and plaque had turned smooth and soft.

In this part we describe a case of chromoblastomycosis due to *Fonsecaea pedrosoi*. A 34-year-old male presented at our clinic with a 12-year history of red plaque in the left knee (Fig. 10a). The patient's left knee

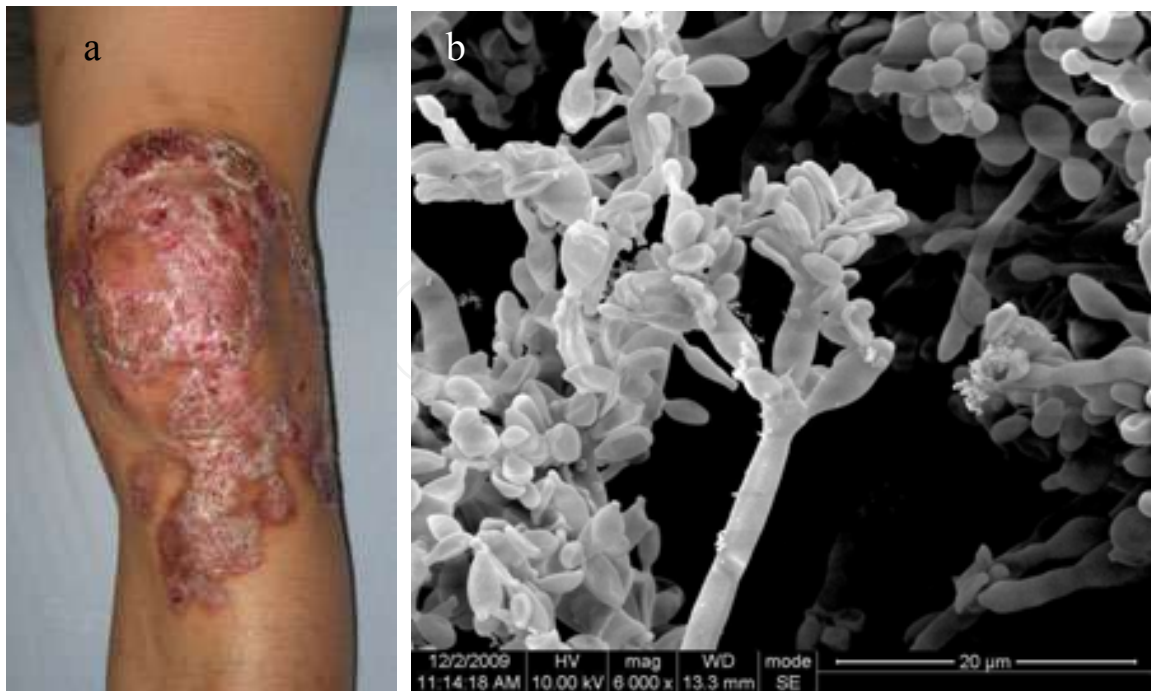


**Figure 10** a. A 34-year-old male with a 12-year history of a red plaque in the left knee. b. Under SEM observation: dematiaceous hyphae with many well-defined septa, conidiophores, and oval brown spores arranged in a clump could be seen. The surfaces of conidiogenous cells were smooth. Oval spores were arranged around conidiophores.

### 3.7. Primary laryngeal aspergillosis

Primary laryngeal aspergillosis is a rare opportunistic infection caused by *Aspergillus*. All causes leading to immunocompromisation are generally due to etiological factors [15]. For immunocompetent patients, oral sex (fellatio) may be the primary cause [16]. Airborne spore colonizes in the larynx through inhalation, then white colony grows on vocal cords or/and laryngeal ventricle. It is characterized by chronic hoarseness, with or without systemic or respiratory symptoms involving fever, cough, and tachypnea. It is usually diagnosed by laryngoscopy and biopsy. Systemic antifungal treatment is often effective.

### 3.7. Primary laryngeal aspergillosis

We describe in the following a case of primary laryngeal aspergillosis due to *Aspergillus fumigatus*. The patient was a 23-year-old female undergraduate student, who presented with chronic hoarseness, severe paroxysmal coughing, and tachypnea. Laryngoscopy revealed obvious white plaques on the swollen vocal cords and laryngeal ventricle (Fig. 11a). The diagnosis of laryngeal aspergillosis was established by the clinical manifestations and the hyphae branching at 45° angles under microscopy, SEM (Fig. 11b), and pathology. She was cured with oral itraconazole at 200 mg twice a day for 28 days.

We describe in the following a case of primary laryngeal aspergillosis due to *Aspergillus fumigatus*. The patient was a 23-year-old female undergraduate student, who presented with hoarseness, severe paroxysmal coughing, and tachypnea. Laryngoscopy revealed obvious white plaques on the swollen vocal cords and laryngeal ventricle (Fig. 11a). The diagnosis of laryngeal aspergillosis was established by the clinical manifestations and the hyphae branching at 45° angles under microscopy, SEM (Fig. 11b), and pathology. She was cured with oral itraconazole at 200 mg twice a day for 28 days.

laryngoscopy and biopsy. Systemic antifungal treatment is often effective.

### 3.8. Acne

Acne is a chronic inflammatory disease of the sebaceous-piloosebaceous system. It is estimated to affect 9.4% of the global population [17]. Acne is closely related to the combination of genetic and environmental factors, among which *Propionibacterium acnes* (*P. acnes*) plays a

key role in the pathogenesis of acne. We describe in the following a case of primary laryngeal aspergillosis due to *Aspergillus fumigatus*. The patient was a 23-year-old female undergraduate student, who presented with hoarseness, severe paroxysmal

coughing, and tachypnea. Laryngoscopy revealed obvious white plaques on the swollen vocal cords and laryngeal ventricle (Fig. 11a). The diagnosis of laryngeal aspergillosis was established by the clinical



**Figure 11.** a. A 23-year-old female undergraduate student presented with hoarseness, severe paroxysmal coughing, and tachypnea. Laryngoscopy revealed obvious white plaques on the swollen vocal cords and laryngeal ventricle. b. SEM image of the larynx showing branching at 45° angles destroyed the vocal cords tissue.

Gram-positive anaerobic bacterium branching is a major commensal of the follicular plug in human skin. Other diseases such as medical device and surgery infections caused by *P. acnes* have also been reported. Strains of *P. acnes* have been classified into several different types [19].

**3.8 Acne**

The following is a description of a case of acne in a 24-year-old girl. She suffered recurrent papule and pustule acne for 6 months (Fig. 12a-b). We removed the follicular plug with sterile hemostatic forceps and observed it through SEM. Under SEM, abundant rod-shaped bacteria were closely spaced in follicular plug tissue (Fig. 12c). Treatment with oral minocycline 50 mg twice a day and topical use of adapalene gel was effective.

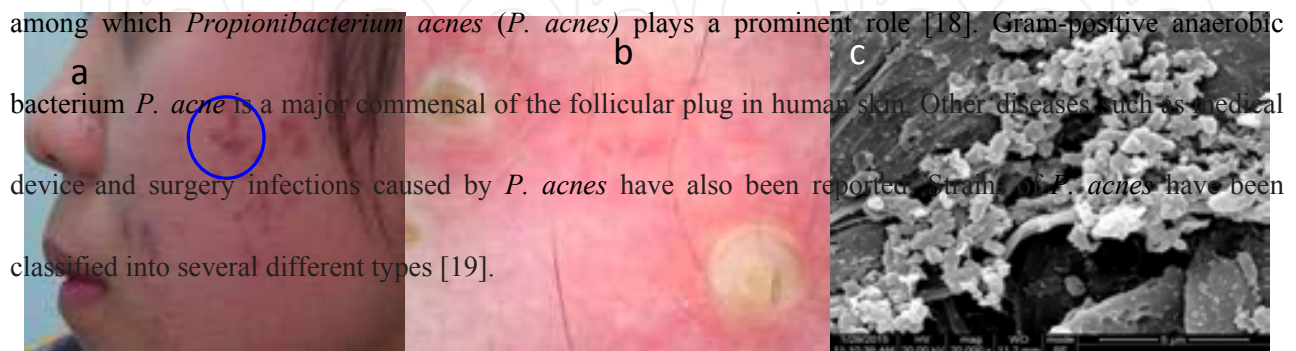


**Figure 12.** a. A 24-year-old girl who suffered recurrent papule and pustule acne for 6 months. b. Under the dermoscopy, the papule was semisphere with tawny follicular plug inside. c. Under SEM, rod-shaped bacteria were closely spaced in follicular plug tissue.

dermoscopy, the papule was semisphere with tawny follicular plug inside. c. Under SEM, rod-shaped bacteria were closely spaced in follicular plug tissue. Treatment with oral minocycline 50 mg twice a day and topical use of adapalene gel was effective.

**3.9. Pediculosis**

Pediculosis is a skin disease caused by arthropods. Its pathogens are three lice species including head louse,

### 3.9. Pediculosis

Pediculosis is a skin disease caused by arthropods. Its pathogens are three lice species including head louse, crab or pubic louse, and body louse, which cause the *Pediculus humanus capitis*, *Phthirus pubis*, and *Pediculus humanus corpus*, respectively. These three insects are obligate human parasites. They are transmitted by person-to-person contact [20]. Itching in various levels of severity is the primary symptom of pediculosis. Crab louse is about 0.8–1.2 mm in length. Its legs are clawed, except for the first pair, which is shortened and vestigial. In contrast to the oval shape of head and body lice, the crab louse is almost as wide as its length, allowing it to grasp widely spaced pubic hairs [21]. Its crab appearance accounts for its name. Patients with pubic lice may be instructed to launder clothing and bedding and to avoid sexual or other intimate contact until their infestations are cured [22]. In case of infestation of head with pubic lice, the head can be shaved totally and then treated with an occlusive agent such as Vaseline petroleum jelly.

We describe a case of pediculosis on the scalp of a 6-year-old boy caused by the crab louse [23]. The boy was presented to our clinic with the complaint of intense itching of the scalp. There were some small pieces of erythema (in the circle) and a brown dot-like substance on his scalp (Fig. 13a). The dermoscopy revealed a brown parasite (0.9 mm in horizontal axes and 1.2 mm in vertical axes) with two crab-like feet adhered to the scalp (Fig. 13b). Microscopic examination and scanning electron microscope showed the detail of this insect (Fig. 13c-d). Based on these morphological findings, the diagnosis of *Pediculus humanus capitis* caused by crab louse is confirmed. Generally, *pediculus humanus capitis* is caused by head louse, rarely by crab louse. Where could this pathogen, crab louse, be from? After a detailed inquiry, his father was found to have pediculosis pubis that had been cured. Therefore, the boy was instructed to shave the head totally and then treated with an insecticidal tincture, which was administered to his parents as well. The boy was cured after 15 day of treatment.

### 3.10. Demodicosis

Demodicosis is a kind dermatitis caused by *Demodex*. It often presents some rosacea-like lesions. *Demodex* is a genus of tiny parasitic mites that live in or near hair follicles of mammals. Currently, about 65 species of *Demodex* are known [24]. Two species living on humans have been identified: *Demodex folliculorum* and *Demodex brevis*, both frequently referred to as eyelash mites [25]. The adult mites are 0.3–0.4 mm long, and 0.012–0.016 mm in diameter, with *D. brevis* slightly shorter than *D. folliculorum* [26]. Each has a semitransparent, elongated body that consists of two fused segments. Eight short, segmented legs are attached to the first body segment. The body is covered with scales for anchoring itself in the hair follicle, and the mite has pin-like mouth for eating skin cells and sebum, which accumulate in the hair follicles. The mites can leave the hair follicles and slowly walk around on the skin, at a speed of 8–16 mm per hour, especially at night, as they try to avoid light [26]. In most of the cases, the mites go unobserved, without any symptoms, but in certain cases (usually related to a disordered immune system) mite populations can dramatically increase, resulting in a condition known as *demodicosis* or *demodex mite* bite, characterized by itching, inflammation, and other skin disorders.

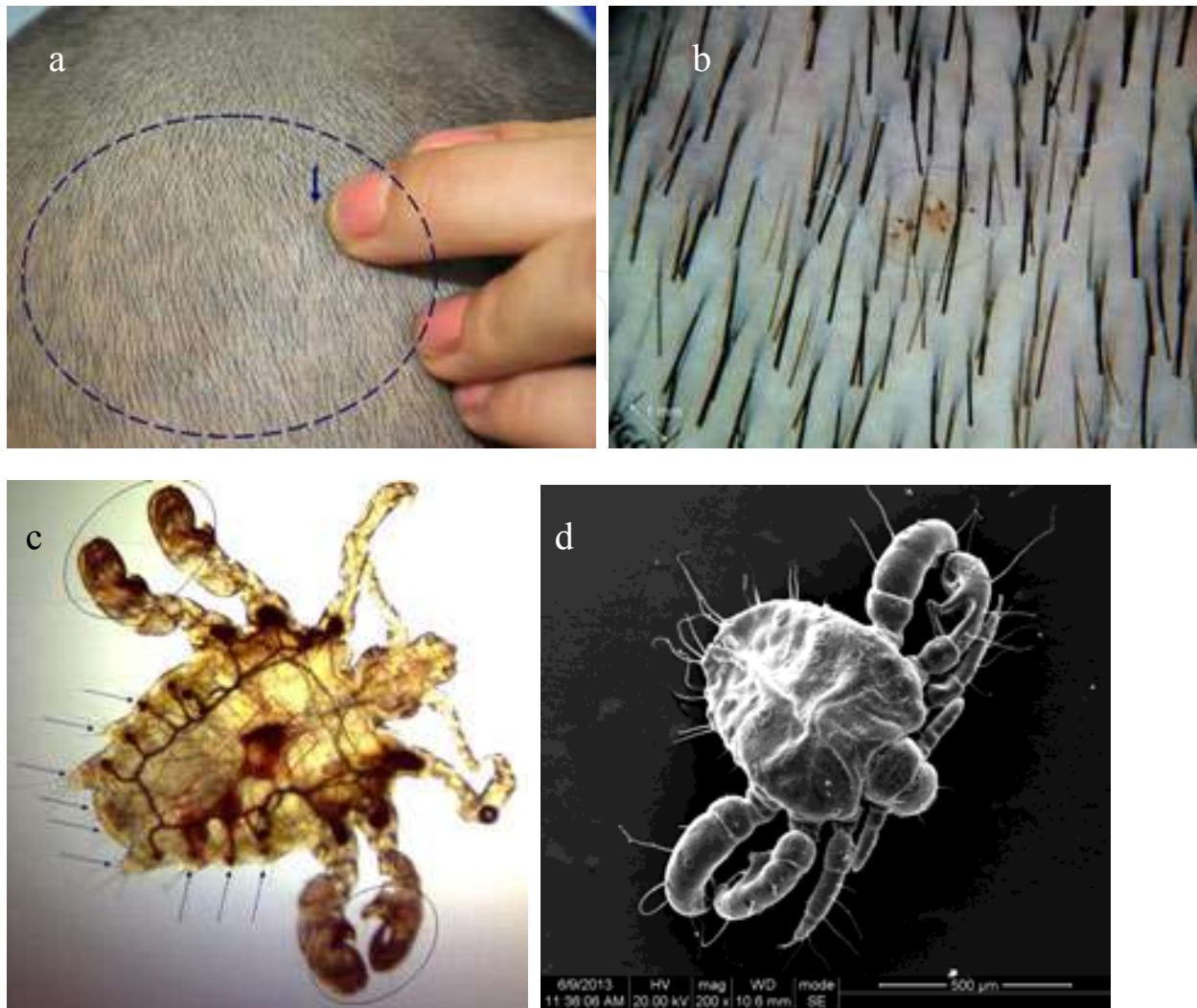


**Figure 13.** a. There were some small pieces of erythema (in the circle) and a brown dot-like substance on the scalp (arrow). b. The dermoscopy revealed a brown parasite (0.9 mm in horizontal axes and 1.2 mm in vertical axes) with two crab-like feet adhered to the scalp. c. Under the microscope, the parasite was characterized by a flat body like a crab and three pairs of feet in different sizes. There was an area (red box) full of blood in the middle part of the parasite. A large number of short setae (arrow) were noted at the edge of the parasite abdomen. d. The SEM showed a vivid three-dimensional ultrastructure of the parasite; the whole body was composed of three parts including spherical head, chest, and elliptical abdomen; a pair of feelers was noted on the head; the three pairs of feet were in shaped section and curved serrated claws were noted at the end of foot; short setae in different length were not only at the edge of the abdomen but also on the feet.

The following is a description of a case of demodicosis due to *Demodex mites*. The patient is a 28-year-old man, who came to our clinic because of itching, multiple erythema, papules, pustules lesions on the nose and cheek (Fig. 14a). The diagnosis of demodicosis caused by *Demodex mites* was established by direct microscopic examination. The observation of SEM revealed that the parasite consists of two segments. There were four pairs of feet on the side of the head of the parasite and its abdomen was characterized by annular striae on the surface (Fig. 14b). The man was cured after receiving 6 months of topical treatment with 7% al-bendazole cream once a day.

### 3.10. Demodicosis

Demodicosis is a kind dermatitis caused by *Demodex*. It often presents some rosacea-like lesions. *Demodex*



Figure 14. a. A 28-year-old man came to our clinic because of itching, multiple erythema, papules, pustules lesions on the nose and cheek. b. SEM revealed a *Demodex folliculorum*, approximately 0.33 mm in length, in the infected skin. Its elongated body consisted of two segments. There were four pairs of feet on the side of the head of the parasite and its abdomen was characterized by annular striae on the surface.

the infected skin. Its elongated body consisted of two segments. There were four pairs of feet on the side of

the head of the parasite and its abdomen was characterized by annular striae on the surface.

## Author details

Ran Yuping<sup>1\*</sup>, Zhuang Kaiwen<sup>1</sup>, Hu Wenying<sup>1</sup>, Huang Jinghong<sup>1</sup>, Feng Xiaowei<sup>1</sup>,  
Chen Shuang<sup>1</sup>, Tang Jiaoqing<sup>1</sup>, Xu Xiaoxi<sup>1</sup>, Kang Daoxian<sup>1</sup>, Lu Yao<sup>1</sup>, Zhang Ruifeng<sup>1</sup>, Ran Xin<sup>1</sup>,  
Wan Huiying<sup>1</sup>, Lama Jebina<sup>1</sup>, Dai Yalin<sup>2</sup> and Zhang Chaoliang<sup>3</sup>

\*Address all correspondence to: ranyuping@vip.sina.com

1 Department of Dermatoverereology, West China Hospital, Sichuan University, Chengdu, China

2 Department of Medical laboratory, West China Hospital, Sichuan University, Chengdu, China

3 State Key Laboratory of Oral Diseases, West China Hospital of Stomatology, Sichuan University, Chengdu, China

## References

- [1] Ellabib MS, Agaj M, Khalifa Z, Kavanagh K. *Trichophyton violaceum* is the dominant cause of tinea capitis in children in Tripoli, Libya: Results of a two year survey. *Mycopathologia*. 2001; 153: 145-147.

- [2] Yu J, Li R, Bulmer G. Current topics of tinea capitis in China. *Jpn J Med Mycol.* 2005; 46: 61-66.
- [3] Zhuang K, Ran X, Lei S, Zhang C, Lama J, Ran Y. Scanning and transmission electron microscopic observation of the parasitic form of *Trichophyton violaceum* in the infected hair from tinea capitis. *Scanning.* 2014; 36: 465-470.
- [4] Chen S, Ran Y, Dai Y, Lama J, Hu W, Zhang C. Administration of oral itraconazole capsule with whole milk shows enhanced efficacy as supported by scanning electron microscopy in a child with tinea capitis due to *Microsporum canis*. *Pediatric Dermatology.* 2015; 32:e312-e313
- [5] Rubenstein RM, Malerich SA. *Malassezia (Pityrosporum)* folliculitis. *J Clin Aesthet Dermatol.* 2014; 7: 37-41.
- [6] Hald M, Arendrup MC, Svejgaard EL, Lindskov R, Foged EK, Saunte DM. Evidence-based Danish guidelines for the treatment of *Malassezia*-related skin diseases. *Acta Derm Venereol.* 2015; 95: 12-19.
- [7] Renati S, Cukras A, Bigby M. Pityriasis versicolor. *BMJ.* 2015; 350: 1394-1400.
- [8] Kaushik A, Pinto HP, Bhat RM, Sukumar D, Srinath MK. A study of the prevalence and precipitating factors of pruritus in pityriasis versicolor. *Ind Dermatol Online J.* 2014; 5: 223-224.
- [9] Kyriakis KP, Terzoudi S, Palamaras I, Pagana G, Michailides C, Emmanuelides S. Pityriasis versicolor prevalence by age and gender. *Mycoses.* 2006; 49: 517-518.
- [10] Kang D, Jiang X, Wan H, Ran Y, Hao D, Zhang C. *Mucor irregularis* Infection around the inner canthus cured by amphotericin B: A case report and review of published literatures. *Mycopathologia.* 2014; 178: 129-133.
- [11] Lu W, Lu J, Ran Y, Lin Z, Wan H, Cui F, Cao L, Pan N, Song X, Chen J, Wanf Y, Yu M. Cutaneous and subcutaneous coinfection by *Lichtheimia corymbifera* and *Candida parapsilosis*: a case report. *Chin J Dermatol.* 2012; 45(10):727-730. (in Chinese)
- [12] Anaissie EJ, Bodey GP, Rinaldi MG. Emerging fungal pathogens. *Eur J Clin Microbiol Infect Dis.* 1989; 8: 323-330.
- [13] Hu W, Ran Y, Zhuang K, Lama J, Zhang C. *Alternaria arborescens* infection in a healthy individual and literature review of cutaneous alternariosis. *Mycopathologia.* 2015; 179: 147-152.
- [14] Krzyściak PM, Pindycka-Piaszczyńska M, Piaszczyński M. Chromoblastomycosis. *Adv Dermatol Allergol/Postepy Dermatologii i Alergologii.* 2014;31(5):310-321. doi: 10.5114/pdia.2014.40949.
- [15] Ran Y, Yang B, Liu S, Dai Y, Pang Z, Fan J, Bai H, Liu S. Primary vocal cord aspergillosis caused by *Aspergillus fumigatus* and molecular identification of the isolate. *Med Mycol.* 2008; 46: 475-479.

- [16] Ran Y, Li L, Cao L, Dai Y, Wei B, Zhao Y, Liu Y, Bai H, Zhang C. Primary vocal cord aspergillosis and scanning electron microscopical observation of the focus of infection. *Mycoses* 2011;54:e634-637.
- [17] Ran Y, Lu Y, Cao L. Primary laryngeal aspergillosis related to oral sex? A case report and review of the literature. *Med Mycol Case Rep.* 2013; 2: 1-3.
- [18] Tan JK, B Ran Y, Lu Y, Cao L, hate K. A global perspective on the epidemiology of acne. *Br J Dermatol.* 2015; 172; Suppl 1: 3-12.
- [19] Antiga E, Verdelli A, Bonciani D, Bonciolini V, Caproni M, Fabbri P. Acne: a new model of immune-mediated chronic inflammatory skin disease. *G Ital Dermatol Venereol.* 2015; 150: 247-254.
- [20] Yu Y, Champer J, Garbán H, Kim J. Typing of *Propionibacterium acnes*: a review of methods and comparative analysis. *Br J Dermatol.* 2015; 172: 1204-1209.
- [21] David C, Flinders, Peter DS. Pediculosis and scabies. *Am Fam Physician.* 2004;69: 341-348.
- [22] Ko CJ, Elston DM. Pediculosis. *J Am Acad Dermatol.* 2004, 50: 1-12.
- [23] Gunning K, Pippitt K, Kiraly B, Sayler M. Pediculosis and scabies: treatment update. *Am Fam Physician.* 2012; 15: 535-541.
- [24] Ran Y, Feng X, Zhuang K, Zhang C. Dermatoscopy, microscopy and scanning electron microscopy diagnosed scalp pediculosis pubis in a child. *J Clin Dermatol.* 2014;43(12):725-726. (in Chinese)
- [25] Rusiecka-Ziółkowska J, Nokiel M, Fleischer M. Demodex – an old pathogen or a new one? *Adv Clin Exp Med.* 2014; 23: 295-298.
- [26] Elston CA, Elston DM. Demodex mites. *Clin Dermatol.* 2014; 32: 739-743.
- [27] Rufli T, Mumcuoglu Y. The hair follicle mites *Demodex folliculorum* and *Demodex brevis* – biology and medical importance: a review. *Dermatologica.* 1981;162:1-11.